ÇUKUROVA UNIVERSITY

INSTITUTE OF NATURAL AND APPLIED SCIENCES

Ph.D. THESIS

Coşkun ÖZALP

LARGE- AND SMALL-SCALE INSTABILITIES FOR SHEAR-LAYER ALONG A PERFORATED SURFACE

DEPARTMENT OF MECHANICAL ENGINEERING

ADANA, 2006

ÇUKUROVA ÜNİVERSİTESİ
FEN BİLİMLERİ ENSTİTÜSÜ

LARGE- AND SMALL-SCALE INSTABILITIES FOR SHEAR-LAYER ALONG A PERFORATED SURFACE

Coşkun ÖZALP

DOKTORA TEZİ

MAKİNA MÜHENDİSİĞİ ANABİLİMDALI

Bu Tez …../…../2006 Tarihinde Aşağıdaki Jüri Üyeleri Tarafından Oybirliği/Oyçokluğu ile Kabul Edilmiştir.

İmza: ……	İmza:……	İmza…….
Doç.Dr.Ahmet PINARBAŞI	Prof. Dr. Beşir ŞAHİN	Doç. Dr. Hüseyin AKILLI
DANIŞMAN	ÜYE	ÜYE

İmza: ……	İmza: ……
Prof.Dr. Recep YURTAL	Prof. Dr. Ertuğrul BALTACIOĞLU
ÜYE	ÜYE

Bu Tez Enstitümüz Makina Mühendisliği Anabilim Dalında Hazırlanmıştır.

Kod No:

Prof.Dr. Aziz ERTUNÇ
Enstitü Müdürü

ABSTRACT

Ph.D.THESIS

LARGE-AND SMALL-SCALE INSTABILITIES FOR SHEAR-LAYER ALONG A PERFORATED SURFACE

Coşkun ÖZALP

DEPARTMENT OF MECHANICAL ENGINEERING
INSTITUTE OF NATURAL AND APPLIED SCIENCES
UNIVERSITY OF ÇUKUROVA

Supervisor : Assoc. Prof. Dr. Ahmet PINARBAŞI
Year : 2006, Pages: 147
Jury : Assoc. Prof. Dr. Ahmet PINARBAŞI
Prof. Dr. Beşir ŞAHİN
Assoc. Prof. Dr. Hüseyin AKILLI
Prof. Dr. Recep YURTAL
Prof. Dr. Ertuğrul BALTACIOĞLU

The shear flow of a fully turbulent boundary layer along a perforated plate, which is bounded by a closed cavity on its backside, can give rise to highly coherent, self-sustained oscillations. These oscillations are characterized in terms of unsteady pressure fluctuations and quantitative images of the instantaneous and averaged flow structure using a technique of high-image-density particle image velocimetry (PIV).

Variations of the effective length L of the perforated plate show nearly invariant values of dimensionless frequency fL/U; in which f is the predominant frequency of oscillation and U is the freestream velocity. In fact, this relationship holds even when the diameter of the hole pattern is altered. Variation of the hole diameter D does, however, strongly influence the amplitude and degree of organization of the self-sustained oscillation. It is demonstrated that, as the hole diameter becomes larger relative to the inflow boundary layer thickness, the amplitude of the predominant spectral peak is substantially attenuated and, in a limitingcase, undetectable.

The present investigation also demonstrates that self-sustained oscillations can be effectively attenuated by three-dimensional surface elements in the form of vortex generators. In absence of the three-dimensional surface elements, a well-defined front of the unstable oscillation propagates along the surface of the plate. In presence of an appropriate surface element, the front is no longer detectable, and instantaneous and averaged defects of the streamwise velocity and surface-normal vorticity exist along the span of the plate.

Keywords: Self-sustained oscillations, Perforated plate, Vortex generators, PIV

ÖZ

DOKTORA TEZİ

GÖZENEKLİ YÜZEY BOYUNCA KAYMA TABAKASINDAKİ BÜYÜK VE KÜÇÜK ÖLÇEKLİ KARARSIZLIKLAR

Coşkun ÖZALP

ÇUKUROVA ÜNİVERSİTESİ
FEN BİLİMLERİ ENSTİTÜSÜ
MAKİNA MÜHENDİSLİĞİ ANABİLİM DALI

Danışman :Doç. Dr. Ahmet PINARBAŞI
Yıl :2006, Sayfa: 147
Jüri :Doç. Dr. Ahmet PINARBAŞI
Prof Dr. Beşir ŞAHİN
Doç. Dr. Hüseyin AKILLI
Prof. Dr. Recep YURTAL
Prof. Dr. Ertuğrul BALTACIOĞLU

Kapalı bir kavite üzerine yerleştirilmiş gözenekli bir levha boyunca oluşmuş tam türbülanslı sınır tabaka içerisinde kendiliğinden sürekli salınımlar oluşur. Bu çalışmada parçacık görüntülemeli (PIV) hız ölçme metodu kullanılarak anlık ve ortalama hız değerleri, girdap çizgileri, Reynolds gerilmeleri ve levha boyunca belli bir zaman aralığında ölçülen basınç değerleri ile bu salınımlar ifade edilmiştir.

Gözenekli levha boyunca akış yönünde ölçülen basınç değerleri neticesinde hesaplanan boyutsuz frekansın fL/U hemen hemen sabit kaldığı görülmüştür. Burada f salınımın frekansını U da serbest akış hızını ifade etmektedir. Aynı şekilde boyutsuz frekansın gözenek çapının değişmesiyle de sabit olduğu gösterilmiştir. Gözenek çapı D nin değiştirilmesi periyodik salınımlara neden olmakta ve etkili bir şekilde salınımların genliğini etkilemektedir. Sınır tabaka kalınlığına göre gözenek çapı arttırıldığında salınımların genliğinin sönümlendiği ve frekansın belirsiz hale geldiği görülmüştür.

Bu çalışmada ayrıca periyodik salınımların meydana geldiği gözenek çapında salınımların genliği üç boyutlu yüzey elemanlarından girdap üreticiler kullanılarak sönümlenmiştir. Girdap üreticilerin kullanılmadığı durumlarda gözenekli levha boyunca kararsız salınımlar oluşur. Girdap üreticilerin kullanılması ile bu salınımların genliği sönümlenmekte ve belirgin olan salınım frekansı belirsiz hale gelmektedir.

Anahtar Kelimeler: Salınımlar, Gözenekli levha, Girdap üretici, PIV

ACKNOWLEDGEMENTS

This list is endless if I have to thank all the people that made this work possible. First, I must acknowledge and sincerely thank my supervisor Assoc. Prof. Dr. Ahmet PINARBAŞI for his guidance, inspiration and encouragement.

I would like to thank Prof. Dr. Beşir ŞAHİN for his motivation, supports, help and encouragements.

I am grateful to Assoc. Prof. Dr. Hüseyin AKILLI for his advices and supports.

I would also thanks to my committee members Prof. Dr. Recep YURTAL and Prof. Dr. Ertuğrul BALTACIOĞLU.

A special thanks is in order to Prof. Dr. D. ROCKWELL for his financial support throughout the project for 15 months, advice, sharing his experience and creating research opportunities at Fluid Mechanics Laboratories, Department of Mechanical Engineering and Mechanics, Lehigh University , USA.

My sincere thanks go to Assist. Prof. Dr. Ali KAHRAMAN and his wife Fatma, Assist. Prof. Dr. Muammer ÖZGÖREN, M.M. YAVUZ, M. ELKHOURY, Ç. SEVER, E. ÇELİK and A. EKMEKÇİ for their continuous moral support and friendship in USA days.

I also want to thank Bülent YANIKTEPE, Research Assistants Cahit GÜRLEK, Atakan AKAR and Sedat YAYLA for their moral support, help and friendship.

In addition, I would like to thank all the staff of Department of Mechanical Engineering at Çukurova University.

Last but not least, I have my deepest appreciation to my beloved family especially my wife Sinem and my daughter Sudenaz for their love, encouragement, understanding and continuous supports.

NOMENCLATURE

D	:Hole diameter of perforated plate
ℓ_a	:Nominal spanwise length
ℓ_b	:Nominal streamwise length
H_p	:Height of vertical plate
H_w	:Depth of water in the channel
FFT	:Fast Fourier Transform
CCD	:Charged-Coupled Device
Nd:YAG	:Neodymium: Yttrium-Aliminum-Garnet crystals
DPIV	:Digital Particle Image Velocimetry
S_{xx}	:Auto-spectral density function
S_{xy}	:Cross-spectral density function
PIV	:Particle Image Velocimetry
u	:Streamwise velocity component
u_{rms}	:Root-mean-square value of streamwise velocity component
v	:Spanwise velocity component
v_{rms}	:Root-mean-square value of spanwise velocity component
$u'v'$	:Reynolds stress
h	:Heigth of vortex generator
t	:Perforated plate thickness
f	:Sampling frequency
w	:Gaussian kernel
x	:Coordinate in streamwise direction
y	:Coordinate in spanwise direction
z	:Coordinate in crossflow direction
L	:Effective length of perforated plate
N	:Frame number
U	:Free stream velocity
Re_θ	:Reynolds number based on θ

Greek Symbols

δ :Boundary layer thickness

θ :Boundary Layer momentum thickness

Δ_t :Sampling time

Δ_a :Spanwise spacing

Δ_b :Longitudinal spacing

ϕ :Phase Angle

Λ :Wavelength of vortex generator

ω :Vorticity

Operators

$\langle . \rangle$:Time-averaging

$\sim$:Fluctuations

TABLE OF CONTENTS Page

LIST OF FIGURES

1. INTRODUCTION

Cavities in aerodynamics surfaces can generate both steady and unsteady disturbances in otherwise uniform flow fields. Changes in static pressure distributions inside the cavity can result in large pressure gradients, and the unsteady flow can generate self-sustaining oscillations, which, in turn, generate acoustic tones that radiate from the cavity.

For the case of laminar flow past a cavity in absence of a perforated plate, it is well known that highly organized, self-sustained oscillations can occur. These cavity-type oscillations are undesirable from several perspectives. They are the origin of coherent and broadband sources of noise and, if the structure is sufficiently flexible, the flow induced vibration as well. Moreover, depending upon the state of cavity oscillations, substantial alterations of the mean drag may be induced.

1.1. Physics of Self-Excited Oscillations in Absence of Perforated Plate

The unsteady flow in and near cavity type geometries, which belongs to a basic class of flows susceptible to self-sustaining oscillations, occurs in a variety of applications such as slotted wall wind and water tunnels and slotted flumes, bellows-type pipe geometries, high head gates and gate slots and aircraft components. These cavity type oscillations are undesirable from the perspectives of inducement of structural vibration and fatigue, generation of noise, and drastic increases in mean drag on the body which houses the cavity. (Rockwell and Naudascher 1978)

Self-excited cavity oscillations have generic features that are as-addressed in the paper of Lin and Rockwell (2001). These features which are illustrated in Figure 1.1, a) interaction of a vorticity concentration with the downstream corner, b) upstream influence from this corner interaction to the sensitive region of the shear layer formed from the upstream corner of the cavity c) conversion of the upstream influence arriving at this location, and lastly d) amplification of this fluctuation in the shear layer as it develops in the streamwise direction.

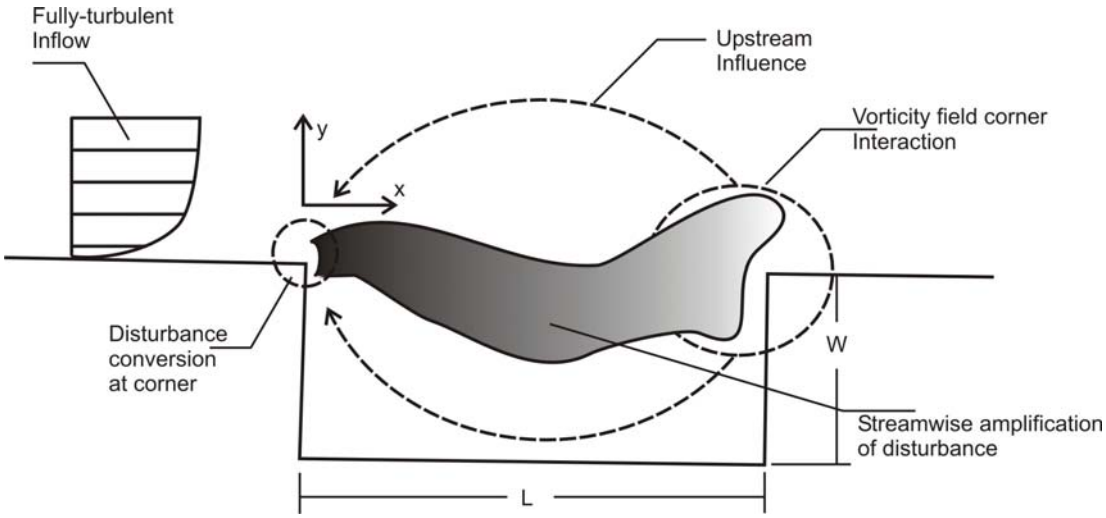

Figure 1.1a. Principal elements of self-sustaining oscillation of turbulent flow past cavity (Lin and Rockwell, 2001)

1.1.1. Interaction of a Vorticity Concentration

The interaction of the incident vorticity field (vortices) with the edge of the impingement surface is crucial in determining the type of upstream influence; this interaction is represented in Figure 1.1a. Since most flows at low Reynolds number involve vortices having relatively coherent concentrations of vorticity, much attention has been devoted to simplified models of vortex-corner/surface interactions, as addressed by Crighton (1975), Goldstein(1976) and Rockwell (1983). Categories of simulation of the interaction process involve: acoustic sources; point-vortex interactions; multiple vortex interactions; distributed vorticity-edge interactions, and idealized representations of the conversion process between an incident instability wave and resultant wave downstream of the edge. At higher Reynolds numbers, where the large-scale vortical structures may contain smaller scale concentrations of vorticity.

An additional, potentially important feature of the corner interaction is the possible coupling between the oscillating shear-layer and the recirculation vortex system within the cavity, illustrated in Figure 1.1b. This coupling may have a

significant influence on the so-called mass-exchange at the cavity corner. Global, instantaneous patterns of the flow structure are required to provide insight into the relationship between lateral deflections of the oscillating shear layer and changes in circulation of the recirculating vortex.

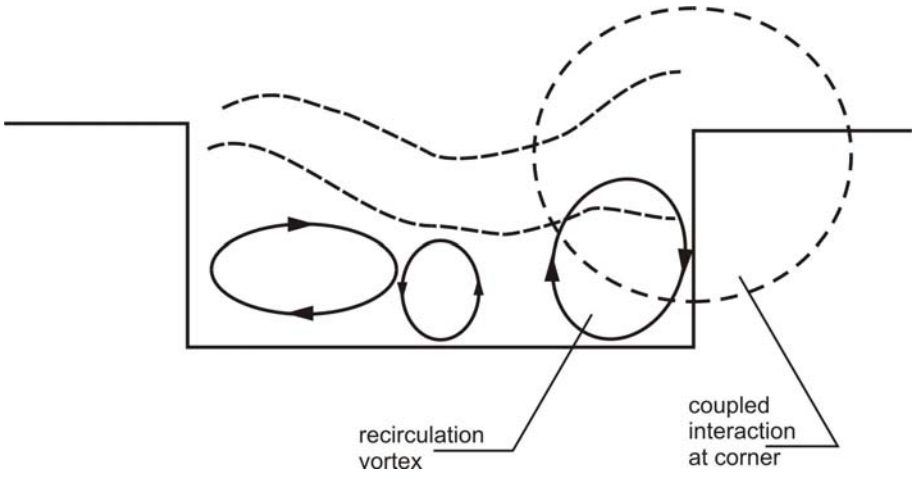

Figure 1.1b. Representation of coupled interaction at corner involving oscillating shear layer and recirculation vortex. (Lin and Rockwell, 2001)

1.1.2. Upstream Influence

The upstream influence originating from the unsteady flow surface interaction at x=L is shown in Figure 1.1a. It has its greatest consequence in the sensitive region near the shear-layer separation at x=0. For the conditions low-speed water flow the acoustic wavelength is much longer than the impingement length; therefore, this upstream influence is essentially instantaneous and can be described "pseudo-sound". That is changes in concentration of vorticity, associated with sudden changes in velocity and pressure at the impingement corner or edge result in corresponding velocity and pressure perturbations in upstream regions of the flow, having the greatest consequence in the highly sensitive region near shear-layer separation. (Knisely and Rockwell, 1981)

1.1.3. Disturbance Conversion at (Upstream) Corner or Edge

Effective conversion of disturbances incident upon the sensitive region of the shear layer separation to downstream traveling instability waves is essential if an oscillation is to be self-sustaining. Moreover, it sets the initial fluctuation level of the shear layer velocity fluctuations, thereby determining the streamwise extent of the exponential growth region of the fluctuations.

It is essential to convert the disturbances incident upon the sensitive region of the shear layer near separation to a downstream-traveling instability wave. For the case of a turbulent inflow, i.e. a fully turbulent boundary layer approaching the separation edge, this conversion process is particularly crucial. If the self-sustaining oscillation is to dominate, it is essential to efficiently convert the upstream influence to oscillations in the turbulent layer separating from the edge. (Rockwell, 1983)

1.1.4. Streamwise Amplification of Disturbances

Disturbance growth in the shear layer, represented by the distorted shaded region of Figure 1.1a is usually characterized by an initial region of exponential amplification followed by nonlinear distortion involving energy transfer between the fundamental and its higher harmonics.

Details of the mechanisms leading to streamwise amplification of disturbances are addressed by Rockwell and Naudascher (1980) and Rockwell (1983). An important unresolved issue is the degree to which a fully turbulent flow separating from an edge can exhibit coherent oscillations arising from amplification of applied disturbances. Although it has been established that free jets and mixing layers having fully turbulent conditions at separation can show coherent, large-scale vortical structures when disturbances of large amplitude are applied.

1.2.Oscillations Due to Flow Past a Slotted Wall Bounded by a Cavity

In comparison to the aforementioned investigations of flow past a single cavity in a continuous wall, very little is known of the shear layer unsteadiness due to flow past a slotted or perforated wall bounded by a cavity. The experiments of Betts (1972) involved flow past a slotted wall bounded by a cavity, but the slots were aligned in the streamwise direction. The entire configuration was located in an open (free-surface) water channel. Resonant fluid oscillations of the standing wave type occurred in the streamwise direction within the cavity, and they apparently coupled with a type of instability of shear layer along the slotted surface. In a related configuration, which involved a slotted-wall test section in water tunnel, with the slots also oriented in the longitudinal (streamwise) direction, a long-wavelength instability was generated, as described by King, Boyle and Ogle (1958).

1.3. Turbulent Shear Layer Past A Perforated Surface

Perforated surfaces, plates, and interfaces are often employed for attenuation of sound in internal flow systems. Such perforated surfaces are commonly found in the exhaust system of an automobile, within aircraft engines and compressors, as well as in reciprocating engine systems and ventilation units. Such perforated surfaces can be effective for attenuation of narrow-band noise or sound. Depending upon the parameters of the perforated surface and the inflow, adverse effects can occur, including the onset of ‘‘singing’’, or pure tone noise generation.

Figure 1.2 and 1.3 show an overview of turbulent shear layer past a perforated. It defines the central considerations using a sequence of schematics. In particular, this classification portrays both long- and short-wavelength instabilities past a perforated plate for: i) an isolated plate, which allows free entrainment through the individual perforations to the shear layer; ii) an adjacent cavity which induces recirculation flow, in order to satisfy the entrainment demands of the developing shear layer, and, in addition, to generate feedback of disturbances to the sensitive region of the shear layer near separation; and iii) an adjacent cavity which simulates

Helmholtz or standing wave resonance effects, as well as elastic wall effects, and their coupling with long- and short wavelength instabilities past the perforated plate.

Flow past a perforated plate can give rise to short wavelength instabilities that scale on the diameter of the perforation, or hole, and a recently documented long wavelength instability that scales on the length of the plate.

1.3.1. Long-Wavelength Instability

A long-wavelength instability is defined to occur at a scale much longer than the length of a perforation in the plate. Figure 1.2a shows this type of instability for the case where the shear flow entrains freely through the plate perforations from the outside environment. The regions of vorticity (not shown) that are generated when the entrained flow passes through each of the perforations may have cumulative effect on the instantaneous and averaged vorticity field of the shear flow, thereby altering its susceptibility to long-wavelength oscillations

Figure 1.2b shows the case of perforated plate bounded by a cavity. The entrainment demands are satisfied by a recirculation flow. The fluctuations of the volume bounded by the rigid cavity and the undulating shear layer across it, as well as the irrotational upstream influence (feedback) emanating from the cavity corner, may enhance the long-wavelength instability.

Figure 1.2c represents the occurrence of Helmholtz resonance, standing wave resonance, and elastic deflection of the cavity boundary. As shown, any one or a combination of these effects is simulated by perturbations of a portion of the cavity wall. If any of the elements of Figure 1.2c is present, they will enhance the tendency to form a long-wavelength instability.

Celik and Rockwell (2002) showed, for the case of a laminar inflow boundary layer, the occurrence of purely hydrodynamic, self-sustained oscillations of flow past a perforated plate of relatively high area ratio, which was bounded on its backside by a closed cavity. This study demonstrates that even in the case where the inflow boundary layer is fully turbulent, this type of long-wavelength instability would persist and, in fact, give rise to strongly coherent oscillations with sharply defined

peaks of both pressure and velocity spectra. In fact, the dimensionless frequency of these oscillations f_oL/U, in which f_o is the coherent frequency of oscillation, L is the length of the perforated plate, and U is the freestream velocity, at values of the order f_oL/U = 0.5 to 0.6. Remarkably, this dimensionless frequency corresponds to the classical first stage of purely hydrodynamic oscillations of flow past a cavity in absence of a perforated plate along its opening as addressed, for example, by Rockwell and Naudascher (1978) and Howe (1997b, 1998). Furthermore, in a more general sense, this type of log wavelength instability past a perforated surface has analogies with oscillations arising from free shear flow past a cavity, as addressed by Gharib and Roshko (1987) and Howe (1997b, 1998). In the event that the perforated plate is bounded by a cavity undergoing the equivalent of acoustic resonance, the aforementioned long wavelength instability can couple with a cavity mode, as described by Ekmekci and Rockwell (2003).

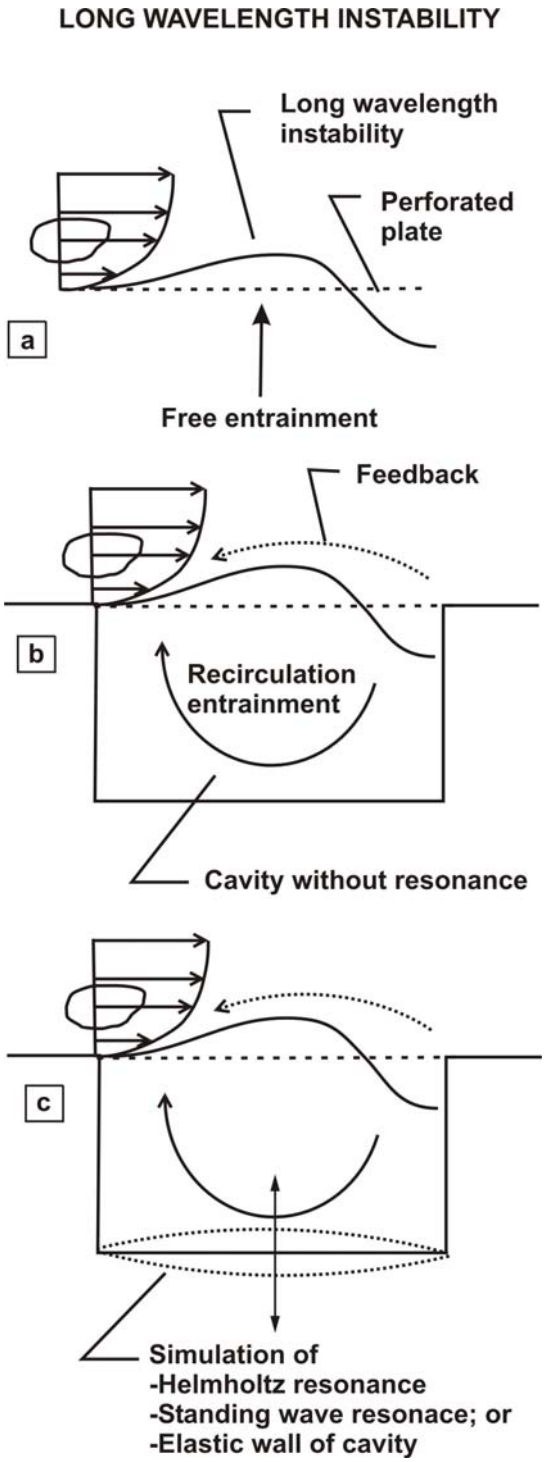

Figure 1.2. Overview of instabilities of turbulent shear flow past a perforated plate and influence of an adjacent cavity. Long-wavelength instability

1.3.2. Short-Wavelength Instability

A classical shear layer oscillation past a cavity may occur at a relatively short-wavelength, i.e. at a small scale, in each of the perforation openings, provided the thickness of the inflow shear layer is sufficiently small. This oscillation is represented in Figure 1.3a. Possible geometries of the perforations are indicated at the top of Figure 1.3a. It is expected that the coherence of the short-wavelength cavity oscillation will be a function of the perforation geometry.

In the event that the perforated plate is bounded by a cavity without resonant or elastic effects, as indicated in Figure 1.3b, the conditions for onset of a small-scale instability across each of the perforations may be altered. The modification of the entrained flow pattern, relative to that of Figure 1.3a, may effectively bias the mean position of the shear layer across each perforation, thereby altering its susceptibility to unstable oscillation.

As shown in Figure 1.3c, the occurrence of standing-wave or Helmholtz resonance within the cavity, or elastic deflection of the boundary of the cavity, will allow coupling the short-wavelength instability across each perforation, provided the corresponding frequencies are suitably matched.

Flow past a circular perforation, among an array of perforations, usually bounded on the backside by a defined cavity(ies) have been addressed by Meyer et all. (1958), Dean (1972), Adams (1974), Tsui and Flandro (1977), and Bauer and Chapkis (1977). In this series of studies, the generation of tones was generally attributed to the hydrodynamic instability of the shear layer past a single hole. Related investigations involve those of Ronneberger (1980), who experimentally addressed the physics of the unsteadiness past a circular hole, as well as Nelson (1982) and Howe (1997a), who focused on the broadband generation of fluctuations (noise). A still further aspect of this class of investigations is determination of the impedance of a perforated plate, with the aid of external excitation, as pursued by Dickey et al. (2001). Flow past inclined slats, i.e. louvers, with a cavity on their backside, can give rise to oscillations and noise generation that are analogous to those arising from flow past a perforated plate, as characterized by Bruggeman et al.

(1991) and Looijmans and Bruggeman (1997). Furthermore, Zoccola (2002) recently investigated the instabilities arising from one to three spanwise obstacles located along the mouth of a resonant cavity.

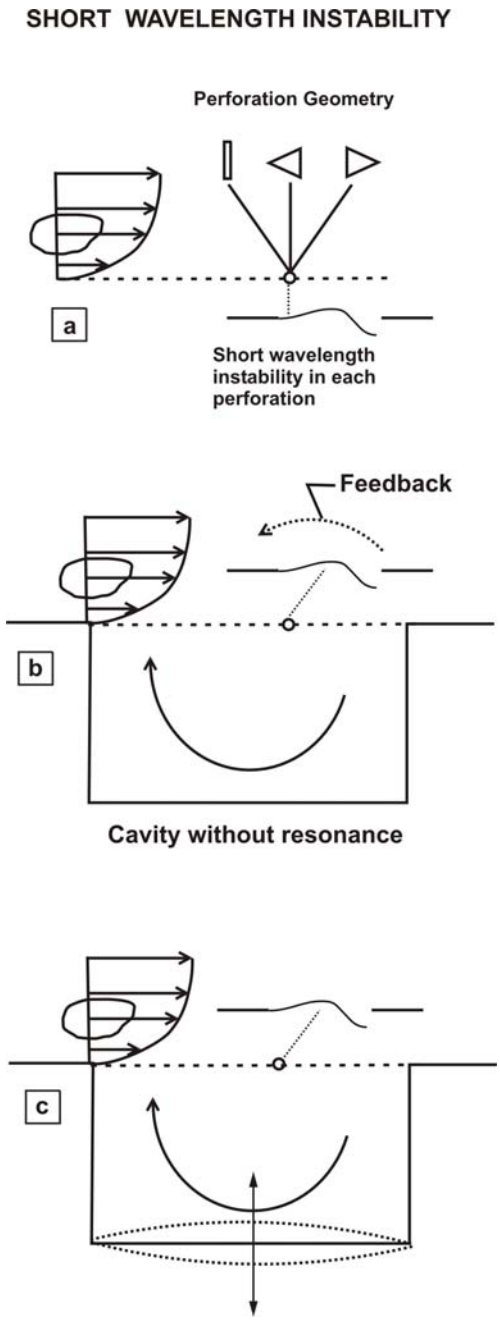

Figure 1.3. Overview of instabilities of turbulent shear flow past a perforated plate and influence of an adjacent cavity. Short-wavelength instability

2. LITERATURE SURVEY AND OUTLINE OF PRESENT STUDY

2.1. Literature Survey

Certain features of the flow instabilities due to shear layer past a perforated plate have their genesis in the shear flow past a single cavity in a continuous plate. It is therefore appropriate to review the literature and physical concepts associated with self-sustained oscillations past single cavities. Such isolated, single cavities usually have a simple rectangular configuration. Yet, a range of investigations on the instabilities generated due to flow past cavities of nonrectangular geometry are available, and can provide a basis for design of individual perforations in a perforated plate.

Turbulent shear flow past a perforated plate bonded by a closed cavity can give rise to highly coherent oscillations, which have wavelength of the order of plate length. (Celik and Rockwell, 2004)

In contrast to the foregoing cases, turbulent shear flow past a perforated plate bounded on one side by a cavity has not been investigated. The present experiment shows that this configuration gives rise to highly coherent oscillations, and pursues the physics of this class of instabilities in detail.

2.1.1. Self-Excited Oscillations in Absence of Perforated Plate

Self-excited oscillations in absence of perforated plate has been investigated several authors.

Extensive data of Ethembabaoglu (1973) taken in a water tunnel in the absence of cavitation have provided insight into several aspects of fluid dynamic oscillations. Spectrum of the pressure fluctuations was measured on the downstream cavity and boundary layer at separation was turbulent. Ethembabaoglu illustrates the variation of Strouhal numbers as a function of dimensionless cavity length L/W.

In contrast to the turbulent boundary layer study of Ethembabaoglu, Sarohia (1977) has taken measurements of mean and fluctuating flow fields for axisymmetric

type cavities where the boundary layer at separation was laminar. Sarohia characterized a minimum cavity length below which cavity oscillations did not occur. Minimum dimensionless cavity length for existence of fluid-dynamic oscillations versus cavity depth for axisymmetric type cavity was plotted.

Unlike the free shear layer, the self-sustained oscillation of the cavity shear layer tends to be much coherent. The coherent oscillation is caused by feedback condition reflected from the down stream surface upon which the shear layer impinges. The crucial physics of self-sustained oscillations of impinging shear layers are described in detail in the invited articles of Rockwell and Naudascher (1978,1979) and Rockwell (1983).

Rockwell and Knisely (1979) visualized the spanwise structure of the shear-layer along the mouth of a cavity using the hydrogen bubble technique. In their investigation the free-shear layer impinged upon the downstream corner of the cavity. The three-dimensional character of an oscillating cavity flow was examined by generating sheets of timelines at various locations in the mean shear layer along the mouth of the cavity. A Laser-Doppler anemometer was used in conjunction wit a Fourier analyzer to acquire detailed power spectra at severe locations in the free stream and in the boundary layer separation.

Details of the mechanisms leading to the streamwise amplification of disturbances are addressed by Rockwell and Naudascher (1980) and Rockwell (1983). An important unresolved issue is the degree to which a fully turbulent flow separating from an edge can exhibit coherent oscillations arising from amplification of applied disturbances. Although it has been established that free jets and mixing layers having fully turbulent conditions at separation can show coherent, large-scale vortical structures when disturbances of large amplitude are applied, no equivalent studies have been undertaken of the amplification characteristics in the shear layer of an impinging flow such as a jet-edge or cavity configuration. The closest indirect evidence that such amplification may be attainable is suggested by the experiments of Ethembabaoglu(1973); there are questions, however, whether the incident boundary layer was sufficiently turbulent.

Howe (1980) studied the linearized theory of unsteady flow through a two-dimensional aperture in a thin plate in the presence of a grazing mean flow on one side of the plate. The mean shear layer is modeled by a vortex sheet. The linear theory of the interaction of a mean shear layer with a two-dimensional aperture reveals be imposed at the leading or upstream edge of cavity. The theory is used to examine the effect of mean shear on the diffraction of sound by a perforated screen, and to predict the spontaneous excitation and suppression of self-sustained oscillations in a wall-cavity beneath a nominally steady mean flow.

A self-sustained low-frequency component in an impinging shear layer was investigated by Knisely and Rockwell (1981). The subjects of this study was investigation of oscillations of a cavity shear layer, involving a downstream-traveling wave and associated vortex formation, its impingement upon the cavity corner, and upstream influence of this vortex-corner interaction. In this investigation, the disturbance arriving at the upstream separation edge from the downstream corner region was modulated. Knisely and Rockwell (1981) addressed variations of the fundamental and low-frequency components associated with amplitude modulation as a function of impingement length L and free-stream velocity U; the examination of nonlinear interaction between frequency components; the source of dominant upstream influence; the nature of growth of the amplitude-modulated instability wave traveling downstream through the shear layer along the mouth of the cavity and, finally, over all phase conditions between separation and impingement for the fundamental and low-frequency components of the amplitude modulated wave. To determine the behavior of possible low-frequency components, as well as to confirm that of the fundamental, two sets of pressure fluctuation spectra were recorded. Firstly free-stream velocity was held constant while the impingement length was varied. In the second serious, the impingent length was fixed and the free-stream velocity varied.

Gharib and Roshko (1987) studied self-sustained, periodic oscillations of the cavity shear layer with low cavity drag. A free-stream velocity was kept 23 cm/s value. For the purpose of spectral analysis and phase measurement hot film probe and anemometer in conjunction with a r.m.s. meter were used. Throughout the phase-

angle or cross-correlation measurements a sampling rate of 200 per second limited by 400 samples and corresponding Nyquist frequency of about 30 was used. The velocity field of the cavity was measured by a two-component, two-colour, frequency-shifted laser-Doppler velocimeter. At U=23 cm/s the boundary layer upstream of the cavity was laminar and had a shape factor $H=\delta_0/\theta_0=2.5$ where δ_0=1.0mm (displacement thickness), θ_0=0.41 mm and $Re_{\theta_0} = 95$. The variation of fundamental frequency with b/θ_0 at a fixed edge velocity was illustrated to characterize self sustained oscillation in the cavity shear layer. They explained that oscillation starts at $b/\theta_0 \cong 81$, which was the minimum cavity with for their experiments. Frequency variation of cavity shear layer with varying cavity width was plotted at free stream velocity. According to this illustration the fundamental frequency of oscillation decreases as b/θ_0 increases. In this graph also a transition region was shown at $b/\theta_0 \cong 122$. The flow visualizations and flow-field measurements were presented in the low-drag regime.

From a design standpoint, it is important to know the impedance of a perforated plate that is subjected to tangential inflow. Dickey et al. (2001) employed a loudspeaker to induce pure tone, external excitation of a side branch, with a perforated plate mounted along its open end. The grazing flow was represented in terms of the friction velocity, and the distinctive features of a circular orifice, relative to a louver, were characterized. Grazing flow past perforated plates can also generate substantial broadband noise, even when pure tone generation is not an issue. Nelson (1982) employed experimental data in conjunction with a model to predict the broadband noise level.

Perrira and Sousa (1993) use a finite difference numerical scheme with temporal discretization. The numerical scheme based on finite differences approximation with an explicit quadratic Leith-type of temporal discretization. Patterns of instantaneous streamlines and vorticity contours within the cavity suggest a relationship to the unstable shear layer past a cavity. More recently, Pereira and Sousa (1995) combined the results of their unsteady numerical simulation with pointwise laser-Doppler measurements at crucial locations in the cavity, and suggest,

for their particular cavity configuration and flow conditions, occurrence of coupling between the shear layer and the dynamics of the recirculation flow field within the cavity. Figure 2.1 shows dye visualization corresponding to their experiments and representative images of the numerical simulation, visualized using passive particles (streak lines). An important observation is that their numerical simulation shows occurrence of an instability having a much shorter wavelength than the overall wavelength of the entire unstable shear layer along the mouth of the cavity.

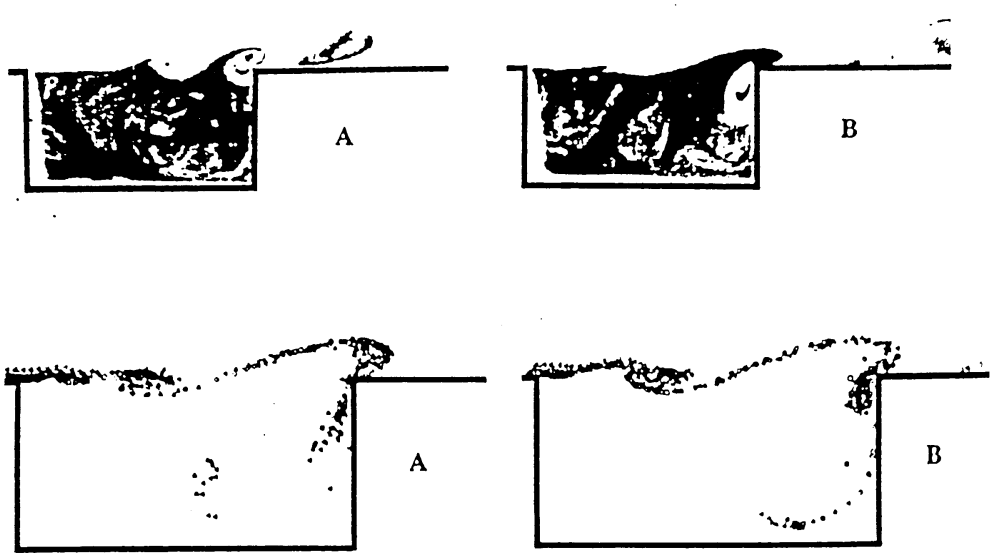

Figure 2.1. Dye visualization (experiment) and passive particle visualization (numerical) representing streaklines for flow past a cavity. (Pereira and Sousa, 1995)

Lyer et.al. (1998) examined unsteady turbulent shear layer formed behind a forward facing step using single-frame, double-pulsed planar Particle Image Velocimetry. They investigated both cavitating and non-cavitating flows at two different Reynolds numbers. The average shear layer thickness was determined from the PIV data and compared for the two Reynolds numbers and the two cases of cavitating and non-cavitating flows. Their preliminary data suggest that the thickness of the cavitating shear layer grows faster than that of a non-cavitating flow.

Kuo and Chang (1998) investigated the influence of a horizontal top plate on self-sustaining oscillation over a rectangular cavity. Due to presence of top plate the self-sustaining oscillation of the shear layer was promoted most effectively. They

employed laser sheet technique to show the self-sustaining oscillatory flow patterns. Dimensionless mean velocity profiles were illustrated to compare with theoretical tanh-velocity. They also showed velocity spectral density measured along the cavity shear layer. Kuo and Chang clarified that the effectiveness decreases as the leading edge of the top plate moves downstream away from the most sensitive region. They found that significant flow acceleration near the most sensitive region of the cavity shear layer reduces the local momentum thickness and enhances the receptivity of the shear layer to the feedback effect. Therefore, stronger feedback from the downstream edge of the cavity and high sensitivity to the feedback at the most sensitive region of the cavity shear layer are key mechanisms to promote the oscillation of the shear layer across the cavity mouth.

Kuo, Huang and Chang (2000) investigated the mechanism leading to enhanced self- sustained oscillations within the cavity by experiment at a Reynolds Number $Re_{\theta 0} = 171 \pm 5$. Three mechanisms are found to possibly modify the shear layer instability across the cavity. First of all, insertion of a horizontal cover plate above the cavity does impose a favorable streamwise pressure gradient that accelerates the flow across the cavity. This flow acceleration increases the amplification rate of shear layer instability. Second, the boundary layer characteristics (both the frequency band and the fluctuating amplitude) may also provide another opportunity to perturb the shear layer instability. Third, the shear layer is deflected into the cavity and leads to strong back. They investigated all three mechanisms are equally important when the leading edge of the cover plate is positioned above the cavity mouth.

Kuo and Huang (2001) concluded the influence on the oscillating characteristics of a cavity shear layer by introducing either a sloped bottom or a flow path modifier at the bottom of the cavity. Laser Doppler velocimetry and laser sheet technique were employed to perform the quantitive velocity measurement and the qualitative flow visualization respectively. They found that in addition to the feedback effect, the upstream moving part of the recirculating flow inside the cavity is either negatively or positively sloped, the oscillating characteristics of the cavity shear layer are modified to different extents. They used different cavity models

which have positively/negatively sloped bottoms and the fence at the bottom of the cavity acts as a flow path modifier.

An important issue is to degree to which a fully turbulent flow separating from the leading-corner of the cavity can undergo self-excited, coherent oscillations that arise from amplification of disturbances. This amplification occurs in the same spirit as the amplification process in an initially laminar shear layer. It is entirely possible that such oscillations may be detectable in a turbulent shear layer. This issue addressed, in a preliminary sense, for purely hydrodynamic oscillations in the works of Lin and Rockwell (1999,2001).

Lin and Rockwell (2001) characterized unsteady flow structure due to turbulent boundary layer past a rectangular open cavity using a cinematographic technique of high-image-density particle image velocimetry. Their study involved instantaneous global flow structure past and within the cavity due to an inflow boundary layer. The time-averaged turbulence statistics will be interpreted in terms of these instantaneous flow patterns. They expressed the time averaged characteristics of the shear layer along the cavity in terms of Reynolds stresses, vorticity and velocity. Reynolds stresses demonstrated that the stresses of the shear layer along the cavity rapidly dominates those of the approach turbulent boundary layer. The patterns of time averaged vorticity show that the region of separation from the leading corner of the cavity dominates all other regions of the flow field, including shear layer along the cavity and the recirculating flow within the cavity.

Rowley et. all. (2002) used numerical simulations to investigate the resonant instabilities in two-dimensional flow past an open cavity. Navier-Stokes equations have solved directly for cavities with laminar boundary layers. This study focused to investigate the two regimes, above shear layer mode and wake mode in two dimensional subsonic flow over a rectangular cavity. Rowley et. all explained that the shear layer mode is characterized by the feedback process the roll-up vorticity in the shear layer, impingement and scattering of acoustic waves at the downstream edge, upstream acoustic wave propagation, and the receptivity of the shear layer to acoustic disturbances. In wake mode the shed vortex has dimensions of nearly the

cavity size, and as it is forming, irrotational free-stream is directed in to the cavity, impinging on the cavity base.

Kuo and Huang (2003) investigated the effect of a surface mounting located on the upper plate on the oscillating flow structure within the cavity. They performed all the experiments in a recirculating water channel. Different values Reynolds numbers were taken which are based on the uniform velocity and momentum thickness at the upstream edge of the cavity. At the upstream edge of the cavity, the streamwise velocity profiles were measured quantitatively along the spanwise direction. Hydrogen bubble technique was used both the quantitative velocity measurements along the spanwise direction and the qualitative top view flow visualization. Kuo and Huang addressed that first extra blockage of the surface mounting on the upper plate creates a streamwisely elongated and transversely expanded recirculating region underneath the upper plate. Second, higher velocity fluctuation in expanded recirculation region provides externally perturbation to trigger the separated shear layer to become more unstable. Third, the transversely expanded recirculating region further deflects the unstable shear layer into cavity, leading to stronger feedback on the cavity shear layer.

Kuo and Jeng (2003) located a circular cylinder of small diameter (d=4mm) very close to upstream edge of cavity, to generate the local periodic excitations in the form of oscillatory rotation about its center with various angular amplitudes and frequencies. All the their experiments conducted in a recirculating water channel at three different Reynolds numbers that are based on the momentum thickness at the upstream edge of cavity. They used LDV system and the laser sheet technique to perform the quantitive velocity measurement and qualitative flow visualization.

2.1.2. Self-Excited Oscillations in Presence of Perforated Plate and Slotted Plate

Meyer et al. (1958) found that self-excited generation of tones could occur over two ranges of flow velocity, one corresponding to resonance coupled with the Helmholtz resonator on the opposite side of the perforated plate, and another coupled with a resonant mode of the main flow duct. Dean (1972) and Adams (1974) also observed self-excited pure tone generation due to flow past perforated liners. The possible importance of the scale and spacing of the individual perforations was pointed out by Dean (1972). Tsui and Flandro (1977) report the occurrence of ‘‘singing’’, which they attribute to vortex shedding past the holes; they found that this phenomenon could be due to coupling with either a resonant mode of the cavity on the backside of the plate or an acoustic mode(s) of the main flow duct. Bauer and Chapkis (1977) also investigated various features of pure tone noise generation due to flow past perforated surfaces. The importance of the instability past an individual hole, or orifice, which can involve vortex shedding, was pursued by Ronneberger (1980). In his investigation, he applied an external perturbation to a single rectangular cavity; in order to induce an oscillation of the interface along the cavity, with the intent of simulating the self-excited vortex shedding that occurs during coupled resonance in an actual orifice of a perforated plate.

King, Boyle and Ogle (1958) observed self-induced oscillations caused by resonant feed-back in a circular slotted-wall subsonic wind tunnel and calculated the convection velocity from the theory of hydrodynamic stability. They also confirmed that the oscillating pressure was in phase throughout the outer chamber and that the phase change of the convected perturbation along the length of the working section.

Betts and Binnie (1966) and Binnie and Cloughley (1970) demonstrated that larger models can be satisfactorily accommodated in an open water-channel if the walls and bottom of the channel contains longitudinal slots which connect the working section to a large open reservoir surrounding the channel and containing effectively stationary water. In the earlier work a form of small-induced oscillation was reported. This consisted of a longitudinal standing wave oscillation (first ‘sloshing’ mode) in the outer chamber, with the surface variations in phase across the

outer chamber and the slotted working section; the amplitude of the standing wave was slightly larger in the working section than at the same longitudinal position in the outer chamber. Although the instability was eliminated at the time, it appeared worthwhile to investigate this further to gain a better understanding of the mechanism involved and to determine the likelihood of its occurrence in a larger scale channel.

The experiment of Betts (1972) involved flow past a slotted wall bounded by a cavity, but the slots were aligned in the streamwise direction. Theoretical and experimental results were compared and good agreement between the theoretical and experimental results was obtained.

If the perforated plate undergoes vibrations, then a number of interesting issues arise. As found by Howe (1996), vorticity generation in the apertures of a perforated plate subjected to a grazing flow can lead to dissipation of plate vibrations. In a further theoretical study, Howe (1997) determined the sound production arising from both turbulence and vortex shedding. Maunget et al. (1999) performed experiments on a vibrating perforated plate in a flow at high Reynolds number, and characterized the damping characteristics.

The importance of perforated plates is not limited to low speed applications. Occurrence of high noise levels in transonic wind tunnels is well known, and recent results related to suppression of edge-tone type noise in the systems is described by Medved (1993).

A further, related configuration, which can be associated with pure tone generation, involves either one or three spanwise (two-dimensional) obstacles across the opening of a resonant cavity, as addressed by Zoccola (2002). An acoustic resonant mode of the cavity was excited by, and coupled with, the flow instability(ies) along the obstacle(s). In nearly all of the foregoing investigations, emphasis has been on the genesis of either pure tone or broadband noise in relation to localized interaction of the separated shear flow past individual holes, orifices, or gaps. In the case of pure tone generation, the inherent instability of the separated shear layer past, for example, the hole should scale on a characteristic length of the

inflow boundary layer and is directly influenced by the diameter, or streamwise, length of the hole.

Celik and Rockwell (2002) showed, for the case of a laminar inflow boundary layer, the occurrence of purely hydrodynamic, self-sustained oscillations of flow past a perforated plate of relatively high area ratio, which was bounded on its backside by a closed cavity.

Figure 2.2 shows patterns of vorticity and streamline topology for a free-shear layer along the opening of a cavity of streamwise length L (left-hand column), in comparison with the instability along the perforated plate of effective length L (right-hand column), which is bounded by the same cavity.

Celik and Rockwell (2002) addressed that in absence of the perforated plate, the time sequence of patterns of phase-averaged vorticity $\langle \omega \rangle_p$ show a highly ordered series of vorticity concentrations, The patterns of phase-averaged streamlines $\langle \psi \rangle_p$, shown at the bottom of the left-hand column of Figure 2.2, are in a reference frame moving with the convective speed of the vorticity concentrations. They indicate well-defined foci (centers of vortices) and saddle points (intersecting streamlines). The patterns of both streamline topology and vorticity are substantially distorted along the leading portion of the impingement plate. In the right-hand column of Figure 2.2, the phase-averaged patterns of vorticity $\langle \omega \rangle_p$ show development of a single concentration, which is also distorted upon encounter with the leading region of the impingement plate. The corresponding pattern of streamline topology shows well-defined foci and saddle points. The middle image of the streamline topology in the right-hand column shows that the streamwise distance between successive saddle points is larger than for the case of no perforated plate given in the left-hand column; this observation corresponds to the elongated nature of the vorticity concentrations. Furthermore, distributions of time-averaged velocity are indicated on the schematic of the perforated plate system shown in the right-hand column. These distributions have the form of a bounded shear layer with no inflection point, in contrast to the well-known in flexional shape of the separated shear layer in absence of the perforated plate.

Ekmekci and Rockwell (2003) addressed the coupling between the self-excited instability past a slotted plate and a resonant mode of a bounding cavity, with particular emphasis on the flow physics. They employed a technique of high-image-density particle velocimetry to provide whole field representations of the instantaneous flow structure during an oscillation cycle. They investigated shear flow past a slotted plate, which can give rise to highly coherent, self-sustained oscillations when coupling occurs with a resonant mode of an adjacent cavity. They explained in their study, the distinctive feature of these oscillations is that the wavelength of the coherent instability along the plate is of the order of the plate length. This observation is in contrast to previous investigations of flow past perforated or slotted surfaces, where the instability scales on the diameter of the perforation or the gap length of a slot. The present oscillations occur even when the inflow boundary layer is turbulent and an inflectional form of the shear flow cannot develop along the cavity opening, due to the presence of the slotted plate. Instigation of a resonant mode of the cavity, in conjunction with an inherent instability of the shear flow along the plate, gives rise to ordered clusters of instantaneous vorticity and instantaneous velocity correlation. During the oscillation, ejection of flow occurs from the cavity to the region of the shear flow; this ejection is in accord with the convection of the large-scale cluster of vorticity along the slotted plate. This oscillation can be effectively detuned by adjusting the inflow velocity, such that the inherent instability of the shear flow past the slotted plate is no longer coincident with the resonant frequency of the cavity.

Recently, Celik and Rockwell (2004) have shown that a long wavelength, self-excited instability can arise due to essentially laminar inflow past a perforated plate.

In essence, they found that the wavelength of the instability is much larger than the diameter of the individual holes in a perforated plate of relatively large open area This instability occurred in the presence of a large, single cavity on the backside of the perforated plate, and the system parameters were such that neither acoustic resonance nor wall elasticity effects were present; that is, the self excited oscillation was due to purely hydrodynamic effects. This preliminary investigation was limited

to oscillations arising in a laminar inflow; in contrast, the present investigation addresses self-excited oscillations arising within a fully developed turbulent inflow. Furthermore, the investigation of Celik and Rockwell (2004) focused on a single hole diameter of the perforated plate, and addressed only instantaneous representations of the flow patterns, along with determination of the predominant frequency of oscillation as a function of effective length of the perforated plate. In contrast to this study present investigation addresses variations of hole diameter in the context of time-averaged statistics of the flow unsteadiness.

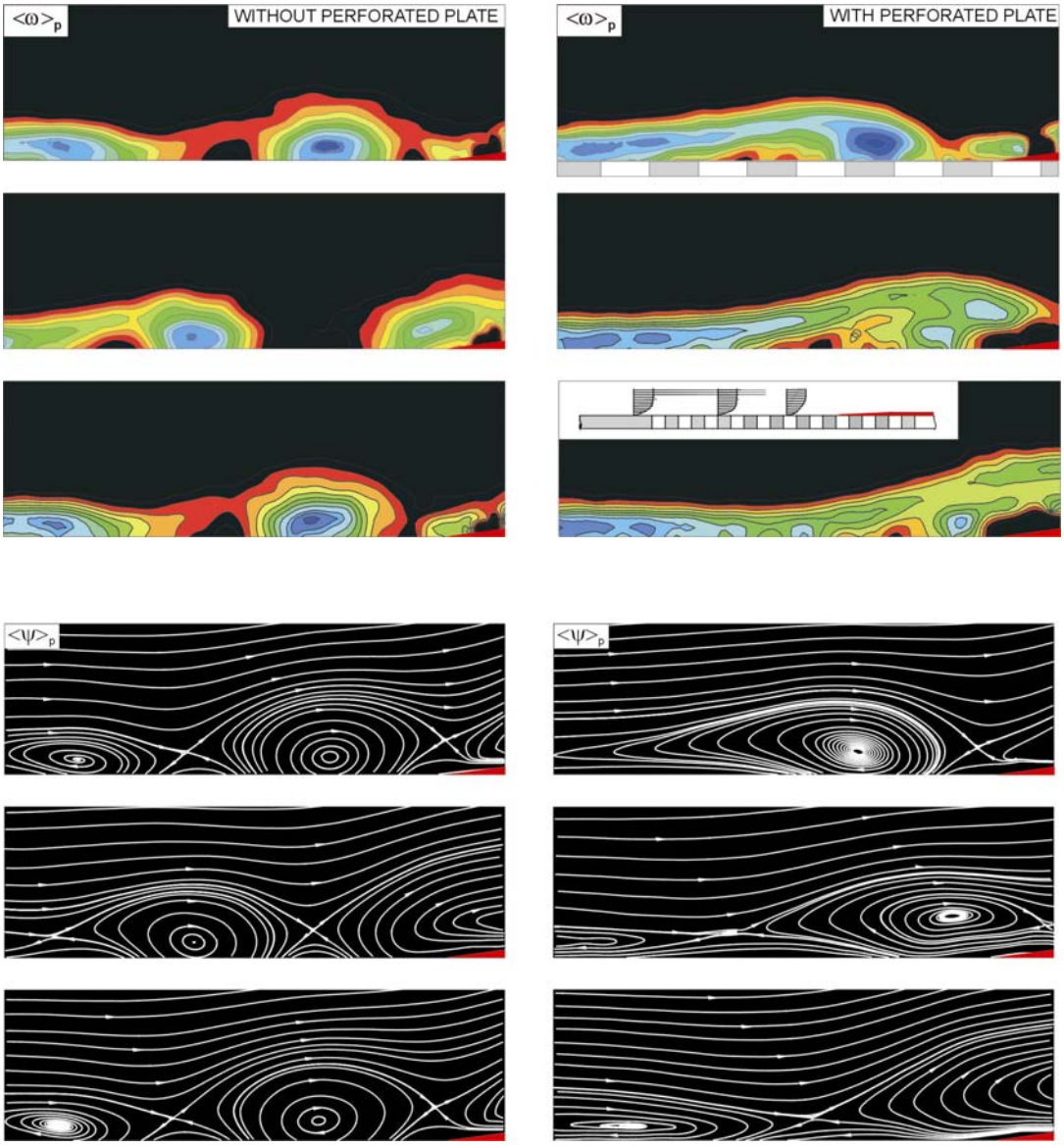

Figure 2.2. Patterns of phase-averaged vorticity and streamline topology for unstable flow past a cavity of length in absence of a perforated plate (left-hand column) and with a perforated plate of effective length L, which is defined as the distance from the upstream boundary of the perforated plate to the impingement edge (right-hand column). In both cases, the field of view corresponds to 0.7L, as defined by the rectangular area in the schematic. (Celik and Rockwell, 2002)

2.1.3. Shallow Cavities

The mean and fluctuating properties of the flow field above and within a shallow wall cavity exhibit interesting fluid dynamical properties and the fluctuation can lead to sound generation. Grace et. all. (2004)

The basic characterization of cavity flow has been the focus of a number of investigations. Researchers such as Sarohia (1977) and Ahuja and Mendoza (1995) have tired to identify a characterizing parameter that governs the onset of resonance or shallow cavities. Sarohia considered a shallow cavity with a laminar upstream boundary conditions. In contrast to Sarohia, Ahuja and Mendoza studied turbulent upstream boundary conditions.

Zhang, Chen, Rona and Edwards (1999) studied the unsteady flows over a shallow cavity at Mach 1.5 and 2.5 numerically. The effects of leading edge compression ramps, expansion surfaces and mass injection on supersonic shallow cavity flow oscillations are investigated through solutions of Short-time Reynolds-Averaged Navier-Stokes equations with the effect of turbulence modeled by a two-equation k-ω model. This study has provided insight into major flow physics and clarified confusion in the interpretation of the effectiveness of different means for the unsteady flow control. They clarified that when an expansion surface is employed, the mean pressure drag coefficient is also increased slightly. When the flow is attached to the surface, the major flow physics are similar to the baseline case. When the mass injection is introduced, a passive pressure response is observed at the leading edge, producing local vorticity and shedding and lastly when a compression ramp is introduced at Mach 1.5 a strong flapping motion leads small changes in the frequency and sound pressure level in the cavity. At mach 2.5, a weak shear layer instability produces a reduction in the sound pressure level, and increased distance between the leading edge and the trailing edge produces a reduction in frequency.

Grace and et. all.(2004) measured mean and turbulent flow fields within and downstream of a non-resonating shallow cavity subject to low Mach number flows with both laminar and turbulent upstream boundary layers. Their experiments were conducted on a fixed cavity geometry and boundary layer trip was used to change the

inflow boundary layer. The cavity was of length 0.1m and depth 0.025m, giving length-to-depth ratio of L/D=4. Flow measurements were taken using both a cross-wire anemometer and a two-component laser Doppler velocimeter. To obtain frequency information within the cavity a single hot-wire anemometer and microphone were used. Mean velocity vector plots and comparison of laminar and turbulent boundary layer profiles were illustrated. Grace et. all were carried out their experiments at 7.5m/s and 15 m/s velocities for both laminar and turbulent upstream boundary conditions, which leads to Reynolds numbers based on length of the cavity of roughly 50,000 and 100,000. Spectral characteristic of the flow within the cavity were investigated and power spectral density versus St. Number graph was showed. They were comparisons their results with some previous investigations such as Gharib and Roshko (1987), Sarohia (1977) and Ahuja and Mendoza (1995).

2.1.4. Alteration Of Flow Structure Due To Three-Dimensional Surface Elements

Three dimensional surface element such as vortex generators have long been used to control flow separation by increasing the near-wall momentum through the momentum transfer from the outer (free-stream) flow to the wall region. Lin (2002). First introduced by Taylor (1947) these devices consisted of a row or small plates or airfoils that project normal to the surface and are set an angle of incidence, β, to the local flow to produce an array of stream-wise trailing vortices. Vortex generators have been used to delay boundary layer separation, to enhance aircraft wing lift and to avoid or delay boundary-layer separation.

Vortex generators have been effectively employed for alterations of the structure of separated flows. Keller and Escudier (1979) demonstrated the attenuation of self-sustained oscillations of flow past a cavity, with emphasis on the effect of incidence angle of the generators. As discussed by Kuethe (1972), in a study of generators at the trailing edge of an airfoil, it is possible to distinguish counter and corotating regions of streamwise vorticity, depending upon the spacing between

generators, all of which are parallel to each other and inclined at the same angle of attack.

Karadogan and Rockwell (1983) characterized the effect of dimensionless height and wavelength of vortex generators and attenuation of the self-sustained oscillations of an axisymmetric jet flow through a cavity at the end of a long pipe. They assessed several attenuation configurations to involve generating streamwise vorticity, dephasing the azimuthal coherence of jet and reducing the rigidity of the jet seperation edge. They involved a long pipe of length l and diameter D terminated by an axisymmetric cavity of length L. Hot wire measurements were taken along the centerline of he cavity and also pressure measurements were acquired within the cavity. Various categories of attenuators (vortex generators, azimuthal dephasors and compliant boundaries) were depicted.

McCormick (1992) demonstrated that the low-profile vortex generators significantly suppress the shock induced separation bubble and improve the boundary-layer characteristics downstream of the shock as the boundary layer becomes thinner and contains lower mixing loses. McCormick explained that the passive cavity substantially reduces the total pressure loss through the shock system and thus wave drag, by causing a more isentropic compression over a larger area.

A passive control method using vortex generators was employed to increase mixing in jet flows by Hu et. al. (2000). Planar Laser Induced Fluorescence and Particle Image Velocimetry were used to accomplish flow visualization and velocity field measurements of the jet mixing flows simultaneously.

Another recent studies Lin et.al. (2002) involves the detailed flow measurements of an embedded streamwise vortex downstream of a single low-profile vane-type vortex generators placed within the turbulent boundary layer over a flat plate. Lin (2002) presented a review of boundary layer flow seperation control by a passive method using low-profile vortex generators. In this review the generators were defined as those with a device height between 10% and 50% of the boundary layer thickness. Practical advantages of low-profile vortex generators such as their inherent simplicity and low device drag were demonstrated.

2.2. Unresolved Issues

An issue of central importance is whether highly coherent, self-sustained oscillations, which have a relatively long wavelength, can occur due to a fully turbulent inflow past a perforated plate. If the inherent instability mechanism of the shear flow past the perforations of the plate is sufficiently robust, then one expects it to rapidly emerge above the background turbulence of the inflow boundary layer. In addition, the effect of the diameter of the individual holes in the perforated plate has not been addressed. If the open area ratio of the perforated plate is held constant, while the hole diameter is varied, it should be possible to determine the effect of diameter on the degree of organization of the self-excited oscillations.

- If a self-excited instability does arise, even in presence of turbulent inflow, the issue arises as to whether the frequency can be scaled according to an effective length of the perforated plate, irrespective of the hole diameter. If so, this would reinforce the view of the instability as a longwavelength phenomenon.
- Characterization of the instability in terms of patterns of instantaneous and averaged Reynolds stress has not been pursued. Furthermore, the spectral content of the fluctuating velocities across the shear flow has not yet been addressed. This type of assessment, in conjunction with a cross-spectral analysis to yield phase information, could provide insight into the wave-like character of the fluctuation across the nominally turbulent shear flow.
- Instantaneous and averaged statistical representations of the unsteady flow pattern in the vicinity of the trailing-end (edge) of the perforated plate are particularly important. If indeed long wavelength instability does occur along the perforated plate, and if it scales on the plate length, the existence of a feedback mechanism would be suggested; it must have its origin in an unsteady flow mechanism at the end of the plate.

Consideration of the foregoing observations of self-sustained oscillations, as well as methods for their attenuation, leads to the definition of central, unresolved issues for the present case of self-excited oscillations past a perforated plate.

- The recent characterization of highly coherent, self-sustained oscillations of flow past a perforated plate, which is bounded on its backside by a closed cavity, raises the issue whether modification of the spanwise coherence of the oscillation on the high-speed (front side) of the perforated plate can lead to effective mitigation of the self-sustained oscillation. That is, it is not yet known whether an appropriate type of surface treatment, which would induce localized velocity and vorticity defects along the span of the plate, can lead to attenuation of this type of robust oscillation.
- In the event that attenuation can be achieved, the minimum height of the three-dimensional elements, as well as the effective spanwise wavelength of the elements, both with respect to the inflow boundary layer momentum thickness, has not been characterized.
- The magnitude of the local velocity defect and thereby the surface normal vorticity, is expected to decay with streamwise distance along the perforated plate, thereby raising the question of the maximum plate length, relative to the inflow momentum thickness, for which oscillations can be effectively attenuated.

2.3. Objectives of Present Investigation

This investigation focuses on turbulent boundary layer incident upon a perforated plate, which is bounded on one side by an enclosed cavity and on the other side by a freestream, can give rise to highly coherent, self-sustained oscillations. The overall aim of this investigation is to address the unresolved issues described in the foregoing, by use of a technique of high-image-density particle image velocimetry, in conjunction with pressure measurements at the trailing end of

the perforated plate. The following steps were taken during the present investigations.

- Four different plates are employed, with whole diameters of D = 6.4 mm, 12.4mm, 19.7mm and 25.4mm. The thickness of the plate is maintained constant at t = 11 mm for all experiments. Furthermore, the open area ratio of the plates was maintained constant at 69 %.
- Quantitative imaging, using high-image-density particle image velocimetry is employed in conjunction with pressure measurements to characterize the physics of these oscillations.
- Instantaneous, time-averaged and phase-averaged representations of velocity, vorticity and Reynolds stress, as well as spectra and cross-spectra evaluated at key locations in the flow allow characterization of the oscillations.
- Measurements of the unsteady pressure are obtained at the tip of the impingement edge. These signals are subjected to appropriate filtering, then digitized and subjected to a fast Fourier transform, which provided pressure spectra.
- By employing concepts of spectral and cross-spectral analysis of the sequence of PIV images, it was possible to obtain amplitude and phase distributions of the organized fluctuation across the shear flow.
- Three-dimensional surface elements, such as vortex generators are employed to attenuate self-excited oscillations.

2.4. Outline of Dissertation

Introduction part of this thesis introduces cavity oscillations with and without perforated plate and practical applications of perforated surfaces.

Literature survey part gives the summary of previous investigations, unresolved issues and objectives of present investigations.

Material and Method part describes experimental system (water channel system, dimensions of perforated plates, pressure measurement system) and measurement techniques.

Results and discussion parts discuss first self excited oscillations of turbulent inflow along a perforated plate. Then all the pressure measurements are illustrated along a perforated plate with various impingement length and constant free stream velocity. Attenuation of self-excited oscillations via three dimensional surface elements like vortex generators reported as a last part.

Finally conclusion and recommendations part summarize main results of the present study and gives recommendations as future studies.

3. EXPERIMENTAL SYSTEM AND TECHNIQUES

3.1. Measurement Techniques

Techniques of high image velocimetry will be employed throughout the investigations. Particle Image Velocimetry (PIV) is a Flow Measurement Technique which can be used to obtain the time dependent full field velocity distributions of single and multi-phase flows. Two-dimensional or three dimensional velocity field distributions can be obtained. The particle image velocimetry (PIV) technique provides, for the first time, a global view of the instantaneous flow field in a quantitative fashion. This allows the user to examine the presence of small flow structures and their influence, obtain vorticity fields quantitatively and, finally, obtain mean, turbulence and stresses globally. These unique capabilities provide a powerful diagnostic tool for solving problems, a unique insight into the nature of flows and the ability to improve the performance of fluid machinery and systems.

Particle Image Velocimetry (PIV) uses images of marker particles in a fluid flow to measure instantaneous velocity fields in experimental fluid mechanics. In general, the particles are illuminated by pulsed sheets of light at precise time intervals to produce images that are recorded on photographic film or on a video camera array. In practical application situations, according to the measurement requirements, the appropriate operating mode needs to be selected and specific system configurations are needed. In general, a PIV system consists of illumination, image acquisition, particle seeding, and image processing and data analysis sub-systems. Laser light is commonly used as the illumination source in PIV systems. Ideal tracer particles should be very small and follow the flow field. Different flow fields need different seeding particles. The design of the seeding particles was discussed by Schmitt et al. (1995). According to spatial resolution requirements, either photographic or CCD video cameras can be used to record the particle images. If the resolution is high enough, CCD video cameras are preferred. To resolve velocity direction ambiguity during the image acquisition process, an image shifting technique is needed (Adrian 1986b). Image interrogation techniques include auto-

correlation and cross-correlation image processing methods. PIV started as a two dimensional velocity measurement method and is being developed to a three dimensional velocity measurement method.

3.1.1. Overview of Correlation Process

Particle Image Velocimetry processing basically determines the distance that the particles moved in the time between laser pulses. The most common methods to determine this distance are particle tracking or correlation. (Özgören 2000) These are Autocorrelation, 1-Frame Cross-Correlation and 2-Frame Cross-Correlation. The differences in these correlation techniques are the image window areas for the first and second particle images. In autocorrelation, the same image window is used for both the first and second image window. In 1-frame cross-correlation, the second image window is offset from the first image window on the same frame. In 2-frame cross, the first image window is on frame 1 and the second image window is on frame 2. Each of these processing techniques has advantages for some applications.

Autocorrelation is for multiple exposure images where the particle motion and image shift together give less than ¼ of the interrogation spot image displacement. This is the classical PIV processing technique.

1-frame cross-correlation is also a multiple exposure technique. It is used when the image shift displacement is large relative to the particle motion displacement. By offsetting the second image window from the first by the mean particle image displacement, distance high-resolution measurements can be made. Otherwise, it would require prohibitively large interrogation spot sizes for autocorrelation processing. By offsetting the second image window by the mean particle image displacement, the interrogation spot size can be reduced and fewer lost pairs relative to autocorrelation will result.

2-frame cross-correlation measures the distance which particles have moved between exposures on two image frames. Each of these frames has only one pulse of light. By knowing the sequence of the first pulse images and the second pulse images, the processing signal-to-noise ratio relative to the single frame techniques is

improved. 2-frame cross-correlation can measure zero displacements and reversing flows without image shifting. 2-frame cross-correlation can be used with image capture systems with an effective frame rate high enough so that the particle images on two successive frames give particle image displacements in the measurable range.

3.2. Experimental Arrangement

Experiments performed in a large-scale water channel, using combination of surface pressure measurement and particle image velocimetry, which yields global representation of the velocity and vorticity fields. The overall experimental system and quantitative measurement techniques are described in the following.

3.2.1. Water Channel System

Experiments will be performed in a large scale water channel which located at Lehigh University, Fluid Mechanics Laboratory, U.S.A. Free-surface water channel having a test section 927 mm wide x 610 mm deep and 4928 mm length shown in Figure 3.1. The water flow speed was controlled by an Ingersoll-Rand radial flow pump. The water channel test section was constructed of transparent plexiglass with upstream and downstream PVC reservoirs. This test section is preceded by large contraction having an inlet width 1478 mm. An arrangements of honeycombs and screens is located upstream of the contraction; it minimized the free-stream turbulence.

3.2.2. Experimental System

The overall aim of this experimental system is to examine instabilities past a fully submerged perforated plate-cavity system, with the option of controlled perturbations of the cavity. This approach allows examination of self-excited instabilities with and without occurrence of simulated cavity resonance. A full boundary layer will be generated along a continuous plate.

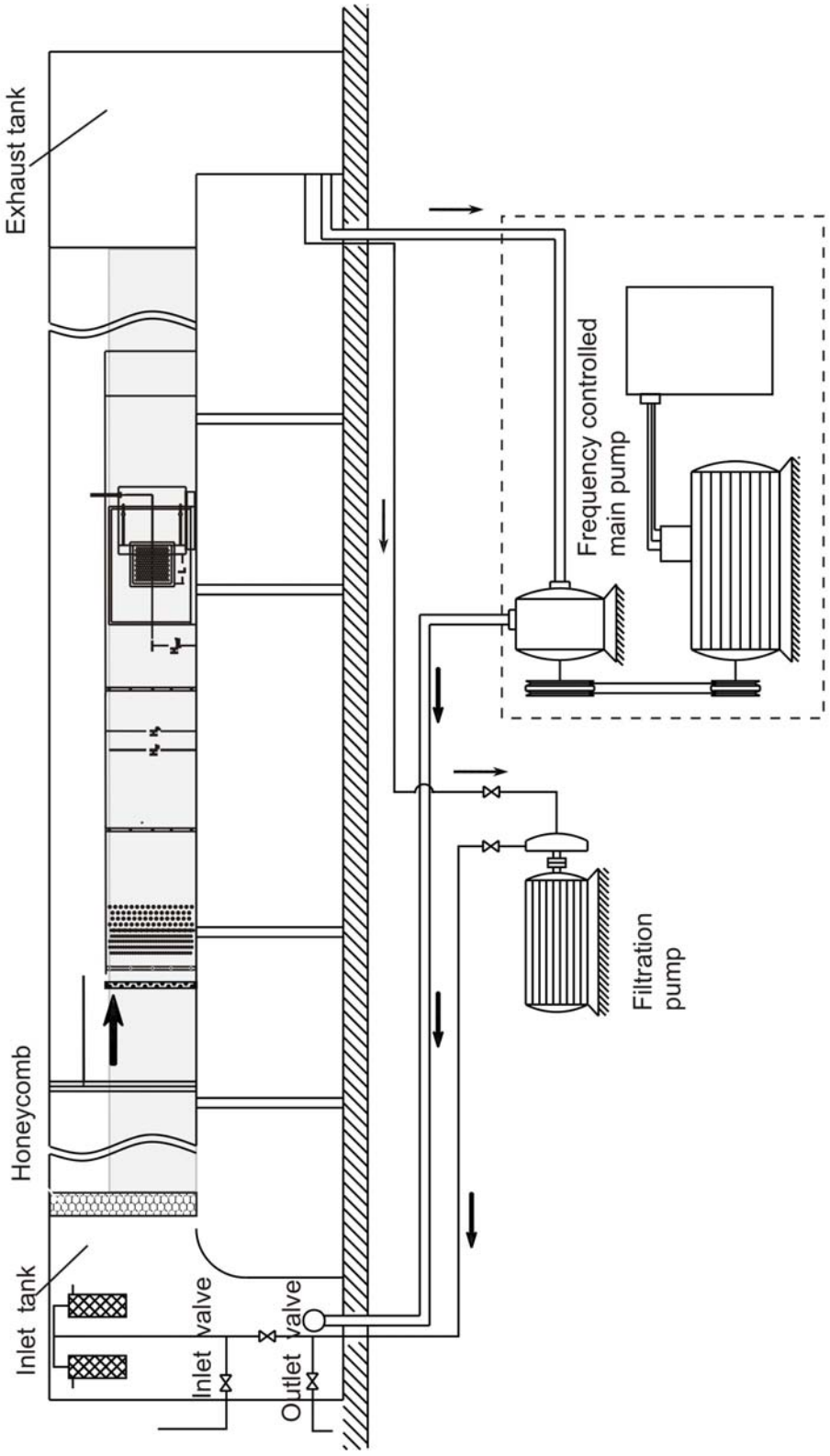

Figure 3.1 Schematic representation of water channel

At an appropriate location, a perforated plate will be mounted in a cutout, which defines the cavity that bounds the plate. Efforts will be made to optimize instability in absence of cavity perturbations, then to examine its frequency and amplitude response in relation to perturbation conditions. Furthermore this system will be designed such that imaging in orthogonal planes will be attainable, in order to basic features of the quasi-two-dimensional and three-dimensional flow structure.

The experimental system will be mounted within a large-scale water channel as shown in Figure 3.2. A system of false vertical walls, as well as a suspended horizontal plate at a suitable length with a boundary layer trips at the leading edge to ensure a fully-developed turbulent boundary layer at the leading-corner of the cavity. The overall length L of the perforated plate, which also corresponds to the length L of the bounding cavity.

Experiments were undertaken in a large-scale water channel, which had a test section 4.928 mm long, 610 mm deep and 927 mm wide. This main test section of the water channel followed a large reservoir, a flow-conditioning unit that involved a sequence of honeycomb and screens, and a contraction. The test section insert, which was placed within the main test section of the water channel, involved an additional contraction, which brought the width of the channel from its original value of 927 mm to an effective channel width of 387 mm. A long flat plate was located downstream of the contraction. The length of this plate, which extended from the exit of the contraction to the leading-edge of the perforated plate of interest in the present investigation was 1.575 mm.

The perforated plate was mounted in a vertical plate of height H_p = 457.2 mm, as defined in the schematic of Figure 3.3 The free-surface of the water in the test section was 450 mm beneath the top edge of the plate. The nominal spanwise length ℓ_a and the streamwise ℓ_b at nominal values of 197 and 183 mm respectively. The thickness of the perforated plate was maintained constant at a value t = 11 mm. In order to vary the effective length L of the perforated plate, a large-scale impingement plate could be translated along its surface, as illustrated in Figure 3.3 This impingement plate had a sharp edge beveled at an angle of 10°. Unsteady pressure measurements at the tip of the impingement plate involve placement of a

PCB pressure transducer within a brass tube arrangement along the top edge of the perforated plate. Initial calibration showed that the effective amplitude and phase distortion of the measured pressure was less than 1% of their nominal values.

The size of this cavity was substantially larger than the width and length of the perforated plate, such that the consequence of localized recirculation flow patterns was minimal. The length of the cavity in the streamwise direction was 610 mm, its height was 432 mm and its depth was 432 mm. Since purely hydrodynamic oscillations are of interest, the cavity was designed with rigid walls, in order to preclude fluid elastic effects. In addition, the characteristic frequencies generated in this study have values of acoustic wavelength roughly two orders of magnitude larger than the largest dimension of the cavity; on this basis, the effects of resonant acoustic coupling were eliminated.

In order to rapidly trip the boundary layer, a sequence of eleven boundary layer trips were placed at and near the leading edge of the plate. These trips were based on the design criteria of the Johansen & Smith (1983). Small spherical and circular cylindrical elements made up successive arrays to allow generation of a fully developed turbulent boundary layer at the inflow boundary of the perforated plate investigated herein. The freestream velocity was maintained at a value U = 240 mm/s and the momentum thickness of the turbulent boundary layer was θ =7.5 mm. [The Reynolds number based on θ was Re_θ = 1800.] The form of this inflow boundary layer agreed very well with that defined by Lin & Rockwell (2001) in a related investigation involving fully-developed turbulent flow.

The flow was initially accelerated in a contraction, then subjected to a series of trips, in order to generate the onset of a turbulent boundary layer, which evolves in the downstream direction. In addition, the location of the trip section for the boundary layer, located along the upper surface of the plate, is illustrated in both and side views of Figure 3.2. Details of the trip section are shown in Figure 3.4, taken from Johansen and Smith (1983). Small (3.36mm) and large (3.86mm) diameter Plexiglas hemispheres were arranged in the pattern illustrated in Figure 3.4.

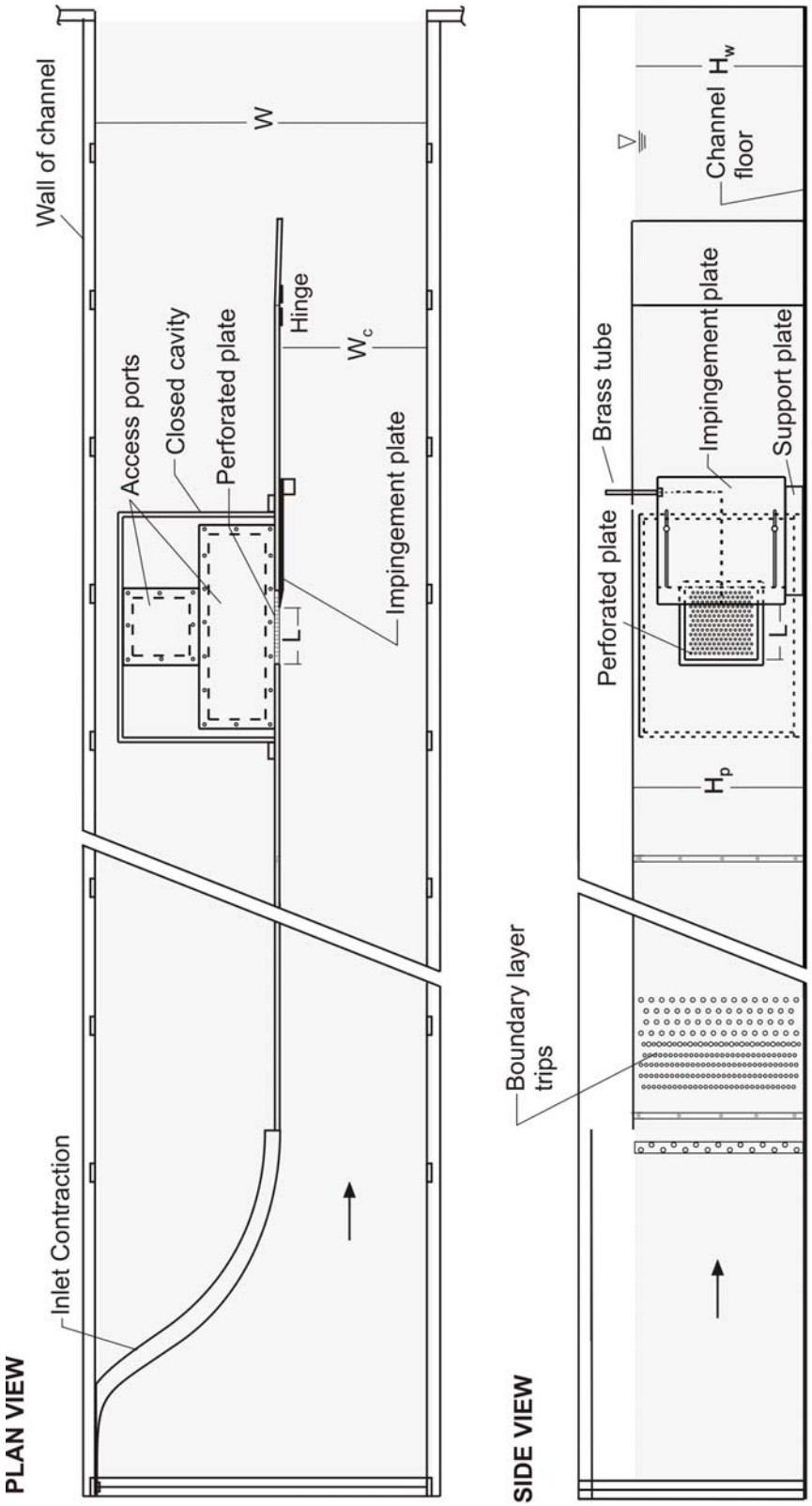

Figure 3.2: Overview of perforated plate-cavity system in large-scale water channel.

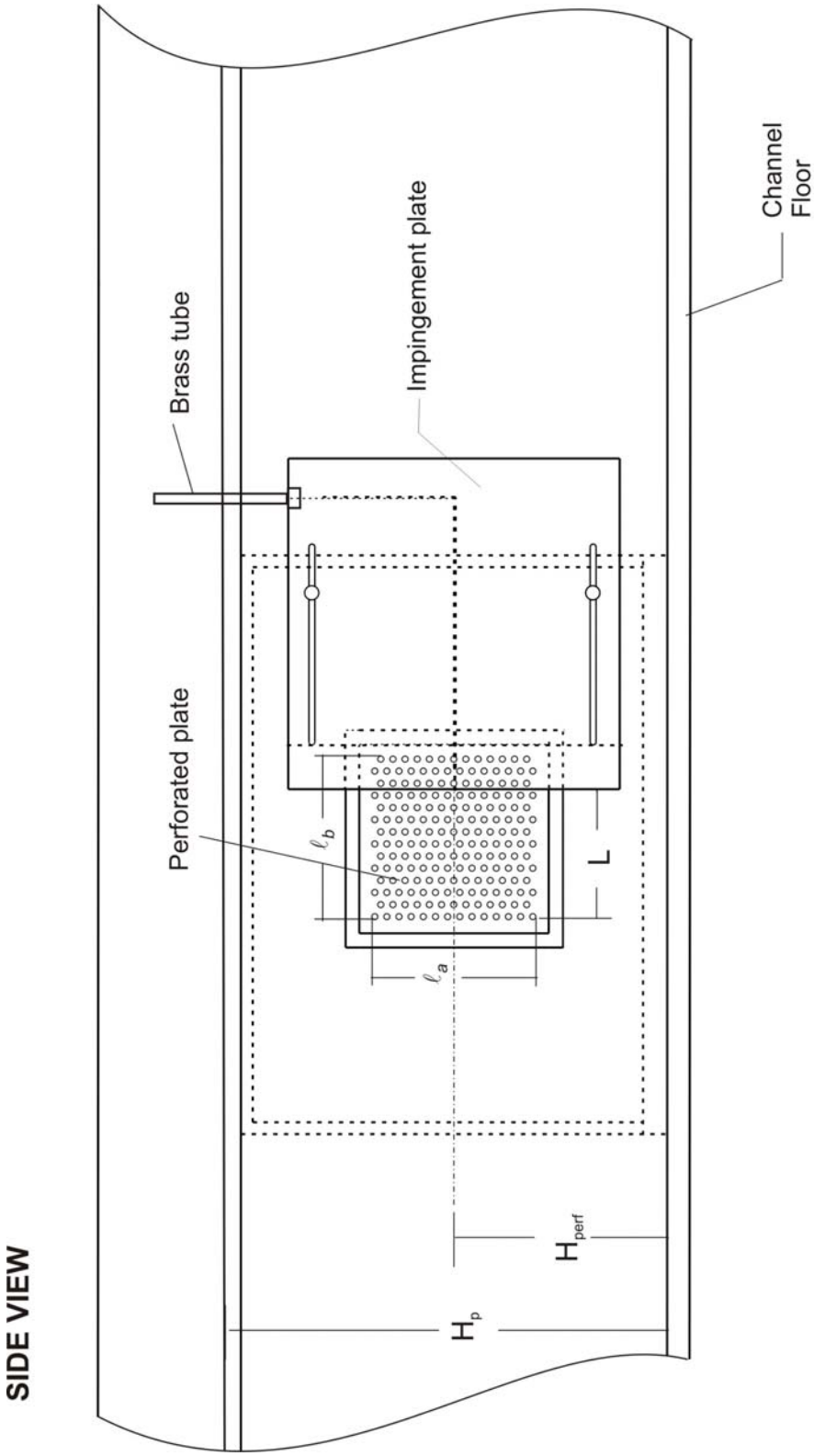

Figure 3.3: View of perforated plate and impingement plate.

The spatially periodic arrangement of these hemispheres extended across the entire span of the plate. In the study of Johansen and Smith (1983), this configuration was found to generate a well-posed turbulent boundary layer for the same value of velocity and effective plate length. Immediately upstream of the perforated plate, the boundary layer momentum and displacement thicknesses are $\theta/\delta = 0.1136$ and $\delta^*/\delta = 0.169$, which are characteristic of a fully turbulent boundary layer.

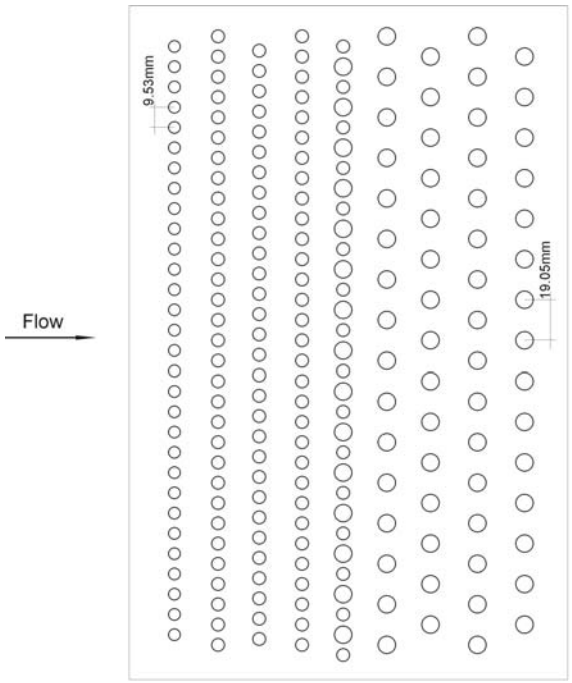

Figure 3.4. Representation of three-dimensional trip section for promoting rapid transition of boundary layer Location of trip section is indicated in Figure 3.2. Circles indicate diameters of hemispheres at specified locations near the leading edge of the plate. (From Johansen and Smith 1983)

A zoomed-in view of the perforated plate is shown in Figure 3.5 and 3.6. Four different plates were employed, with hole diameters of D = 6.4 mm, 12.7mm, 19.1mm and 25.4mm. The plate was maintained constant thickness at t =11mm for all experiments. The spanwise and longitudinal spacings Δ_a and Δ_b had values such that the open area ratio of all hole patterns was the same. This open area ratio was 69%; it is defined as the total open area due to the sum of the areas of the holes, normalized by the total area of the plate.

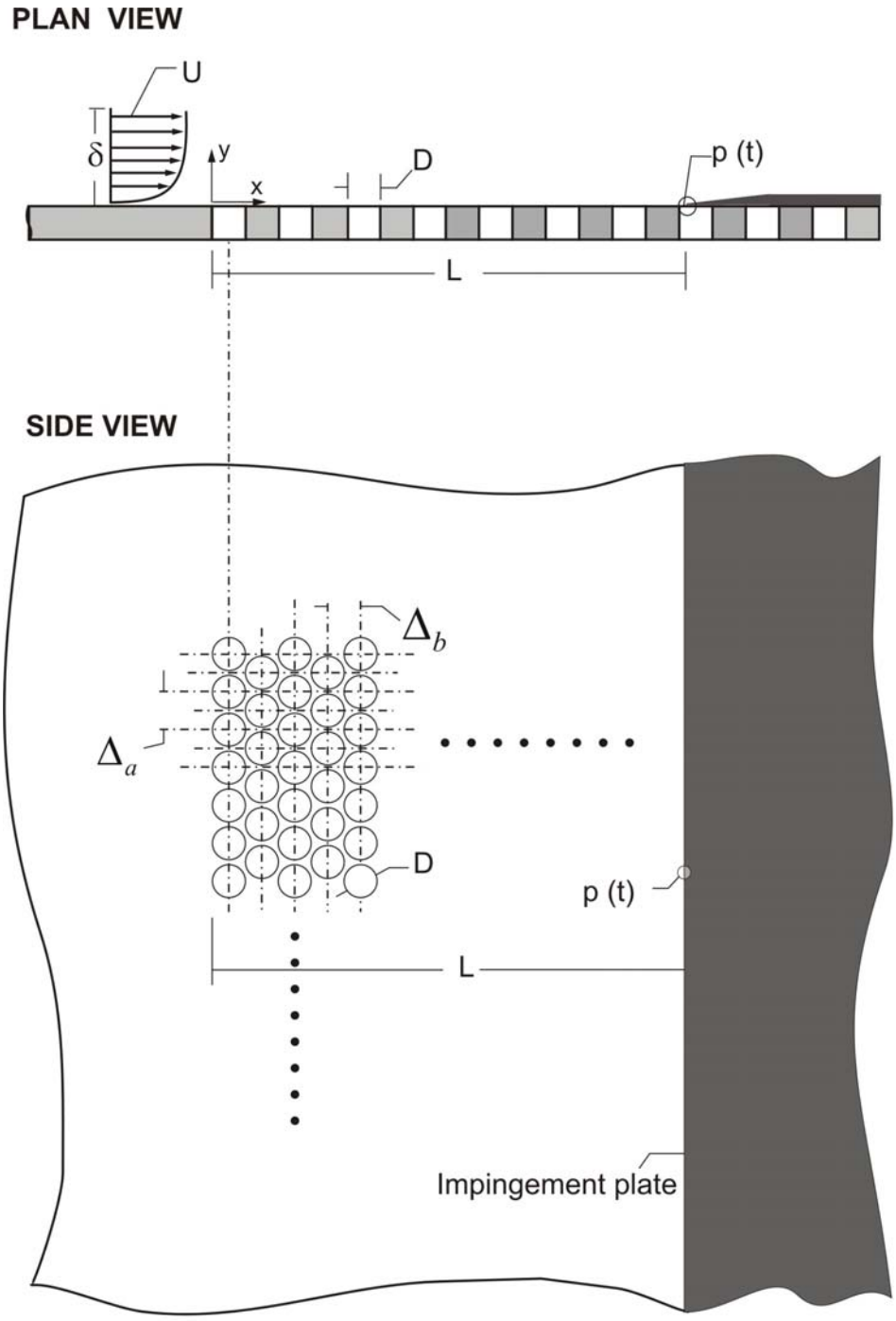

Figure 3.5. Zoom-in view of perforated plate system

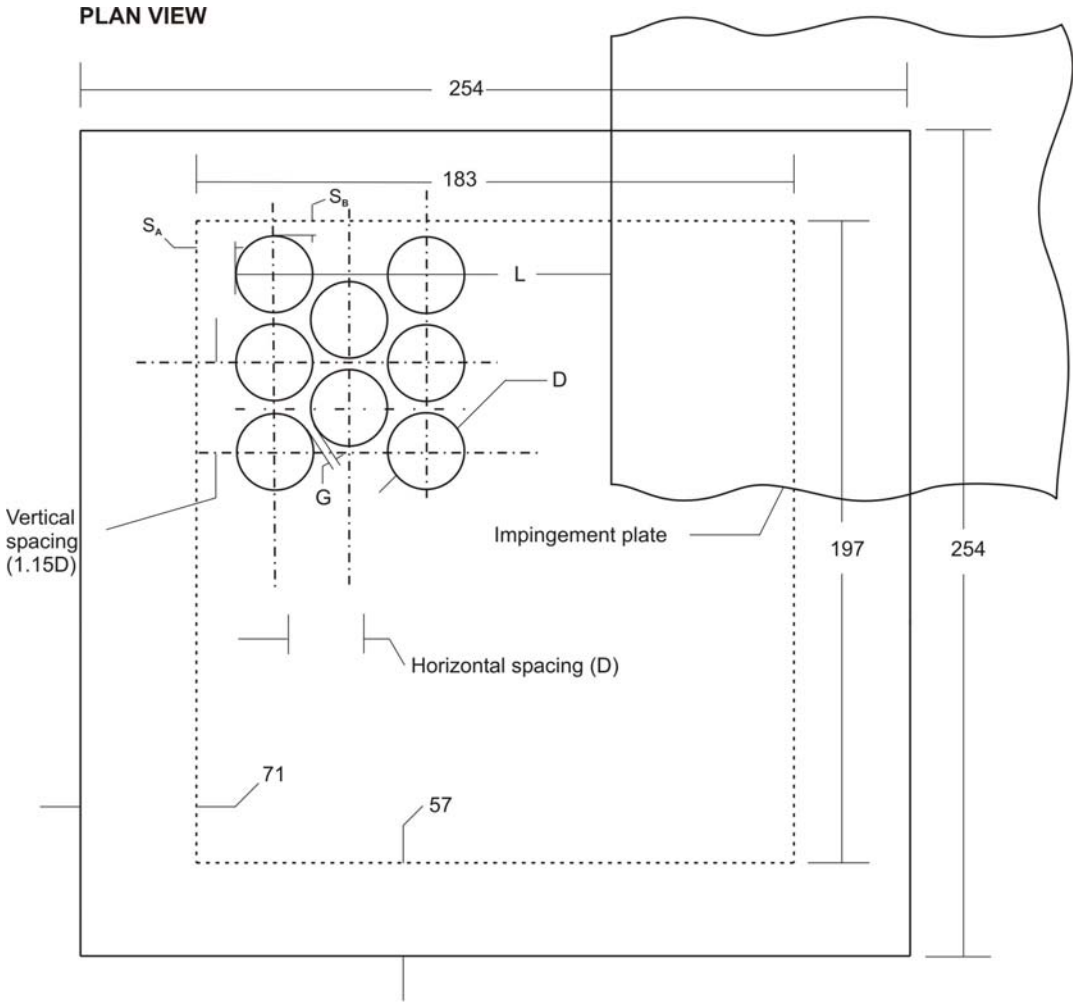

Diameter (D)	Horizontal spacing	Vertical spacing	Gap thickness (G)	Plate Thickness (t)
25.4	25.4	29.2	4	11
19.1	19.1	22	3	11
12.7	12.7	14.6	2	11
6.4	6.4	7.3	1	11

Figure 3.6. Perforated plate. (All dimensions are in mm.)

3.3. Three-Dimensional Surface Elements

In absence of the three-dimensional surface elements, a well-defined front of the unstable oscillation propagates along the surface of the plate. In presence of an appropriate surface element, the front is no longer detectable, and instantaneous and averaged defects of the streamwise velocity and surface-normal vorticity exist along the span of the plate. The magnitudes and spanwise wavelengths of these defects are directly related to the extent of attenuation of the oscillation. Since the magnitudes of these defects decay significantly with distance along the plate, the most effective attenuation typically occurs for plate lengths less than or equal to a critical length.

An appropriate measure of the degree of attenuation is a reduction in the magnitude of the coherent component of the fluctuating pressure. For all cases, even in presence of effective attenuation, a low magnitude spectral peak at the frequency of the inherent oscillation is still discernible; it may be either sharp or broadband, and is indicative of the robust nature of the self-sustained oscillation.

A schematic of a representative three-dimensional surface element, which can be generally referred to as a row of vortex generators, is given in Figure 3.7. The trailing-edge of this unit was located a distance of ℓ = 89 mm upstream of the first row of perforations in the plate, as designated in the schematic of Figure 3.7. Five different configurations of the three-dimensional triangular surface elements were employed. They are designated as elements *A* through *E* in Figure 3.8. For each type of element, the absolute values of element height and wavelength are given in dimensions of mm on each schematic. Furthermore, the table at the inset of Figure 3.8 provides dimensionless values of the height h/θ and wavelength Λ/θ. As indicated, the values of dimensionless height range from h/θ = 0.3 to 1.4, while the values of spanwise wavelength are essentially from Λ/θ = 2.13 to 12.80. As will be demonstrated, small values of h/θ are relatively ineffective.

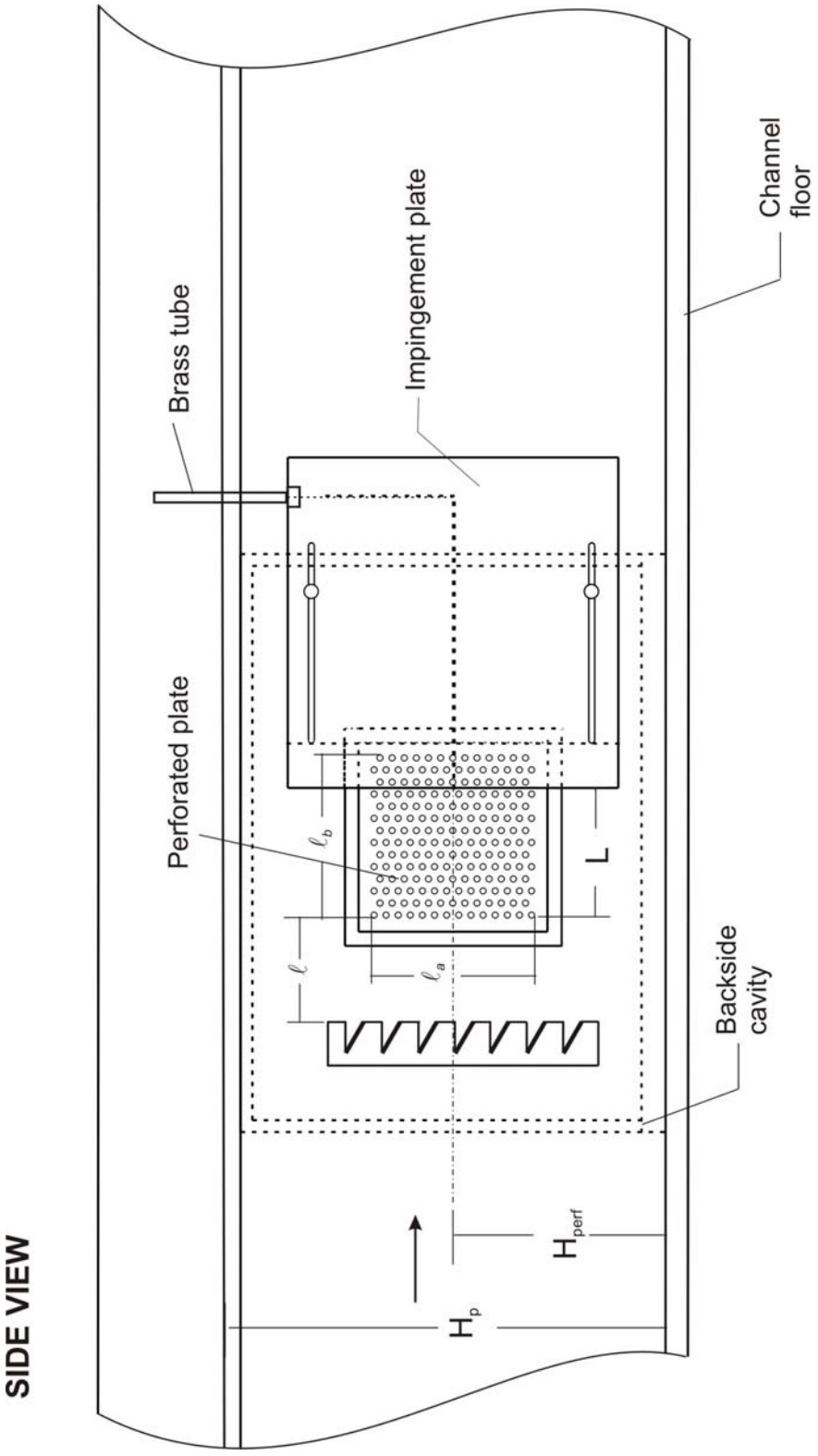

Figure 3.7: View of perforated plate, impingement plate and vortex generator.

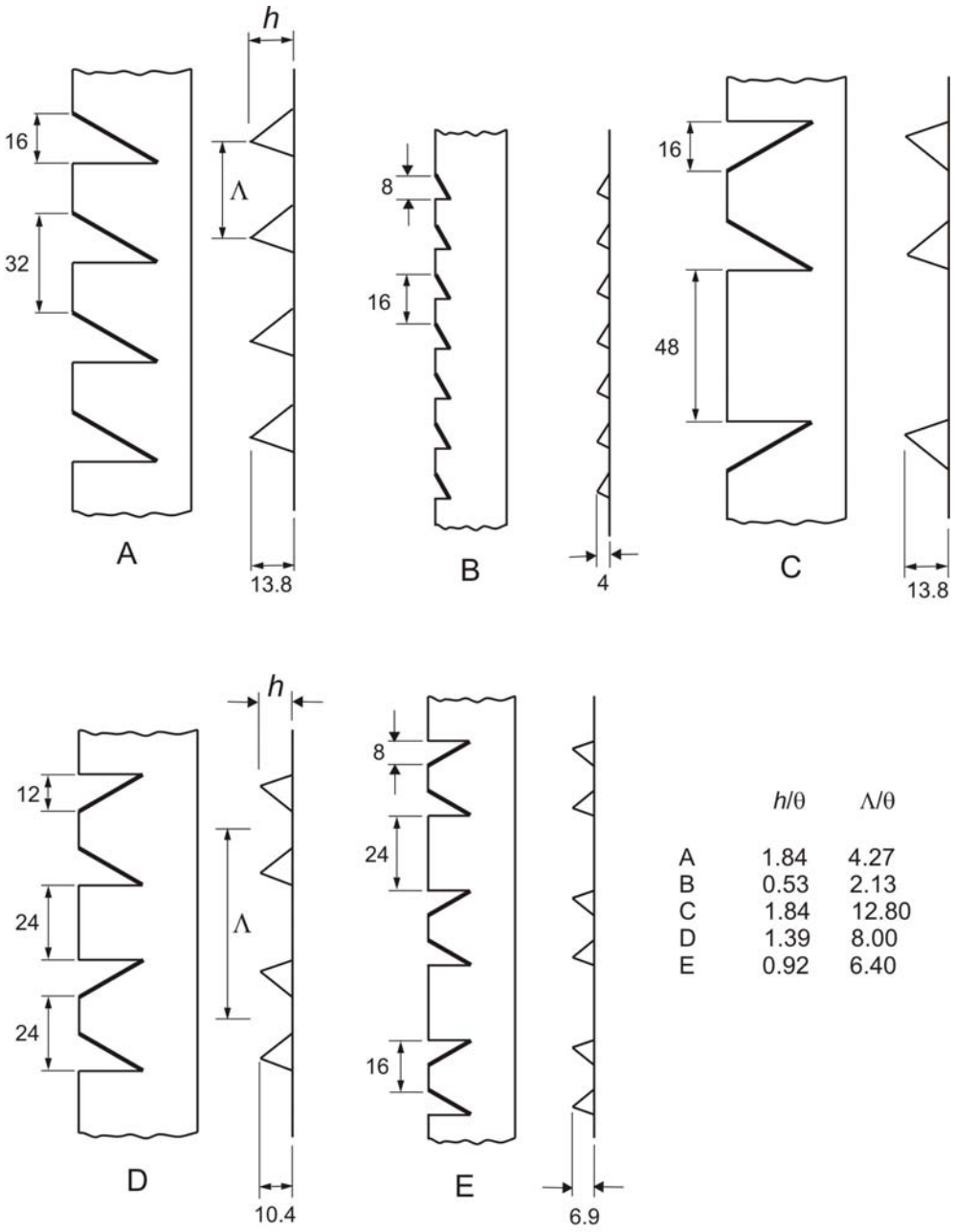

Figure 3.8. Plan and side views and dimensions of vortex generators

3.4. Image Acquisition

Quantitative visualization of the flow patterns was attained using a method of high-image-density particle image velocimetry. Illumination was in the form of a 1mm thick laser sheet which was generated from two Nd:Yag pulsed lasers fitted with a cylindrical–spherical lens system. Each laser of the dual system had a power ratingof 90 mJ. Two orientations of this sheet were employed. For the horizontal orientation, the laser sheet intersected the horizontal center-line of the plate, as indicated in Figure 3.9 This placement of the laser allowed quasi-two-dimensional visualization of the flow structure. Alternately, a horizontal orientation of the laser sheet was used, as indicated in Figure 3.10 and 3.11. In this case, the sheet was placed close to the surface of the perforated plate, i.e., the distance between the centerline of the laser sheet and the surface of the plate was 1 mm. Using this approach, it is possible to determine the instantaneous spanwise structure of the flow pattern along the perforated plate.

A time sequence of 200 images was acquired at a frequency of fifteen frames per second. This set of instantaneous images could be time-averaged or, by using a selected, coherent event of the instability adjacent to the plate, a phase-average of the flow pattern was acquired. Post-processing involved a combination of instantaneous time-averaged and phase-averaged representations of velocity, vorticity and Reynolds stress. Furthermore, by employing concepts of spectral and cross-spectral analysis of the sequence of PIV images, it was possible to obtain amplitude and phase distributions of the organized fluctuation across the shear flow.

The PIV images were recorded in the cinema mode, at an effective framing rate of 15 frames per second. Since the maximum frequency of interest in this investigation corresponded to a coherent oscillation at $f_0 \leq 1\,Hz$, it was possible to perform spectral analysis. At a specified location, xy in the flow field, it was possible to construct the time variation of the desired velocity fluctuation by considering a total of 200 PIV images, which represents 200 sample points. This single record, without averaging, was employed to determine the spectrum. A Hanning window was employed during the spectral analysis.

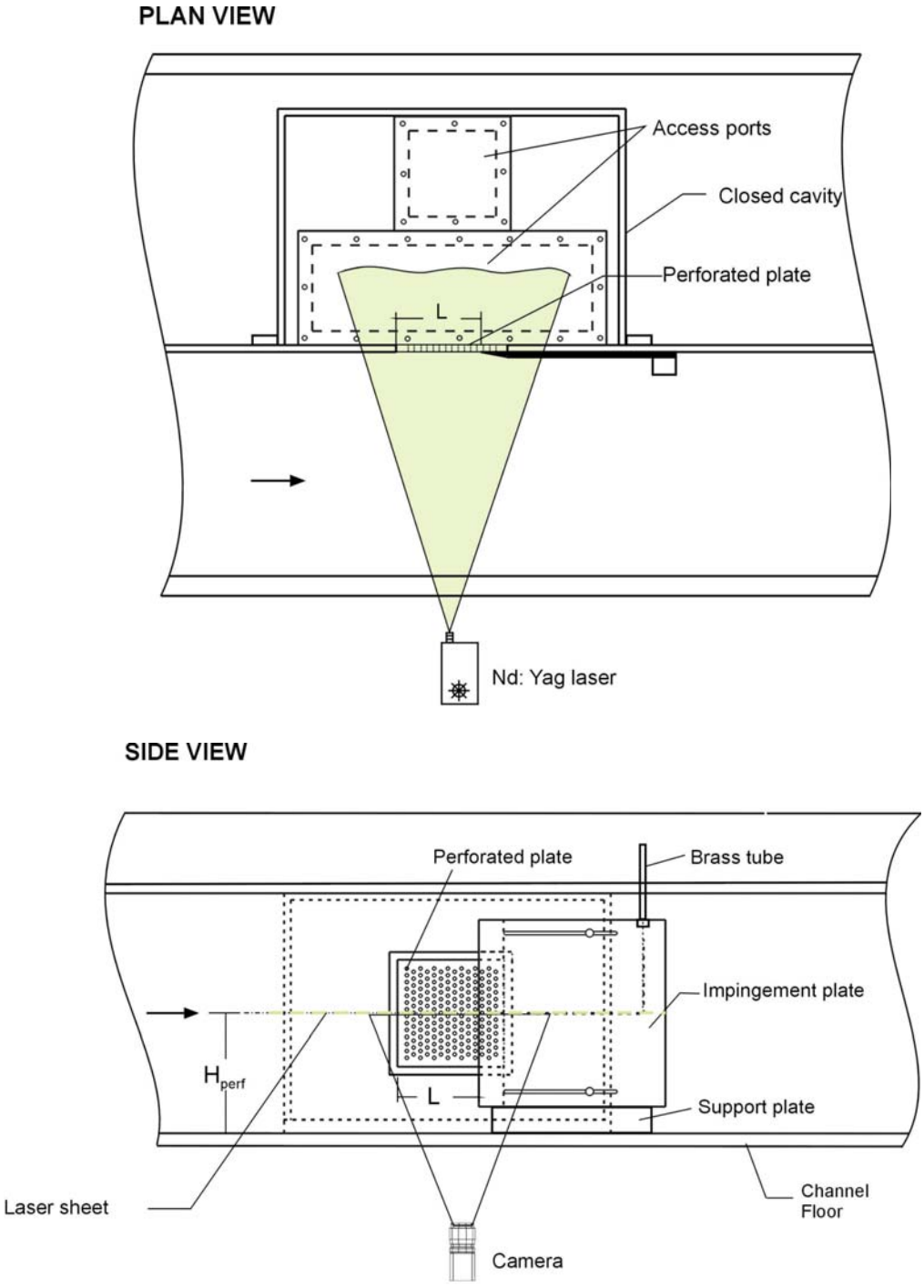

Figure 3.9. Plan and side views of test-section showing location and horizontal orientation of laser sheet and field of view of camera.

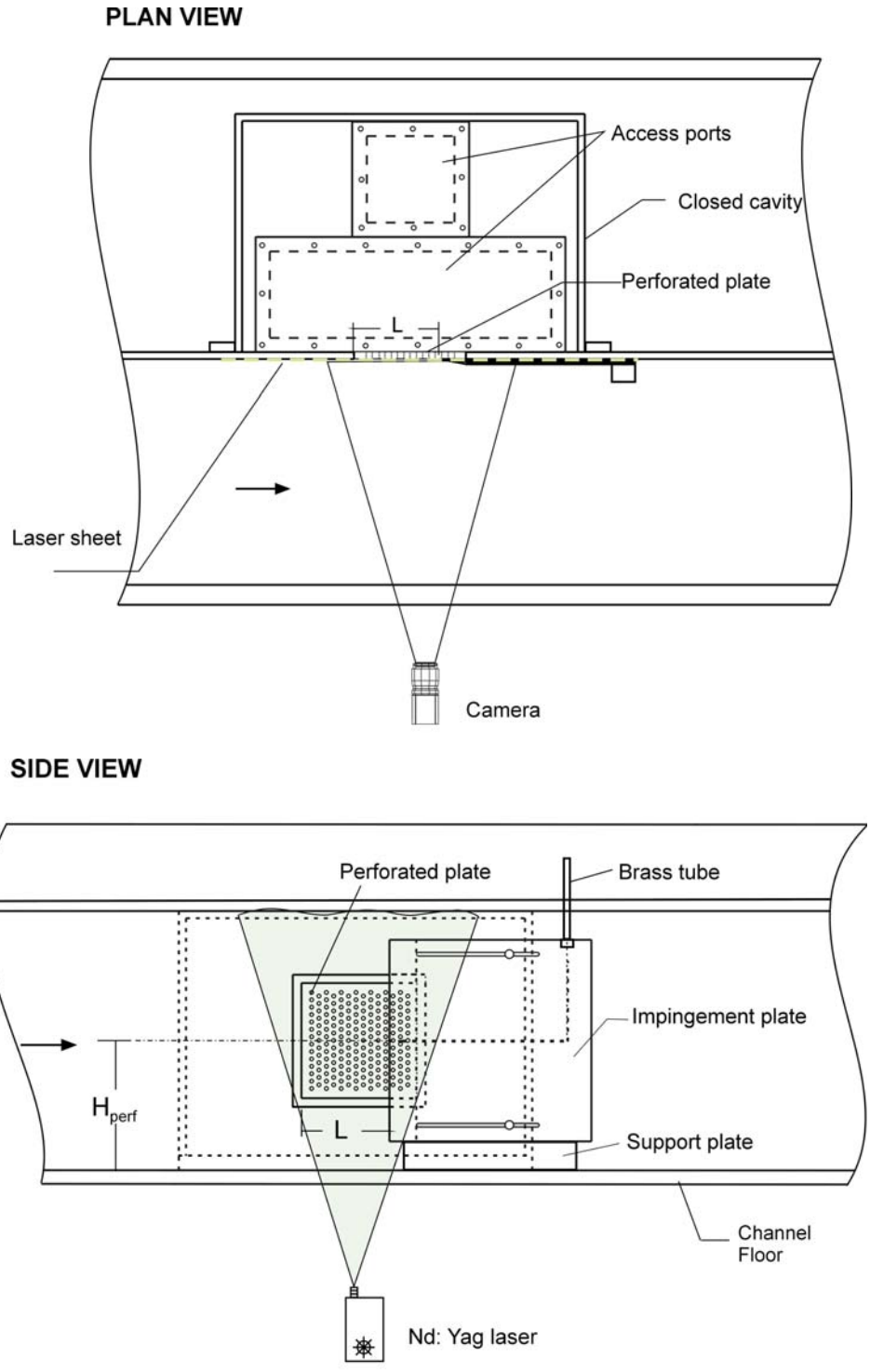

Figure 3.10. Views of perforated plate test-section showing orientation and location of laser, generated laser sheet, camera and field of view for laser sheet close to surface of perforated plate.

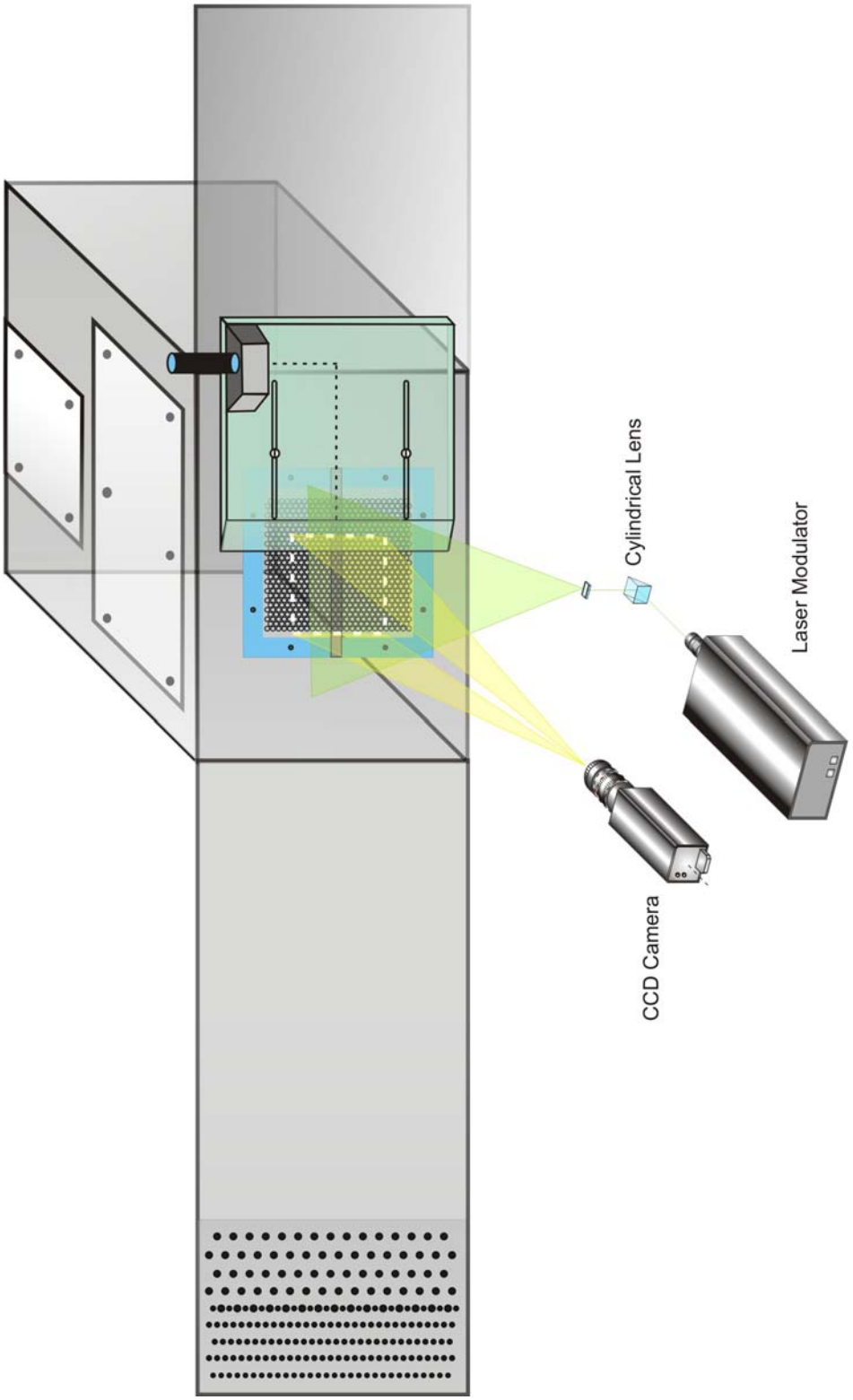

Figure 3.11: 3D view of cavity and laser orientation

The flow is seeded with 12 micron, metallic coated hollow plastic spheres, which were essentially neutrally buoyant. The silvered coated hollow particles were mixed in a one liter container, then poured in to the water channel. Then, the water channel was run at maximum speed for a period of several minutes, in order to ensure that particles were uniformly dispersed throughout the water. TSI PIVCAM 10-30 CCD digital camera, having a resolution of 1024 × 1024 pixels, allowed acquisition of the patterns of particle images. The camera was equipped with NIKON AF Micro Nikkon 55 mm focal–length lens. The CCD camera and lasers were connected to a PC via a TSI Laser pulse synchronizer control system which could control the timing of data acquisition. Patterns of particle images were acquired at a rate of 15 frames pairs per second. A Hart correlation technique was employed to determine the velocity fields. The basic principle of Hart Correlation is that each interrogation spot image is first compressed based on a threshold defined by the user as compression ratio. The intensity information on the compressed images is then put into an encoded form and correlation function is performed on the encoded information. The Hart Correlation is also applied in a progressive fashion to allow the reduction of interrogation spot size for high spatial resolution. A double correlation technique is also used to increase signal -to-noise ratio for the correlation function so that the correct velocity measurements can be made more robustly. The Hart Correlation allows interrogation spot size to be as small as 4 pixels to be analyzed so that vector field with very high spatial resolution can be obtained.

The pattern of velocity vectors was calculated by performing a cross-correlation of the patterns of particle images in each frame pair. During this interrogation, windows of 32 × 32 pixels and 16 × 16 pixels were employed. In order to ensure that the criterion for high-image-density was satisfied, the number of particle images within the interrogation window was, at minimum, 15 to 20. Furthermore, during the interrogation process, these windows were overlapped by 50% in order to satisfy the Nyquist criterion. The field of view for the velocity vectors is indicated in conjunction with each figure. The total number of velocity vectors attained or acquired over the field of view of each original image ranged from 9136 to 9364.

The images were acquired using TSI's INSIGHT 3.0 software. The PIV images by the CCD camera were digitized by an image processing board, then transferred to a PC for image processing and display on a PC monitor.

Post Processing refers to the analysis of the velocity vector field after the vectors have been extracted from the PIV image. Post processing consists of two basic functions—vector editing, and computing flow properties. Vector editing is necessary because some wrong peaks may be chosen as the velocity peak. In vector fields with 1,000 points, ninety-nine percent correct vectors still gives 10 wrong vectors. During the image processing the signal-to-noise ratio at each spot must pass the threshold values to be considered a valid peak. Usually these thresholds are set to filter out most of the bad points, but if the thresholds are too high to filter out all the bad points, many good points are also eliminated.

In post processing, the vectors are compared against the neighboring vectors. Vectors that vary by more than the validation tolerance from the neighborhood average are removed. This neighborhood check enforces continuity on the flow. Places that are left empty can be filled in by interpolating the neighboring vectors to get the best estimate of the velocity at that point. After the vector has been validated and the missing points filled in, the properties of the flow can be computed. Measuring the flow properties like vorticity from the accurate vector field data is one the key reasons for performing PIV measurements. The post-processing module computes vorticity, Reynolds stresses, and the velocity magnitude.

CLEANVEC PIV vector validation software, which is developed by Steven M. Soloff and Prof. Carl D. Meinhart is used for removing bad vectors. After the removing bad vectors, the Fortran program NFILVB (Lin 1994) interpolated between the vectors and fill the blank locations using interpolation. The velocity field was smoothed using a Gaussian filter having an exponent p = 1.3. These interpolation and filtering techniques are well known and described in detail by Landreth and Adrian. (1989). The sampled-averaged velocity field was obtained using in-house program NWENSAV2 (Lin, 1996)

3.5. Pressure Measurement

Measurements of the unsteady pressure were obtained at the tip of the impingement edge. These signals were subjected to appropriate filtering, then digitized and subjected to a fast Fourier transform, which provided pressure spectra.

The time history of the pressure fluctuations, along with averaged spectra, will be monitored at one or more locations with in the cavity for selected phases. Such pressure measurements will be most insightful for the case where perturbations are not applied to the cavity system. Appropriate spectral analysis can provide insight into degree of coherence of the inherent fluctuation associated with the long wavelength instability. Alternately, when perturbations are applied, it is anticipated that the pressure field will be dominated by a frequency component of the applied perturbation. In this case, it will be desirable to employ the pressure signal as a phase reference for the image acquisition.

Unsteady pressure measurements at the tip of the impingement plate involved placement of a high sensitivity pressure transducer within a brass tube arrangement along the top edge of the perforated plate. Initial calibrations showed that the effective amplitude and phase distortion of the measured pressure was less than 1% of their nominal values. Pressure signals were acquired using a PCB transducer, model number 106B50. This pressure transducer had a sensitivity of 500 mv/psi. Other specifications of transducer are given in Appendix E. Spectra of the fluctuating pressure were acquired through sampling the pressure signal at a nominal frequency of $\Delta f = 20$ Hz, which provides a Nyquist frequency $1/2\ \Delta f = 10$ Hz.

Figure 3.12 gives the view of the pressure transducer box, showing the plan and side views of the transducer block. The pressure tap was connected to the pressure transducer by means of 1.6 mm diameter pressure transmission line and actual face of the pressure transducer allowed the instantaneous pressure to be sensed by the active face of the pressure transducer, which had an overall diameter of 18 mm and a sensing face with a diameter of 16 mm.

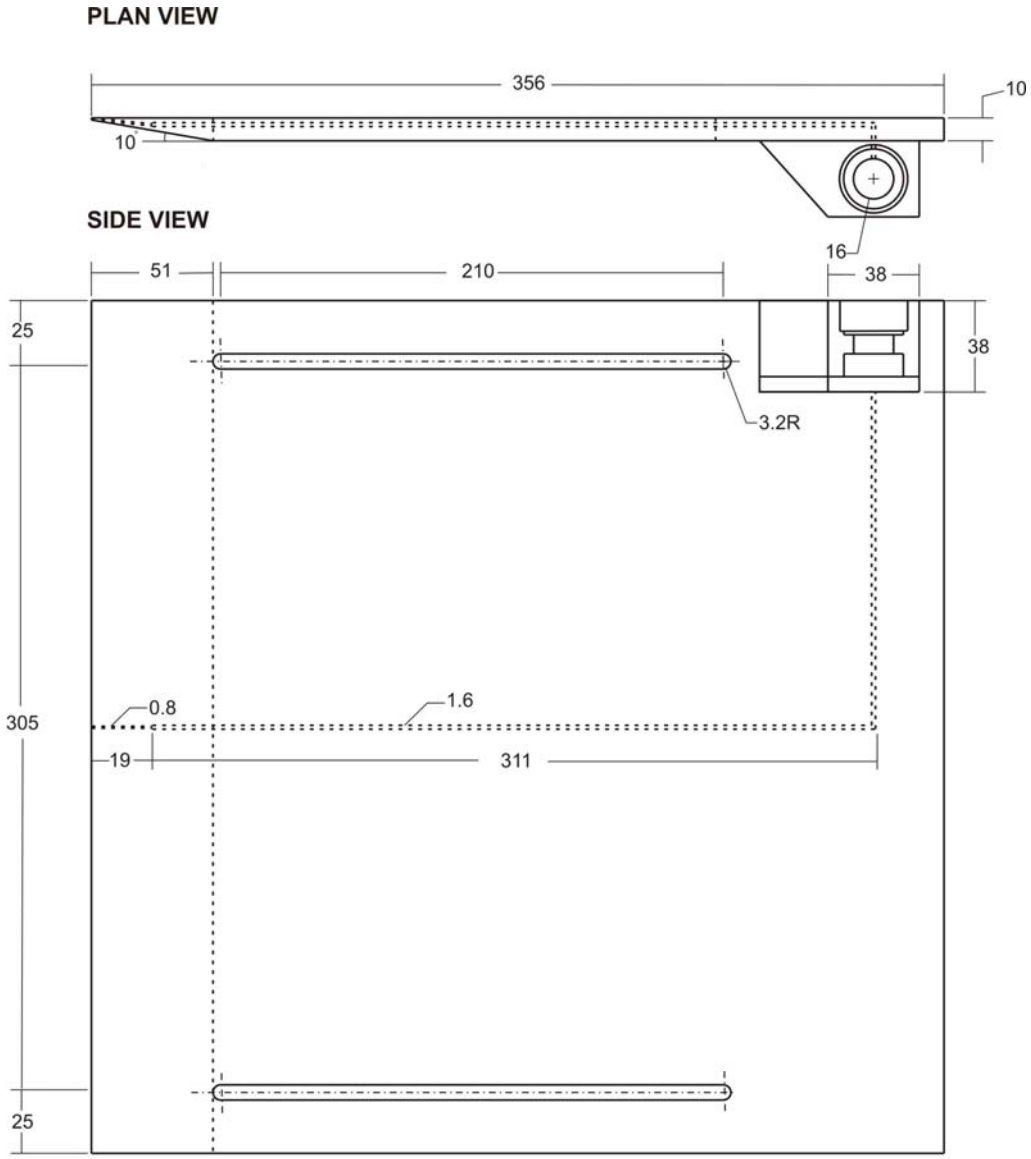

Figure 3.12. Close-up of impingement plate showing pressure tap, transmission line, and transducer housing system. (All dimensions are in mm.)

During the pressure analysis experiments pressure signals were subjected to analog filtering and electronic amplifiers. The sampling time was $\Delta t = 0.05$ sec, in order to adequately resolve all the dominant frequencies. Each signal was then transmitted to the A/D board of the host microcomputer, stored in digital form, allowing reconstruction of the time traces, as well as computation of the spectral peaks using an FFT technique. Figure 3.13 illustrates pressure signal lines from transducer to host microcomputer.

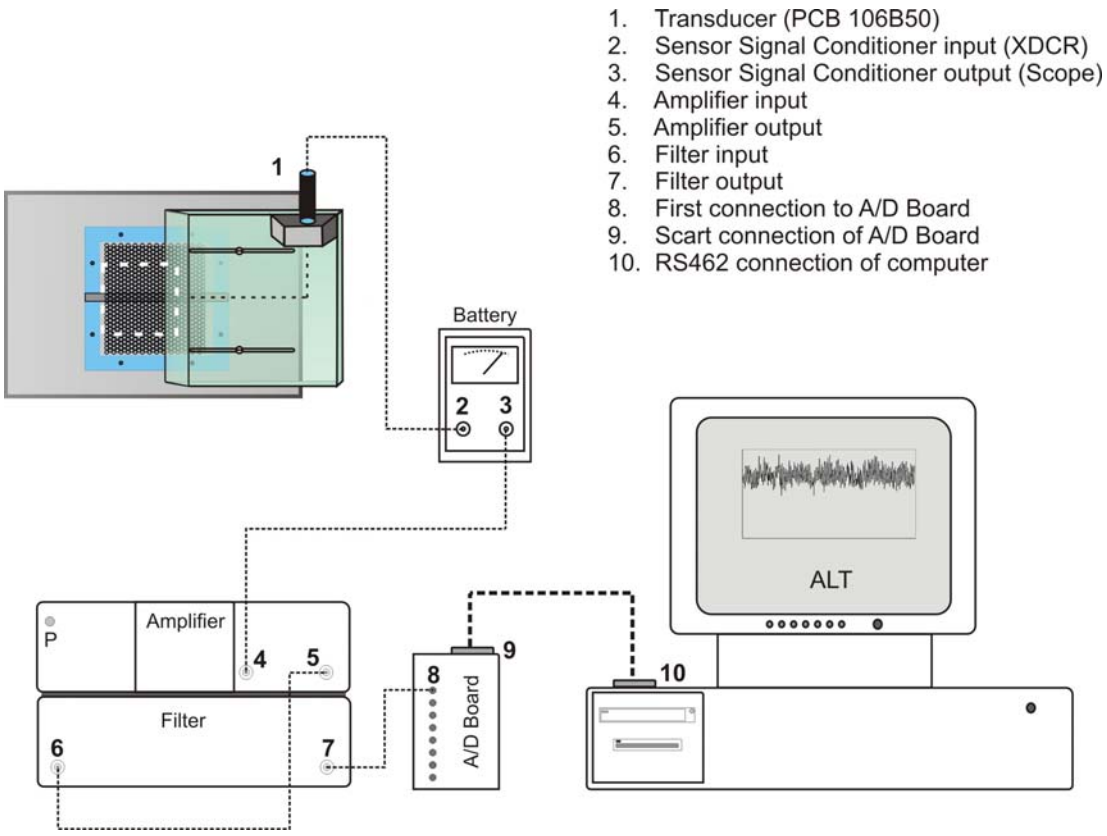

Figure 3.13. Schematic representation of pressure signals transfer connections

4. RESULTS AND DISCUSSIONS

4.1. Self-Excited Oscillations of Turbulent Inflow Along a Perforated Plate

The grazing flow of a fully turbulent boundary layer along a perforated plate, which is bounded by a closed cavity on its backside, can give rise to highly coherent, self-sustained oscillations of the shear flow, even in absence of acoustic resonant or fluid elastic effects. These oscillations are characterized in terms of unsteady pressure fluctuations and quantitative images of the instantaneous and averaged flow structure using a technique of high-image-density particle image velocimetry. This purely hydrodynamic instability, which rapidly emerges above the turbulent background, has a wavelength that is much longer than the hole diameter of the perforated plate. Variations of the effective length L of the perforated plate show nearly invariant values of dimensionless frequency fL/U; in which f is the predominant frequency of oscillation and U is the freestream velocity. In fact, this relationship holds even when the diameter of the hole pattern is altered. Variation of the hole diameter D does, however, strongly influence the amplitude and degree of organization of the self-sustained oscillation. It is demonstrated that, as the hole diameter becomes larger relative to the inflow boundary layer thickness, the amplitude of the predominant spectral peak is substantially attenuated and, in a limiting case, undetectable. These features are interpreted in conjunction with instantaneous and averaged patterns of the flow structure, which include distributions of both Reynolds stress and amplitudes of spectral peaks. This type of instability is distinctively different from the classical instability associated with ‘‘singing’’ of perforated plates employed in attenuation liners in engineering systems, where the genesis of the instability is local vortex shedding within each hole of the perforation, in contrast to the long wavelength instability that is addressed herein.

These oscillations can be scaled according to $f\theta/U$, which represents the dimensionless frequency of the shear layer oscillation in terms of the inflow momentum thickness θ and the freestream velocity U. Furthermore, the scaling parameter fL/U provides a basis for characterizing these oscillations, and accounts

for the effect of the finite lengthscale L. In the event that the inflow boundary layer is fully turbulent, as opposed to laminar, it is difficult to observe organized structure of these oscillations, in absence of any acoustic or resonance effects, which are absent in the case of incompressible low speed water flow past a cavity.

4.1.1. Averaged Reynolds Stress of Shear Flow Past a Perforated Plate

Figure 4.1.1 compares patterns of time-averaged Reynolds stress $\langle u'v' \rangle / U^2$ for two extreme values of hole size of the perforated plate: $D/\theta = 0.85$ and 3.38. The field of view of these patterns is indicated by the dashed frame in the schematic. The coordinate system $(x'; y')$ is measured from the leading-corner of this field of view, while the system $(x; y)$ is from the leading-edge of the perforated plate. For the case of the smallest hole $D/\theta = 0.85$; represented by the top set of contours, high levels occur in the region close to the plate perforation. In fact, the extrema of $\langle u'v' \rangle / U^2$ occur within a layer approximately 0.5y from the surface of the perforated plate. Furthermore, the contours of $\langle u'v' \rangle / U^2$ near the impingement edge are spatially periodic in the region adjacent to the plate. Their streamwise wavelength is of the order of the hole diameter.

On the other hand, for the pattern with relatively large diameter holes $D/\theta = 3.38$; shown in the bottom set of contours, highly concentrated contours, with relatively high peak values, do not occur in the region immediately adjacent to the surface of the plate. Rather, in the region immediately upstream of the plate extending from $x'/\theta = 5.0$ to 10.5, the contours are displaced significantly away from the surface of the plate. The peak value $\langle u'v' \rangle_{max} / U^2$ is -2.0×10^{-3}, compared to the substantially higher value of -5.6×10^{-3} for the aforementioned case of the small diameter hole pattern shown in the top image.

A common feature of both patterns of Reynolds stress shown in the two images of Figure 4.1.1 is that the concentrated layer of $\langle u'v' \rangle / U^2$ is confined to a region approximately $y'/\theta = 1.5$. These highly concentrated layers are in contrast to the rather broadly distributed, but well-defined regions of $\langle u'v' \rangle / U^2$, extending

approximately over the range y'/θ from 2 to 5. This region corresponds to the highest amplitudes of the broadband Reynolds stress in the naturally occurring turbulent boundary layer. In fact, the elevation of this layer and its peak values of $<u'v'>/U^2$ are in general accord with those of a fully developed turbulent boundary layer generated in a similar type of test-section by Lin &Rockwell (2001).

The relatively large amplitude and the highly ordered form of the pattern of Reynolds stress contours, which occur immediately adjacent to the perforated plate for the smaller hole pattern (see top image of Figure 4.1.1), suggest occurrence of an organized oscillation when the diameter of the hole is sufficiently small. In the next section, the degree of organization of the oscillation is addressed for this hole diameter, as well as for larger hole diameters. Spectral analyses of velocity and pressure signals serve as a basis for comparison.

4.1.2. Spectra of Velocity and Pressure: Effect of Hole Diameter

Figure 4.2 shows spectra of pressure fluctuations $S_p(f)$; measured at the tip of the impingement edge, for various hole diameters. These pressure spectra are compared with spectra $S_u(f)$ of the longitudinal velocity fluctuation component $\tilde{u}(t)$ measured across the shear layer, at a streamwise location x = 0.8L.

Consider, first of all, the peak amplitude of the pressure spectra for increasing values of hole diameter D/θ; as represented in the bottom row of plots of Figure 4.1.2. As D/θ increases from 0.85 to 2.54, the peak amplitude decreases substantially and, at the largest hole diameter $D/\theta = 3.38$, an organized component is no longer detectable. This same trend is, in fact, evident in the peak amplitudes of the velocity spectra S_u shown in the top of Figure 4.1.2. Consider, for example, the bottom row of spectra Su; corresponding to an elevation $y/\theta = 0.22$ above the surface of the perforated plate. For increasing values of hole diameter $D/\theta = 0.85$ to 2.54, the amplitude decreases substantially, as observed for the aforementioned pressure spectra. At the largest hole diameter $D/\theta = 3.38$, a distinct peak is no longer detectable. Furthermore, for a given value of D/θ, the peak amplitude of the organized component, which is indicated by the vertical dashed-line in each

spectrum, and connected from one spectrum to the next by an inclined dashed-line, shows a decrease with increasing elevation y/θ from the surface of the perforated plate. It is, therefore, apparent that for the cases where a highly organized oscillation component does occur in the turbulent shear layer past the perforated plate, it persists for a value of the order of 1 momentum thickness θ, i.e., y′/θ ≅1; though it decreases in amplitude. This observation is consistent with the highly concentrated layer of Reynolds stress $<u'v'>/U^2$ shown for the smallest hole pattern at the top of Figure 4.1.1

Contours of constant amplitude of the spectral peak $|S_u(f_0)|$ of the longitudinal velocity fluctuation $\tilde{u}$, as well as the spectral peak $|S_v(f_0)|$ of the transverse $\tilde{v}$ fluctuation are given in Figure 4.1.4. These patterns correspond to the smallest diameter hole D/θ = 0.85. The streamwise location of these patterns corresponds to the region immediately upstream of, and including, the impingement edge. The amplitude of the spectral peak $|S_u(f_0)|$ attains peak values in the region immediately adjacent to the surface of the perforated plate, but contours of relatively high level extend well above the surface of the plate, at a streamwise location immediately upstream of the tip of the impingement edge.

Corresponding patterns of the distribution of the peak amplitude of the spectral component $|S_v(f_0)|$ are shown at the bottom of Figure 4.1.4. This contour distribution of $|S_v(f_0)|$ is a complement to the pattern for the longitudinal component shown at the top of Figure 4.1.4. It shows a highly ordered form, and the region very near the surface of the plate involves a spatially periodic pattern with a wavelength approximately equal to the hole diameter. The highest amplitudes of $|S_v(f_0)|$ occur immediately adjacent to the tip of the impingement edge. Taken together, the patterns of $|S_u(f_0)|$ and $|S_v(f_0)|$, shown at the top and bottom of Figure 4.1.4, both exhibit peak values in the vicinity of the impingement edge. This observation suggests that the abrupt encounter of the incident organized wave with the tip of the impingement edge, which corresponds to the effective trailing-end of the perforated plate, generates an unsteady, highly organized flow distortion, which could act as an

upstream influence that reinforces the self-sustained oscillation of the turbulent shear layer.

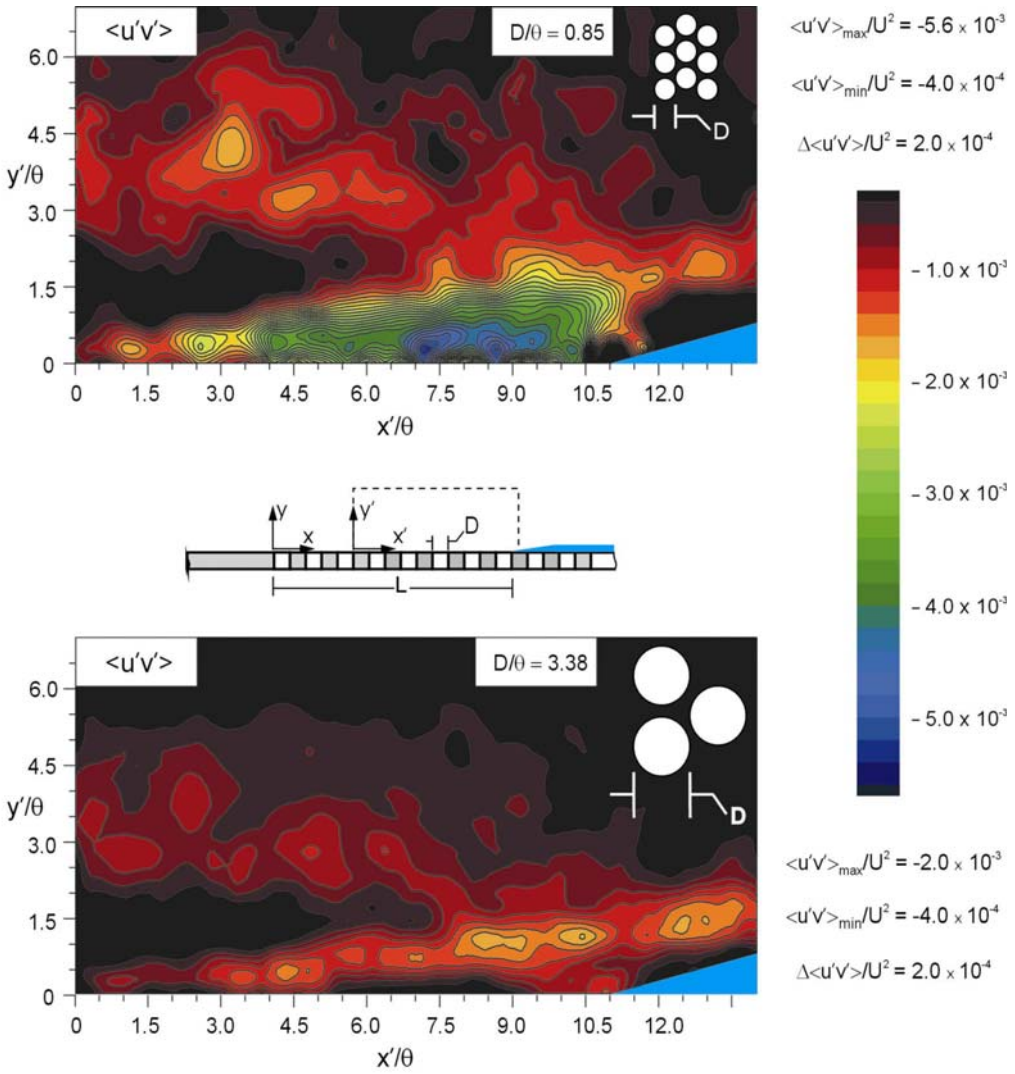

Figure 4.1.1. Patterns of averaged Reynolds stress correlation $<u'v'>/U^2$ for a relatively small diameter hole D/θ = 0.85 (D=6.4mm) and a relatively large diameter D/θ = 3.38 (D=25.4). Minimum and incremental values are $<u'v'>/U^2$=-4x10^{-4} and $\Delta\left[<u'v'>/U^2\right]$=2.0x10^{-4}. Peak values are $\left[<u'v'>/U^2\right]_{max}$=-5.6x10^{-3} for the small hole pattern D/θ = 0.85 and -2.0x10^{-3} for large hole pattern. Location of x' is at x=0.35L. Length of perforated plate is L/θ=17.2.

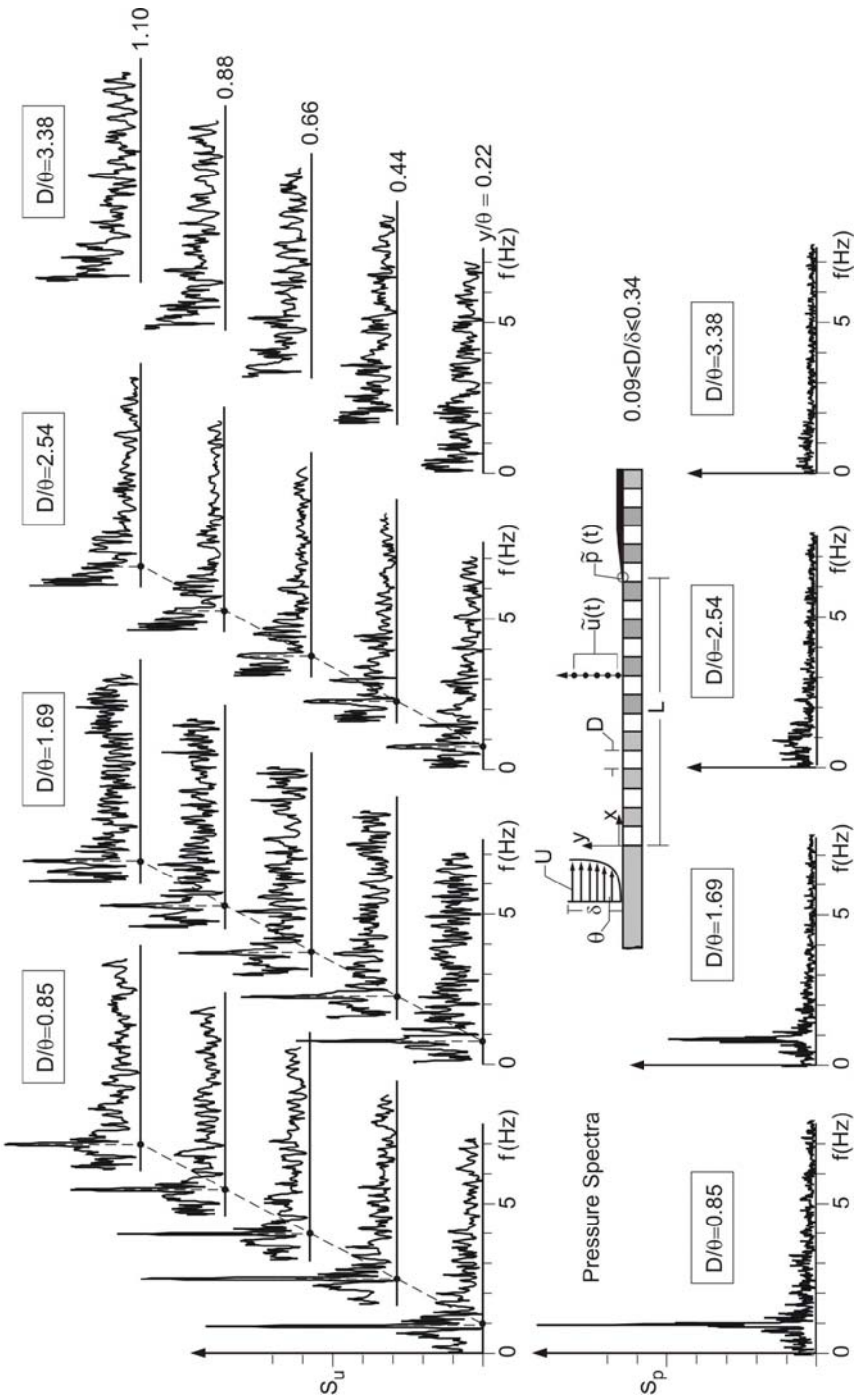

Figure 4.1.2. Spectra of pressure fluctuation S_p at tip of impingement edge in relation to spectra of S_u of longitudinal velocity fluctuation across shear layer at a location x = 0.8L. Sets of spectra are shown for four different values of the dimensionless diameter D/q of the hole of the perforated plate. Length of plate is L/θ= 17.2.

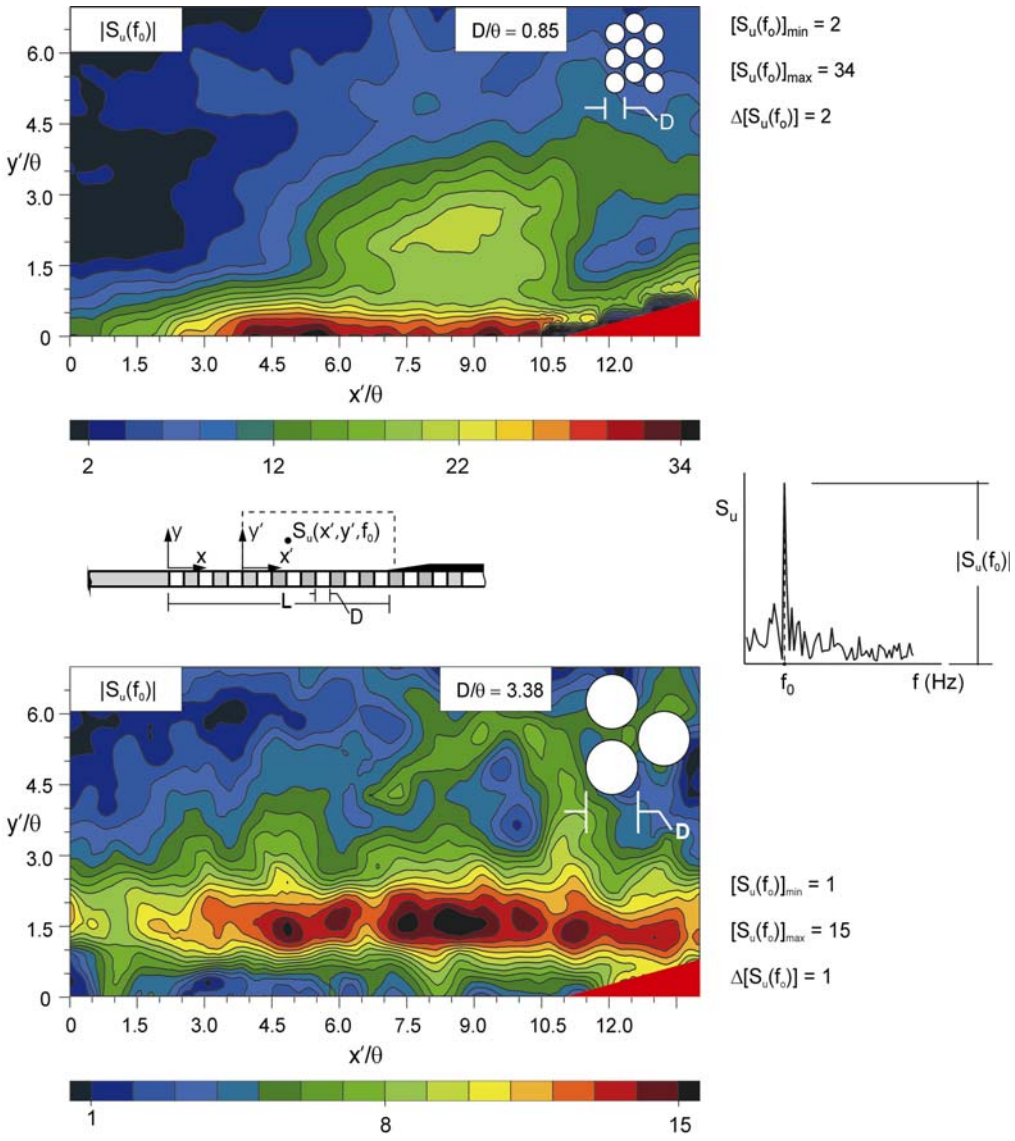

Figure 4.1.3. Contours of constant amplitude of the dominant spectral peak $|S_u(f_0)|$ for the smallest and largest diameter holes D/θ = 0.85 (D=6.4) and 3.38 (D=25.4) of the perforated plate. x'=0 at $x'/L = 0.35$

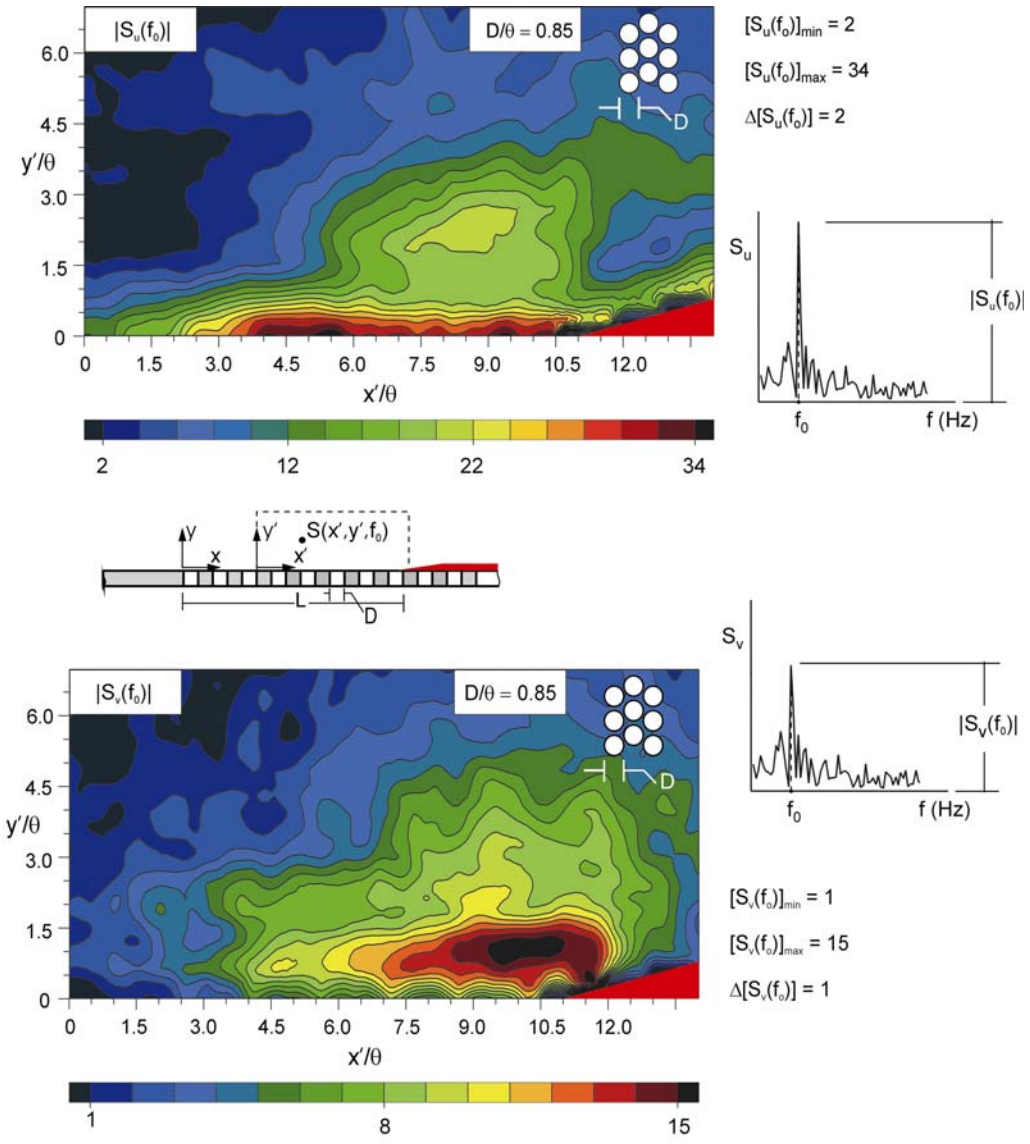

Figure 4.1.4. Contours of constant amplitude of the dominant spectral peak $|S_u(f_0)|$ and $|S_v(f_0)|$ for the smallest diameter holes D/θ = 0.85 (D=6.4) of the perforated plate. x'=0 at $x'/L = 0.35$

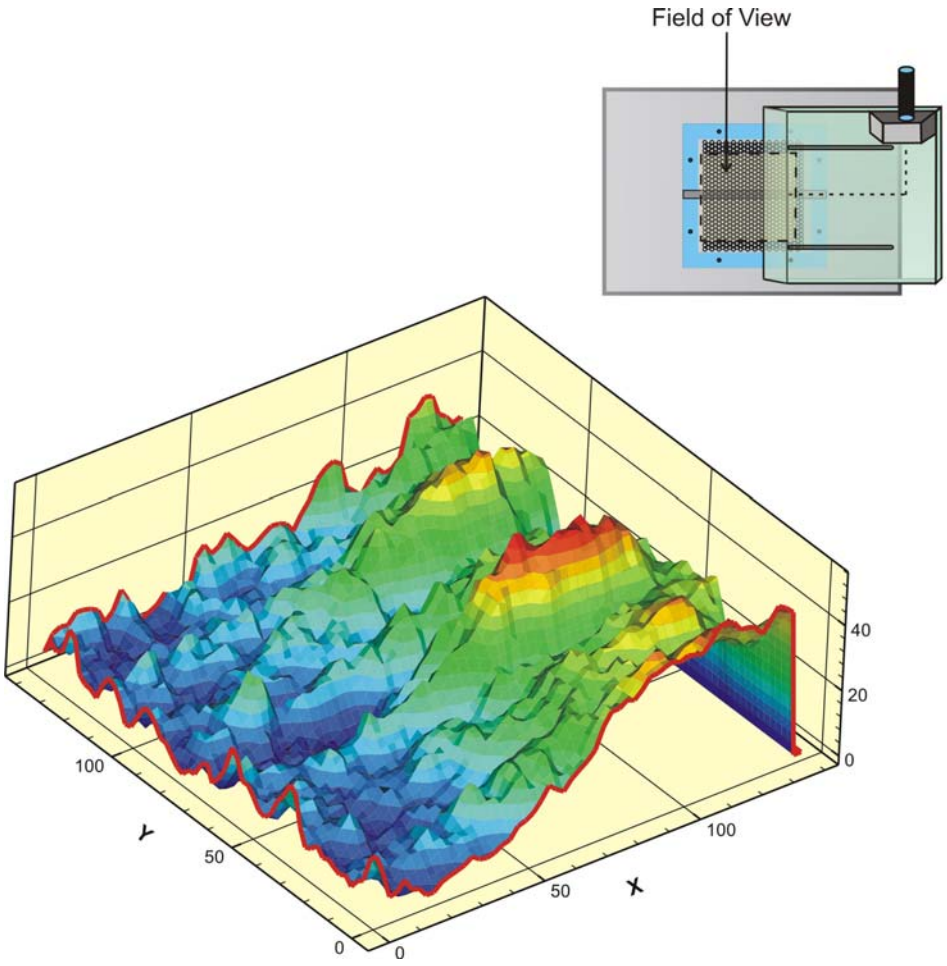

Figure 4.1.5a. Three dimensional contour plot of cross spectral density S_u for the smallest diameter holes $D/\theta = 0.85$.

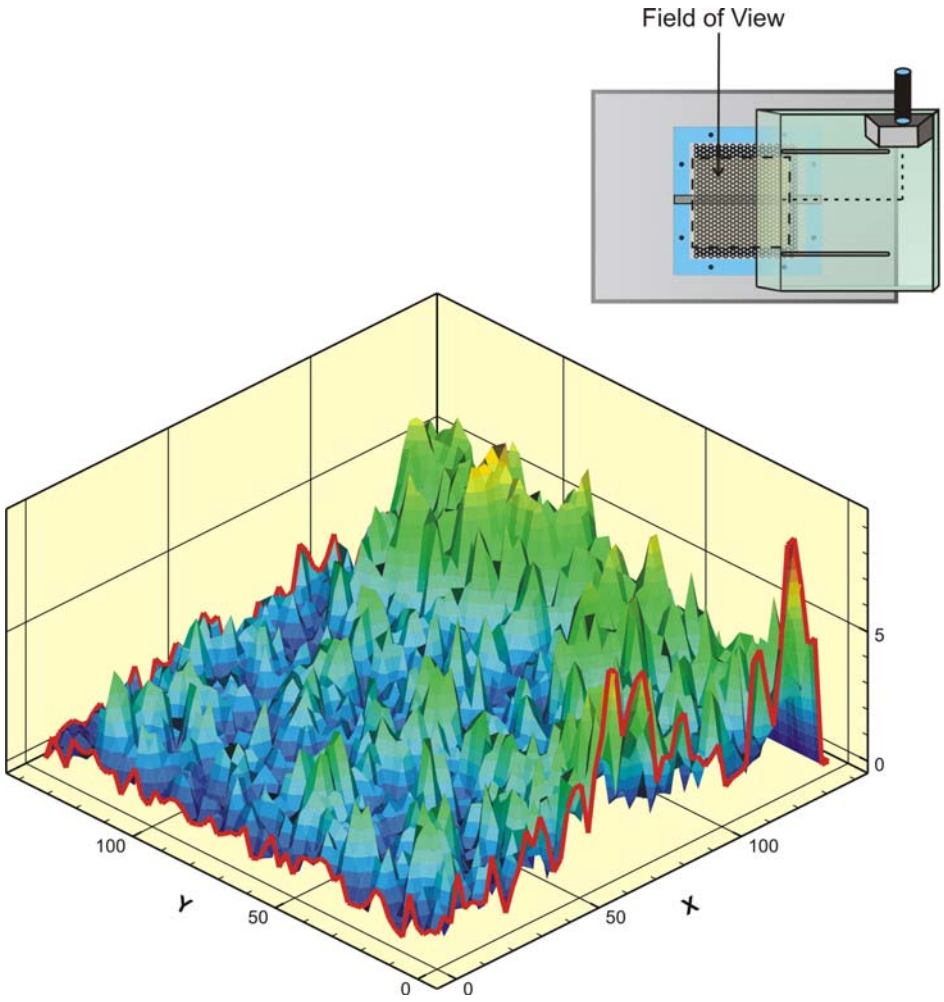

Figure 4.1.5b. Three dimensional contour plot of cross spectral density S_v for the smallest diameter holes $D/\theta = 0.85$.

4.1.3. Scaling of Organized Component of Oscillation

Spectra of the type shown in Figure 4.1.2 were acquired for variations of the effective length of the perforated plate, expressed in normalized form as L/θ and L/D. This variation of L was accomplished by translating the tip of the impingement edge along the surface of the perforated plate, as indicated in the schematic of Figure 4.1.6. As a consequence, it is possible to determine the effect of variation of L/θ (or L/D) for various values of hole diameter D/θ. As shown in both of the plots of Figure 4.1.6, the dimensionless frequency f_0L/U has a band of remarkably constant values lying within the range $f_0L/U = 0.5–0.60$. In other words, the dimensionless frequency f_0L/U is relatively insensitive to both L/θ (or L/D) and D/θ. This reaffirms the viewpoint that the instability along the surface of the perforated plate is a long wavelength phenomenon, and the effect of hole diameter D/θ is to alter the amplitude of the oscillation (see Figure 4.1.2), but not its dimensionless frequency f_0L/U.

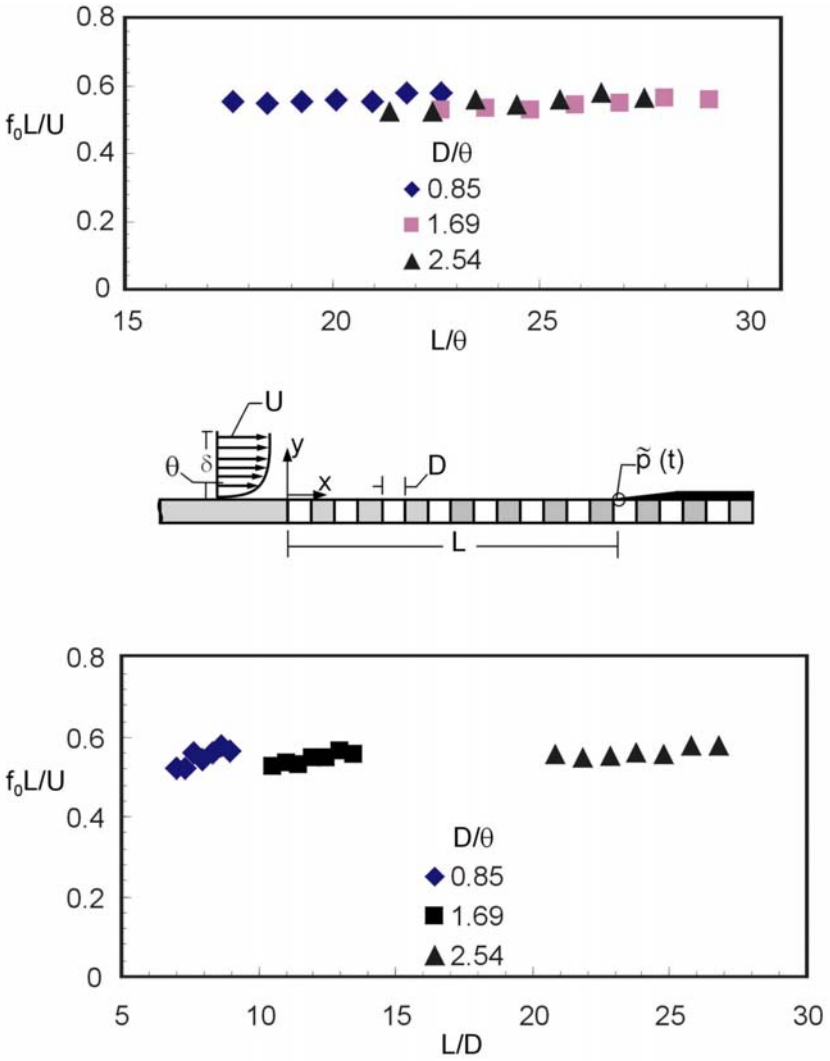

Figure 4.1.6. Variation of dimensionless frequency f_o of predominant spectral peak of pressure fluctuation, normalized by effective length L of perforated plate and freestream velocity U, with respect to dimensionless cavity length L/θ and L/D, in which θ is momentum thickness of the approach flow and D is the diameter of the hole of the perforated plate. Dimensionless frequencies are shown for various D/θ values.

4.1.4. Form Of Organized Wave Along Perforated Plate

It is evident from the preceding section that a highly organized instability can exist in the nominally turbulent shear flow along the perforated plate. In order to determine the amplitude and phase distributions of this organized component across the shear layer, cross-spectral analysis was performed for the fluctuations of the longitudinal component $\tilde{u}(x_0,y,t)$ the transverse (vertical) component $\tilde{v}(x_0,y,t)$ and the vorticity $\tilde{w}(x_0,y,t)$. The amplitude distributions of each of these components are shown in Figure 4.1.7a-a as a function of vertical distance y/θ from the surface of the plate, in comparison with the time-averaged longitudinal velocity $\tilde{u}/U$. The corresponding phase angle variations are given in Figure 4.1.7a-b. Whereas the phase $\phi_{\tilde{v}}$ of the transverse (vertical) component $\tilde{v}(x_0,y,t)$ exhibits only mild phase variations, the longitudinal phase $\phi_{\tilde{u}}$ shows a phase jump, i.e., a change in sign. The phase of the vorticity fluctuation $\phi_{\tilde{w}}$ increases substantially with distance from the surface of the perforated plate. With the foregoing amplitude and phase distributions, it is possible to reconstruct the time-dependent variation of the longitudinal component of the wave-like motion. Distributions of instantaneous longitudinal velocity $\tilde{u}(x_0,y,t)$ are shown for sequential instants t/T during the oscillation cycle in the plot at the bottom left of Figure 4.1.7b. These distributions were obtained from the distributions of amplitude and phase given in Figures 4.1.7a-a and 7b-b.

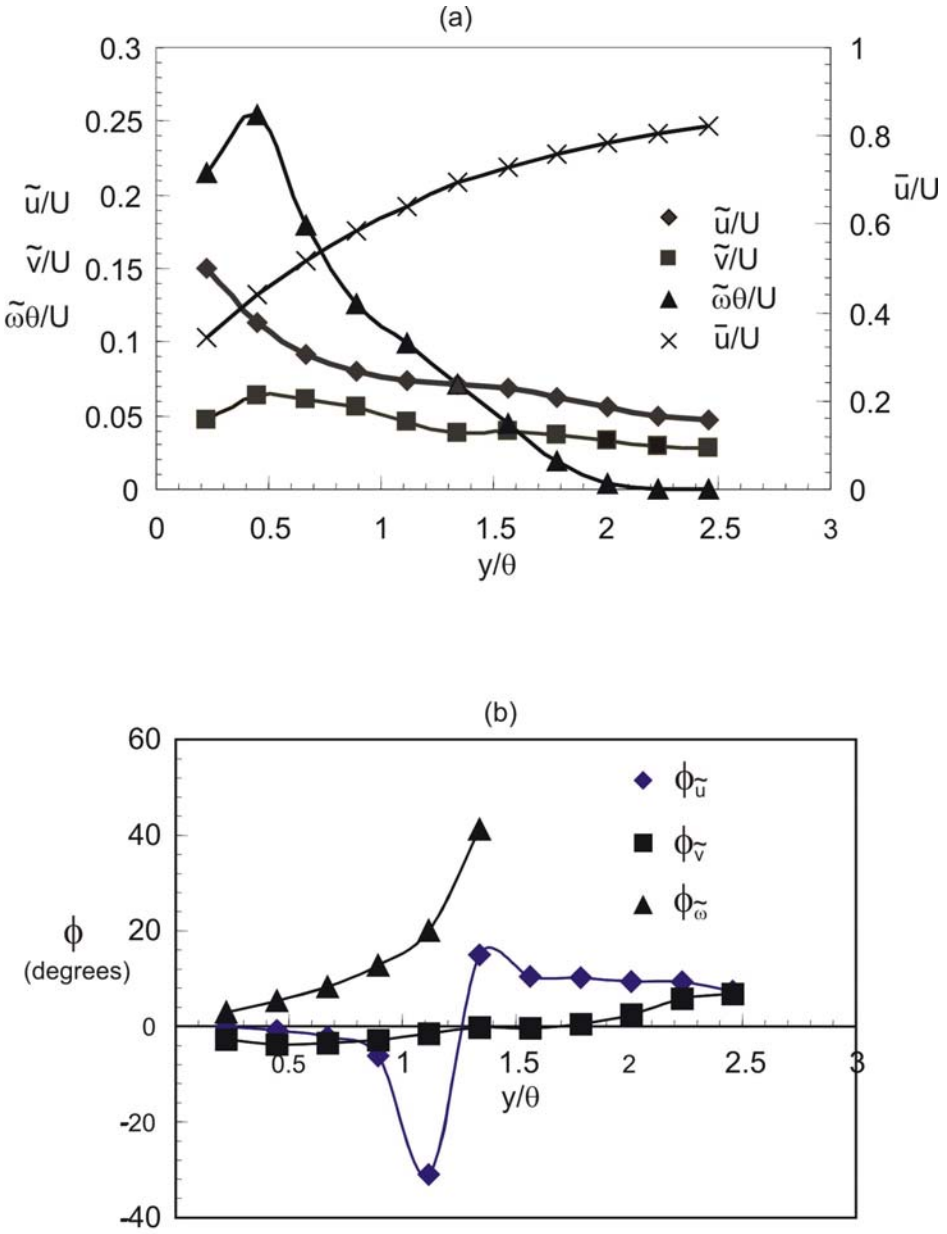

Figure 4.1.7a. Variation of amplitude and phase of organized velocity and vorticity fluctuations and their corresponding phase angles across the shear layer at locations indicated in the schematic. Hole diameter is D/θ = 0.85. Plot (a) shows the amplitudes of the longitudinal and transverse velocity fluctuations $\tilde{u}/U$ and $\tilde{v}/U$, as well as the vorticity $\tilde{\omega}\theta/U$, in which U is the freestream velocity as a function of transverse distance y/θ across the shear layer, in which is momentum thickness. Plot (b) shows the phase angle ϕ of the velocity fluctuations ϕ_u and ϕ_v, as well as vorticity fluctuations ϕ_ω as a function of y/θ. Datas were acquired at 0.8L. Length of perforated plate is L/θ = 17.2.

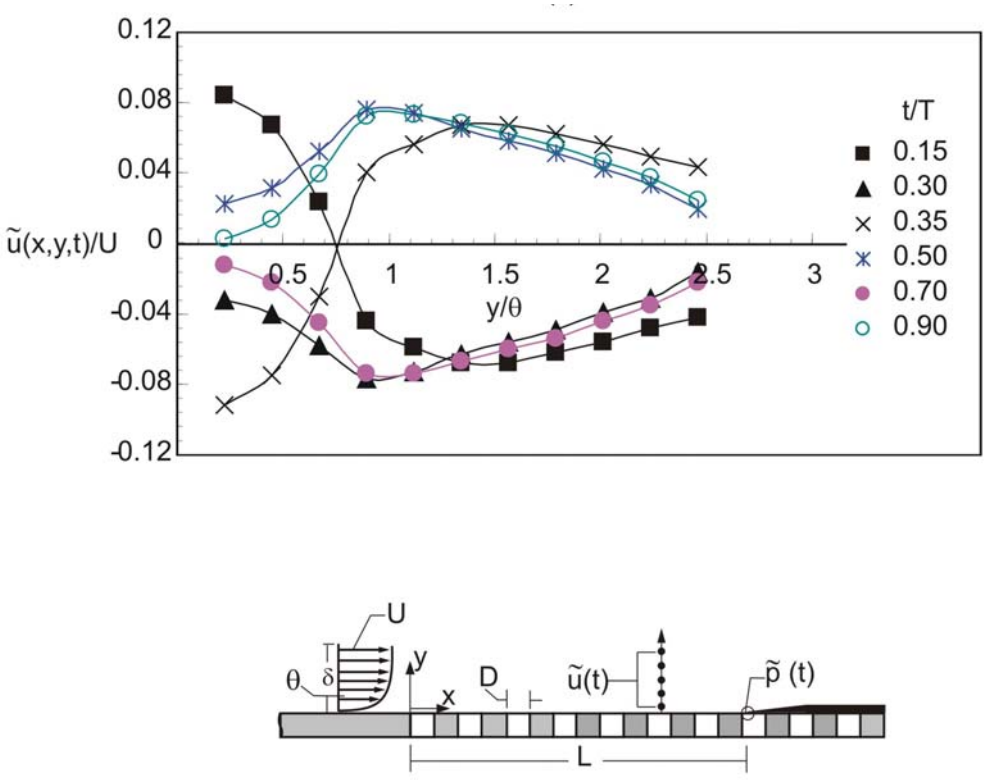

Figure 4.1.7b. Instantaneous distributions of the velocity fluctuations $\tilde{u}(x_0, y, t)$ as a function of distance y/θ. Datas were acquired at 0.8L. Length of perforated plate is L/θ = 17.2.

4.1.5. Quantitative Visualization of Flow Structure

The organized fluctuations described in the foregoing sections are associated with time sequences of global visualization of the flow structure. Figure 4.1.8a and 4.1.8b show patterns of instantaneous vorticity and velocity correlation $\langle u'v' \rangle$ over five frames N of the cinema sequence. Diameter of holes in plate is $D/\theta = 0.85$. Time t is normalized by the period T of the cycle of the oscillation. For the vorticity contours, the minimum and incremental values are $\omega_{min} = -6\ sec^{-1}$ and $\Delta\omega_{min} = -2\ sec^{-1}$. For instantaneous velocity correlation, minimum and incremental values are $[u'v'/U^2]_{min} = 3.7x10^{-3}$ and $[u'v'/U^2] = 3.7x10^{-3}$. Upper boundary of each image corresponds to a distance of $y = 3.36\theta$ from surface of the perforated plate.

The organized cluster of vorticity contains small-scale concentrations of vorticity. At increasing values of N; the cluster of elongated vorticity becomes more focused and is swept above the upper surface of the impingement edge. The corresponding patterns of the instantaneous correlation $\langle u'v' \rangle$ generally retain their integrity as they are swept downstream along the surface of the plate. Again, small-scale concentrations of $\langle u'v' \rangle$ are evident.

The spanwise nature of the instantaneous flow structure was examined using the laser sheet and camera arrangements shown in Fig. 3.10. The laser sheet was oriented vertically, such that it was parallel to the surface of the plate, and its centerline was 1mm from the surface.

Figure 4.1.9a and 4.1.9b shows the instantaneous patterns of longitudinal u velocity vectors as a function of frame number N* in a cinema sequence. Dark regions correspond to high velocity, and light regions to low velocity. For the smallest hole pattern, for which organized oscillations occur, the images at N* = 0, 2 and 4, show the onset of a well-defined front, i.e., a sharply defined interface between low and high magnitudes of u vectors, the streamwise striations of large amplitude vectors notwithstanding. The advancement of this front from left to right is in accord with the movement of the patterns of instantaneous vorticity and Reynolds

stress correlation <u′v′> with increasing cinema frame sequence N shown in Figure 4.1.8a and Figure 4.1.8b.

On the other hand, for the largest hole pattern, represented by the Figure 4.1.9b a well-defined front does not occur. Rather, regions of high and low velocities appear to be randomly distributed over the surface of the plate. This lack of organization is in agreement with the nature of the spectra given in Figure 4.2, for which no well-defined spectral component is evident.

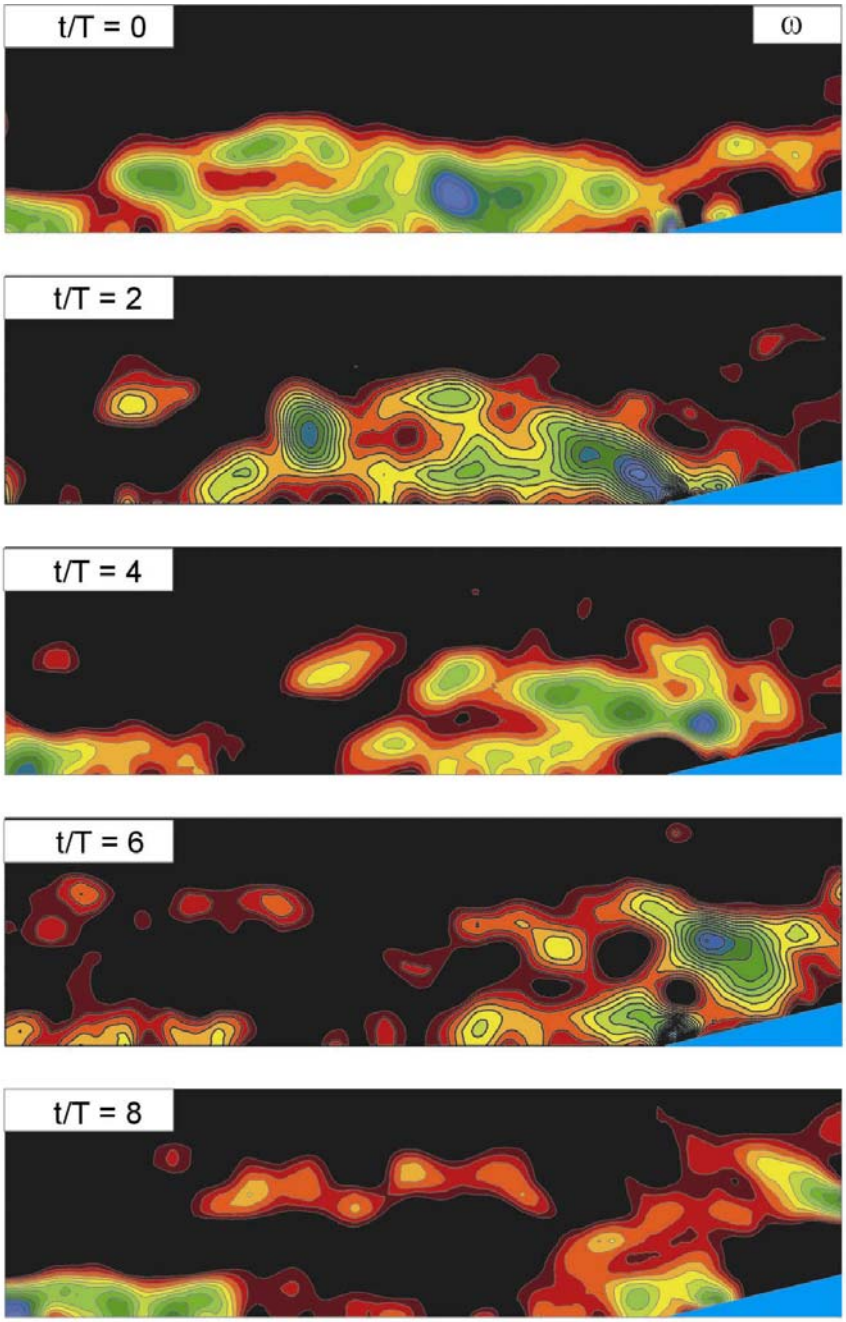

Figure 4.1.8a. Time sequence of contours of constant instantaneous vorticity Diameter of holes in plate is $D/\theta = 0.85$. Time t is normalized by the period T of the cycle of the oscillation. For the vorticity contours, the minimum and incremental values are $\omega_{min} = -6\ s^{-1}$ and $\Delta\omega_{min} = -2\ s^{-1}$. Upper boundary of each image corresponds to a distance of $y = 3.36\theta$ from surface of the perforated plate.

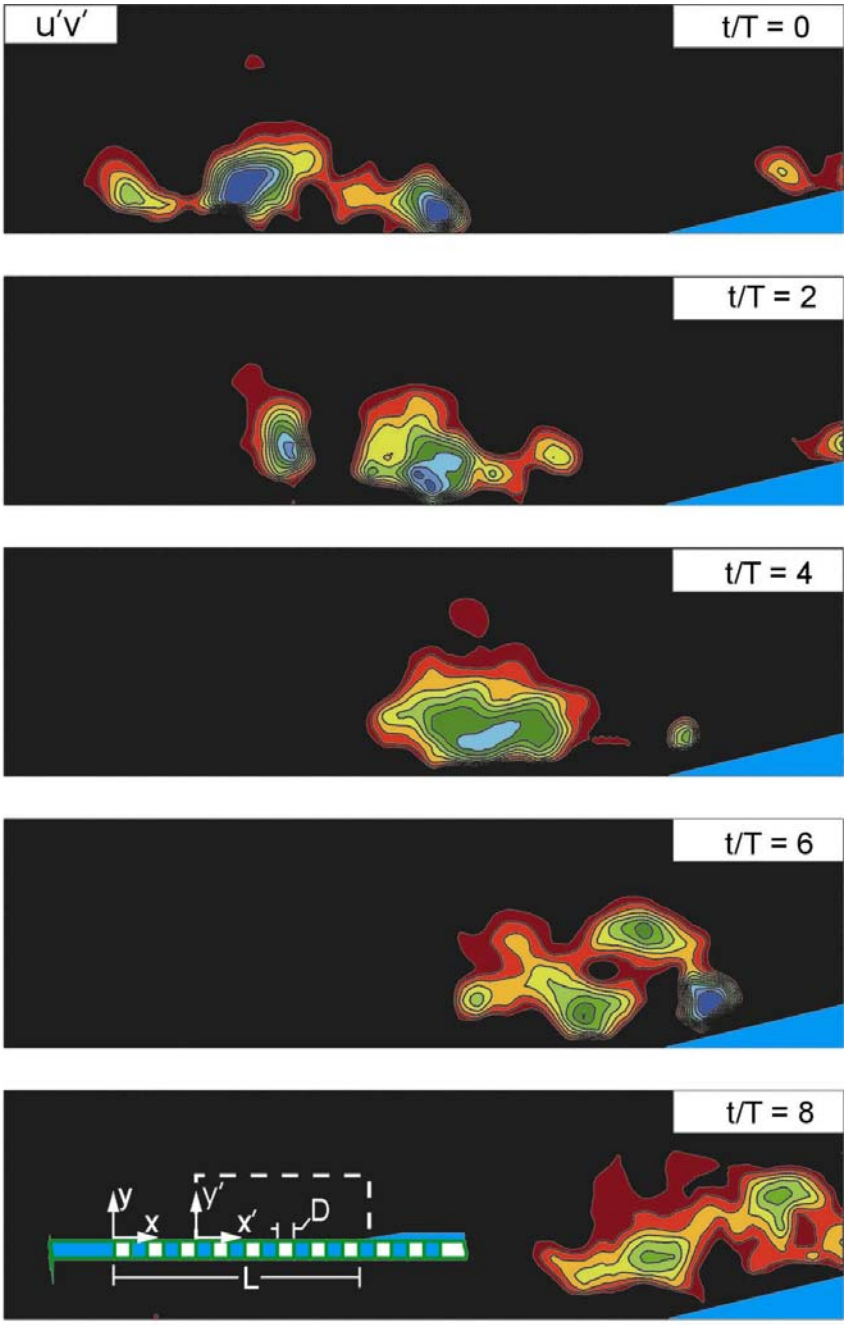

Figure 4.1.8b. Time sequence of instantaneous velocity correlation, minimum and incremental values are $[<u'v'>/U^2]_{min}$ = 3.7x10^{-3} and $[<u'v'>/U^2]$ = 3.7x10^{-3}. Upper boundary of each image corresponds to a distance of y = 3.36θ from surface of the perforated plate.

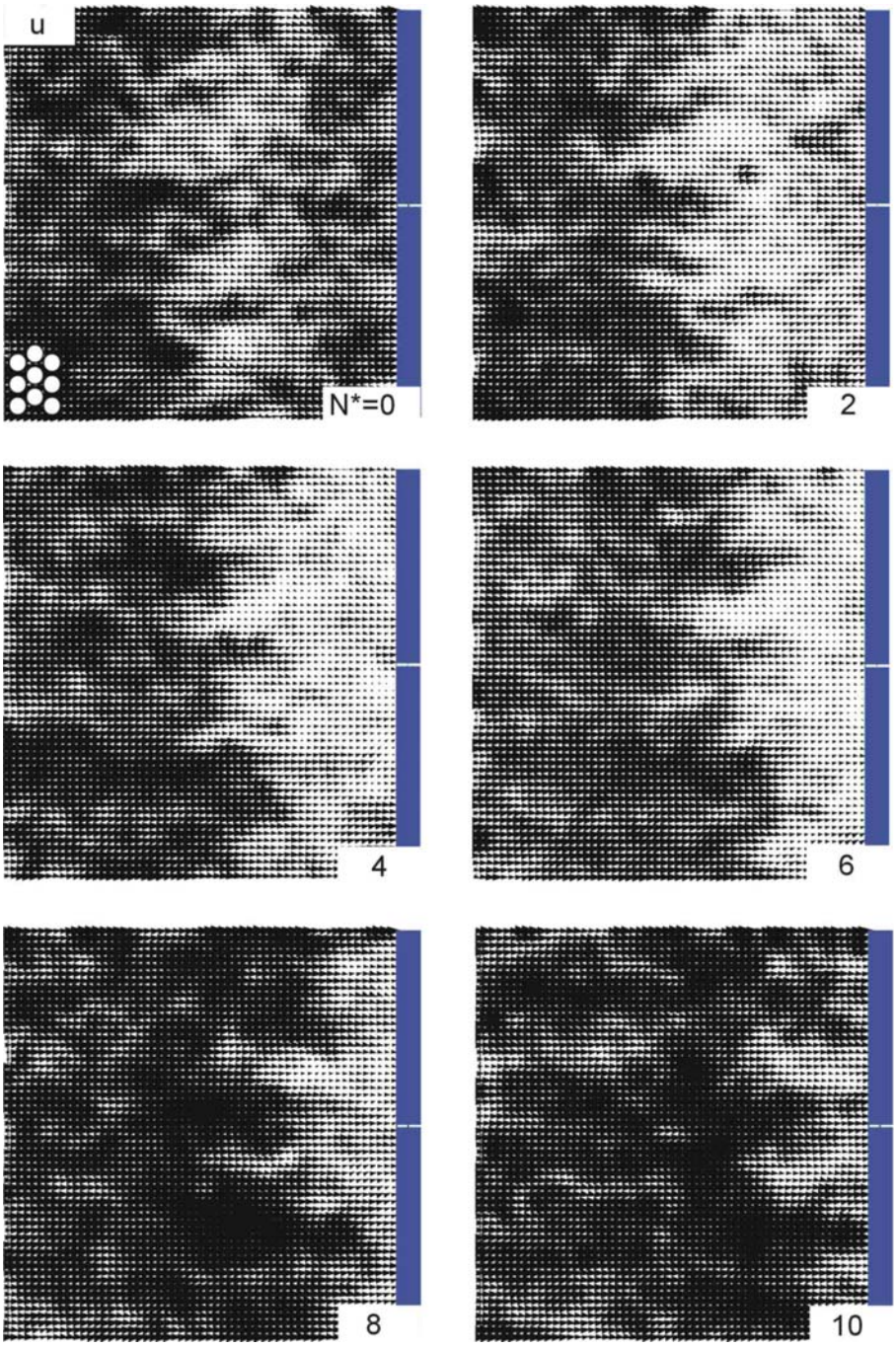

Figure 4.1.9a. Patterns of instantaneous vectors of the longitudinal (streamwise) component of velocity u for perforated plates having a small hole D/θ=0:85; N* represents the frame number of the cinema sequence. For the case of the small hole D/θ=0:85; the oscillation is relatively coherent, and its period extends from $N^* = 0$ to $N^* = 16$.

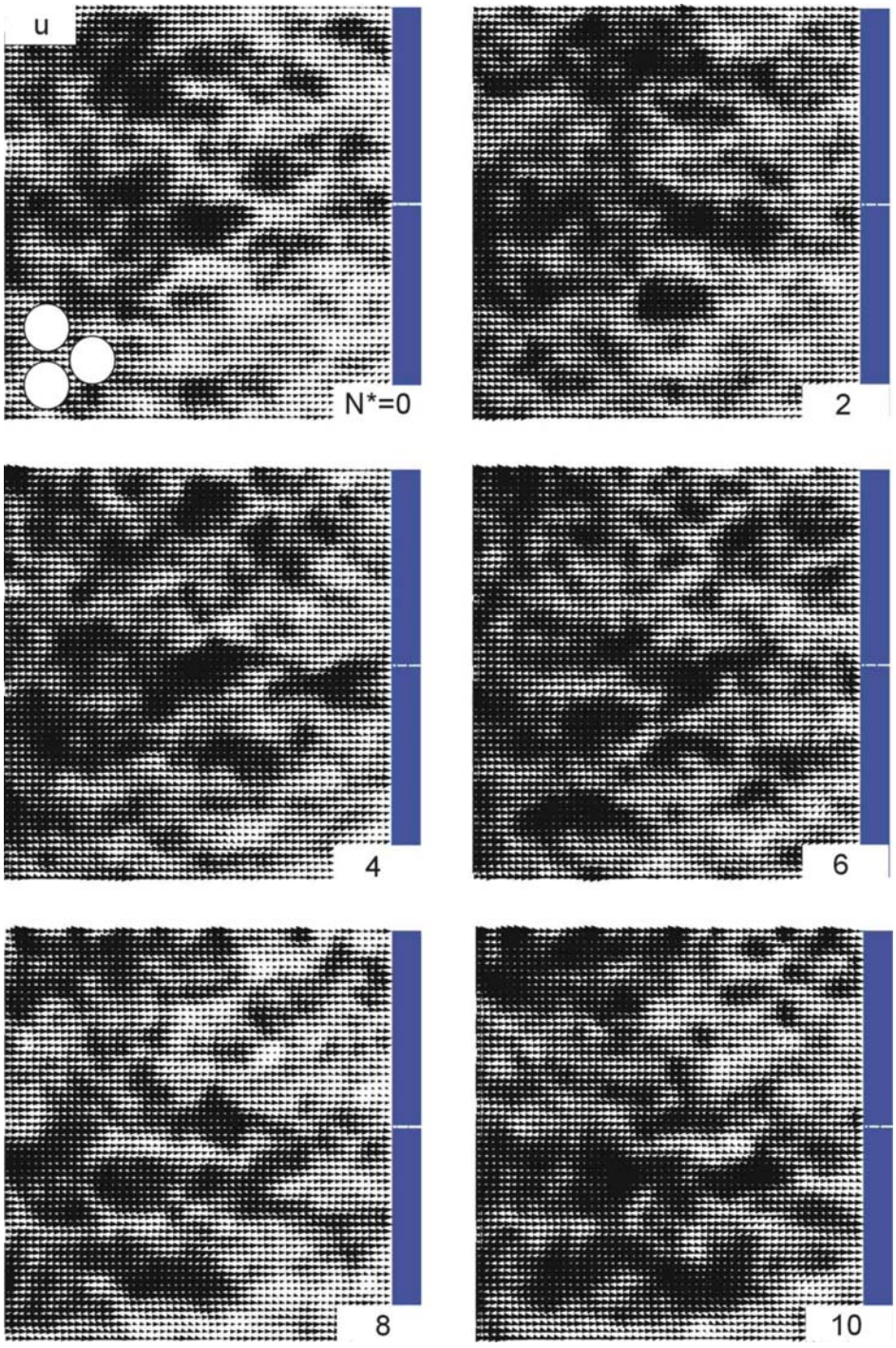

Figure 4.1.9b. Patterns of instantaneous vectors of the longitudinal (streamwise) component of velocity u for perforated plates having a small hole D/θ=3.36; N* represents the frame number of the cinema sequence.

4.2. Pressure Fluctuations

In order to characterize the oscillations through the cavity length pressure signals were acquired at different locations. Pressure records of continuous duration of 102.4 sec., corresponding to, for example 2048 cycles of a fluctuation at 0.05 sampling time, were recorded at values impingement length L to momentum thickness θ ratio, L/θ=17.75, 18.5, 19.25, 20, 20.75, 21.5 and 22.25 for each perforated plates. These pressure signals are represented in the form of simple time traces and corresponding plots of spectral density. Each of pressure time traces was subjected to a Fast-Fourier transform (FFT) to provide the spectra. Spectral analysis is a powerful tool for characterizing dynamic systems. Spectral analysis is using to identify the coherence and strength of oscillations. Fourier transform of corresponding auto-correlation functions make it possible to determine the coherence of periodic fluctuations of pressure and velocity at a single point. Spectral analysis of the pressure signals carried out in accord with the procedures outlined by Newland (1993).In essence the definition for the spectrum is $S_k \frac{1}{Nf_s} X_k^* X_k$ in which N is the number of data points f_s is the sampling frequency X_k is the fast Fourier transform (FFT) of time series and X_k^* is its complex conjugate. For evaluation of S_p the values of sampling frequency had values 10. During the acquisition of the pressure data, the sampling rate was set to 20 samples per second to have Nyquist frequency of 10 Hz. The maximum frequency for the present study was found approximately 0.997 Hz and the Nyquist criterion was thereby satisfied. During the pressure data measurements the inflow velocity U was maintained at a constant value while the effective length L of the plate was varied.

In order to characterize the temporal variation of the unsteady shear layer impinging upon the cavity length pressure signals were acquired at crucial locations. Preliminary scoping experiments, involving variation of the impingement length L, were carried out using the pressure signal at the tip of impingement plate. These pressure signals are presented in the form of simple time traces and corresponding plots of spectral density.

Figures 4.2.1-4.2.7 show pressure signal time traces and corresponding spectra for D/θ=0.85. In this figures values of frequency of the spectral peak were in the range *f*=0.811 to 0.997. While impingement length L to momentum thickness θ ratio L/θ, increasing from 17.75 to 22.25, frequency of the spectral peak decreasing from 0.997 to 0.811. The maximum amplitude of the fundamental pressure component occurs at approximately L/θ=20.75. The energy is more concentrated at the fundamental L/θ=20.75 value. The minimum amplitude of the pressure component occurs at L/θ =17.75.

Figures 4.2.8-4.2.14 show pressure signal time traces and corresponding spectra for D/θ=1.7. In this figures values of frequency of the spectral peak were in the range *f*=0.762 to 0.928. While impingement length L to momentum thickness θ ratio L/θ, increasing from 17.75 to 22.25, frequency of the spectral peak decreasing from 0.928 to 0.762. The maximum amplitude of the fundamental pressure component occurs at approximately L/θ=22.25 and its value is 0.186. The energy is more concentrated at the fundamental L/θ=22.25 value. The minimum amplitude of the pressure component is 0.064 and it occurs at L/θ =17.75. The amplitudes of pressure spectra component are lower than the amplitudes of D/θ=0.85 perforated plate.

Figures 4.2.15-4.2.21 show pressure signal time traces and corresponding spectra for D/θ=2.54. In this figures frequency of the spectral peak is not detectable for the L/θ=17.75, 18.5, 19.25 lengths. After the impingement length to momentum thickness ratio is L/θ = 20.0, frequency of the spectral peak is detectable. It ranges between the *f* = 0.771 to 0.830. The maximum amplitude of the fundamental pressure component occurs at approximately L/θ=22.25 and its value is 0.064. The minimum amplitude of the pressure component is 0.032 and it occurs at L/θ =20.75.

Figures 4.2.22-4.2.28 show pressure signal time traces and corresponding spectra for D/θ=3.4. In this figures frequency of the spectral peak is not detectable for the all L/θ dimensionless impingement lengths.

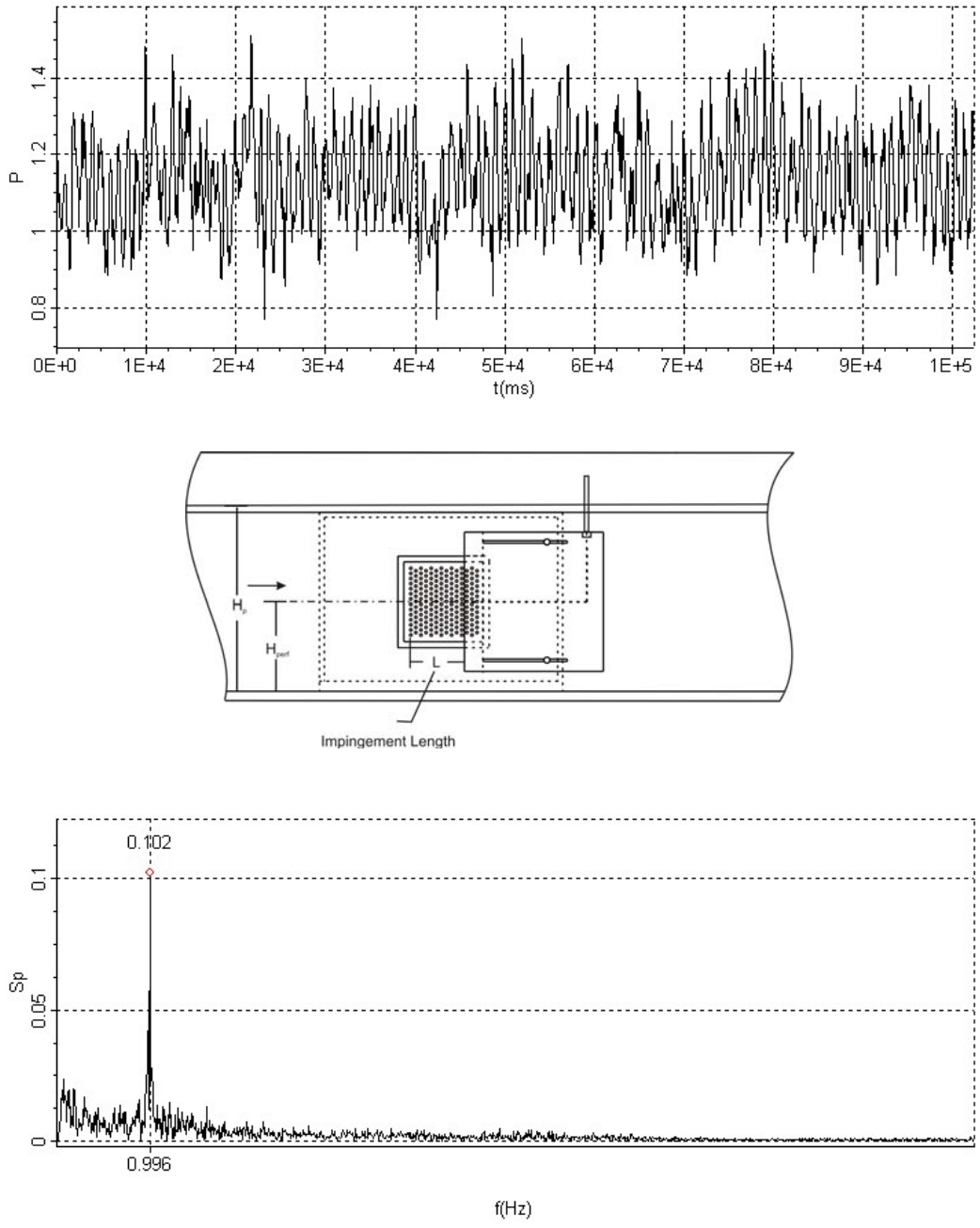

Figure 4.2.1. Time trace and spectrum of pressure fluctuation at tip of impingement edge. Sampling time is $\Delta t = 0.05$sec; Nyquist frequency is 10 Hz. Perforated plate diameter to momentum thickness ratio is $D/\theta = 0.85$ and impingement length to momentum thickness ratio is $L/\theta = 17.75$

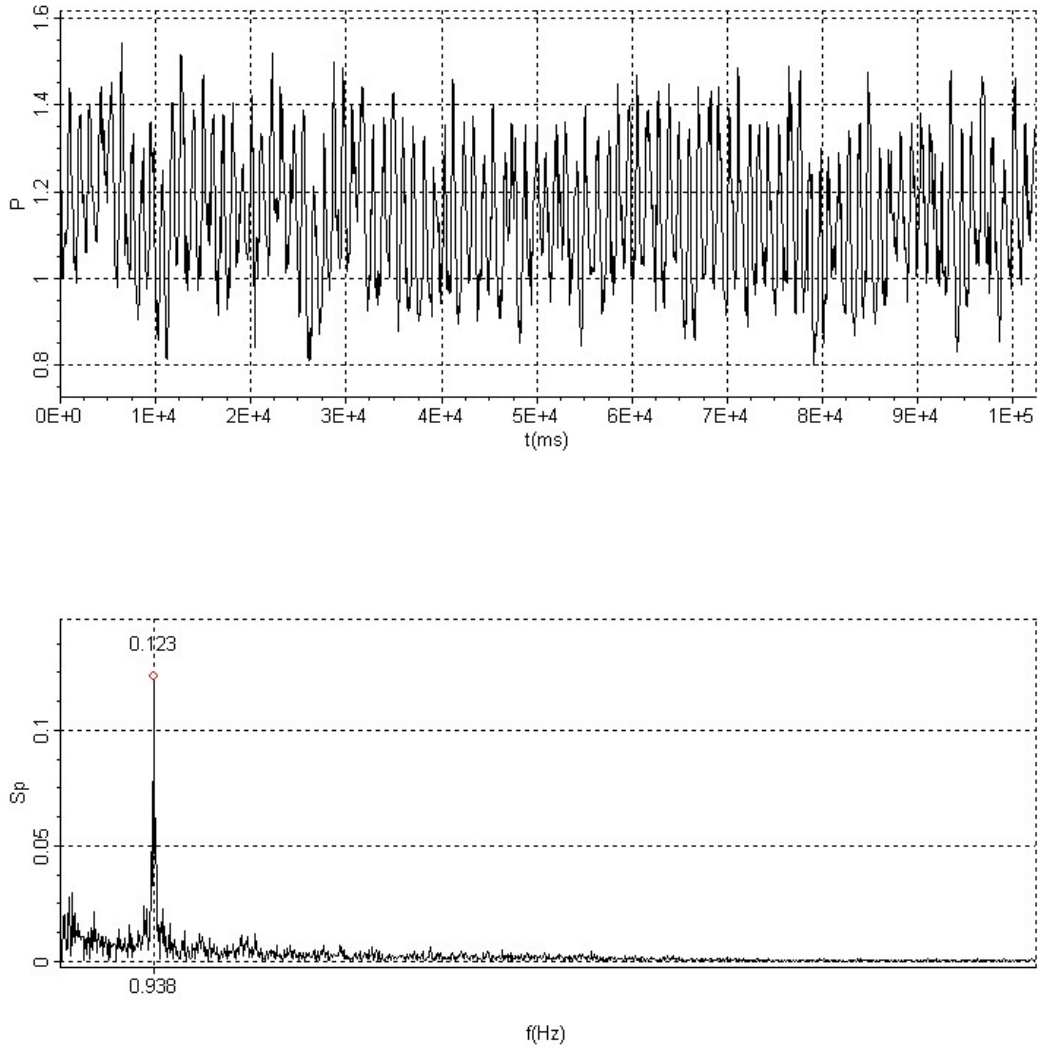

Figure 4.2.2. Time trace and spectrum of pressure fluctuation at tip of impingement edge. Sampling time is $\Delta t = 0.05$sec; Nyquist frequency is 10 Hz. Perforated plate diameter to momentum thickness ratio is $D/\theta = 0.85$ and impingement length to momentum thickness ratio is $L/\theta = 18.5$

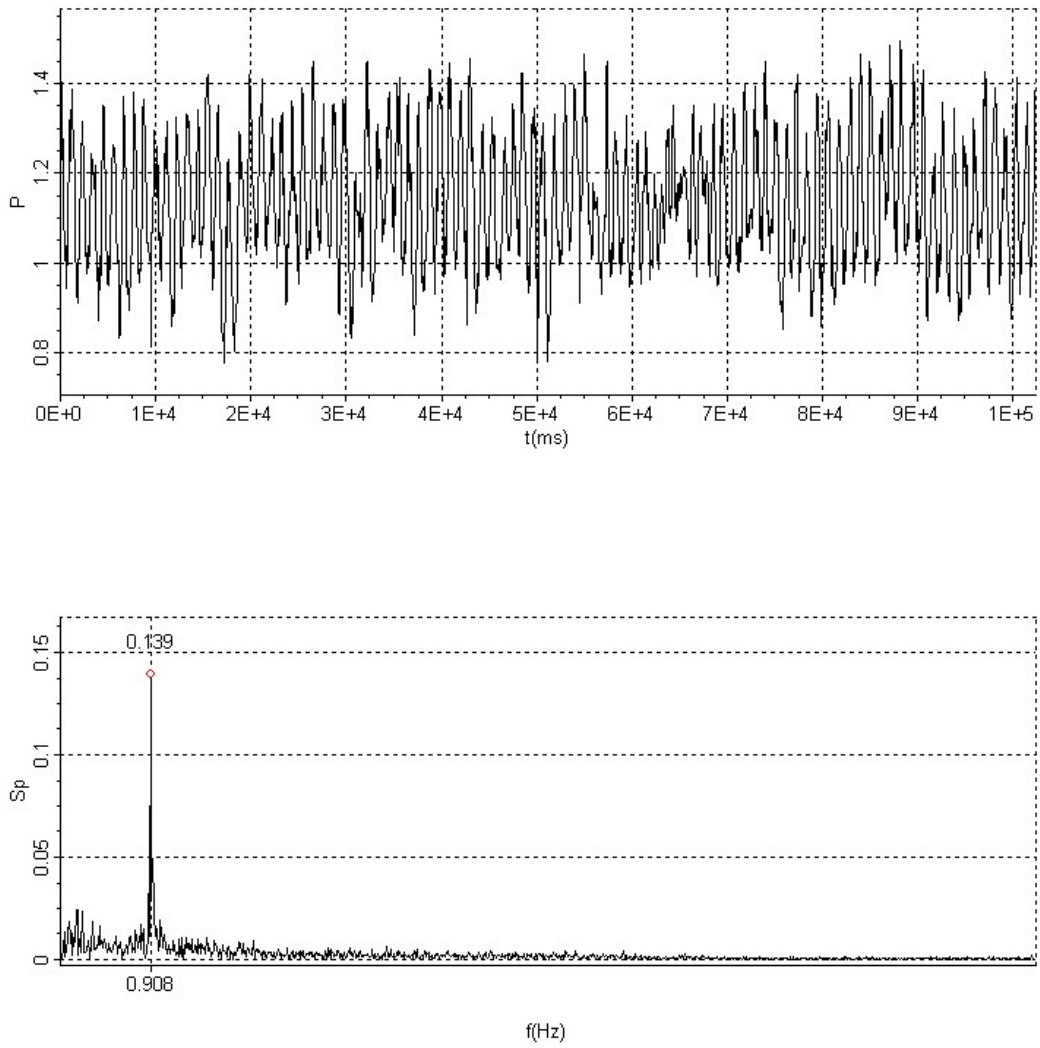

Figure 4.2.3. Time trace and spectrum of pressure fluctuation at tip of impingement edge. Sampling time is $\Delta t = 0.05$sec; Nyquist frequency is 10 Hz. Perforated plate diameter to momentum thickness ratio is $D/\theta = 0.85$ and impingement length to momentum thickness ratio is $L/\theta = 19.25$

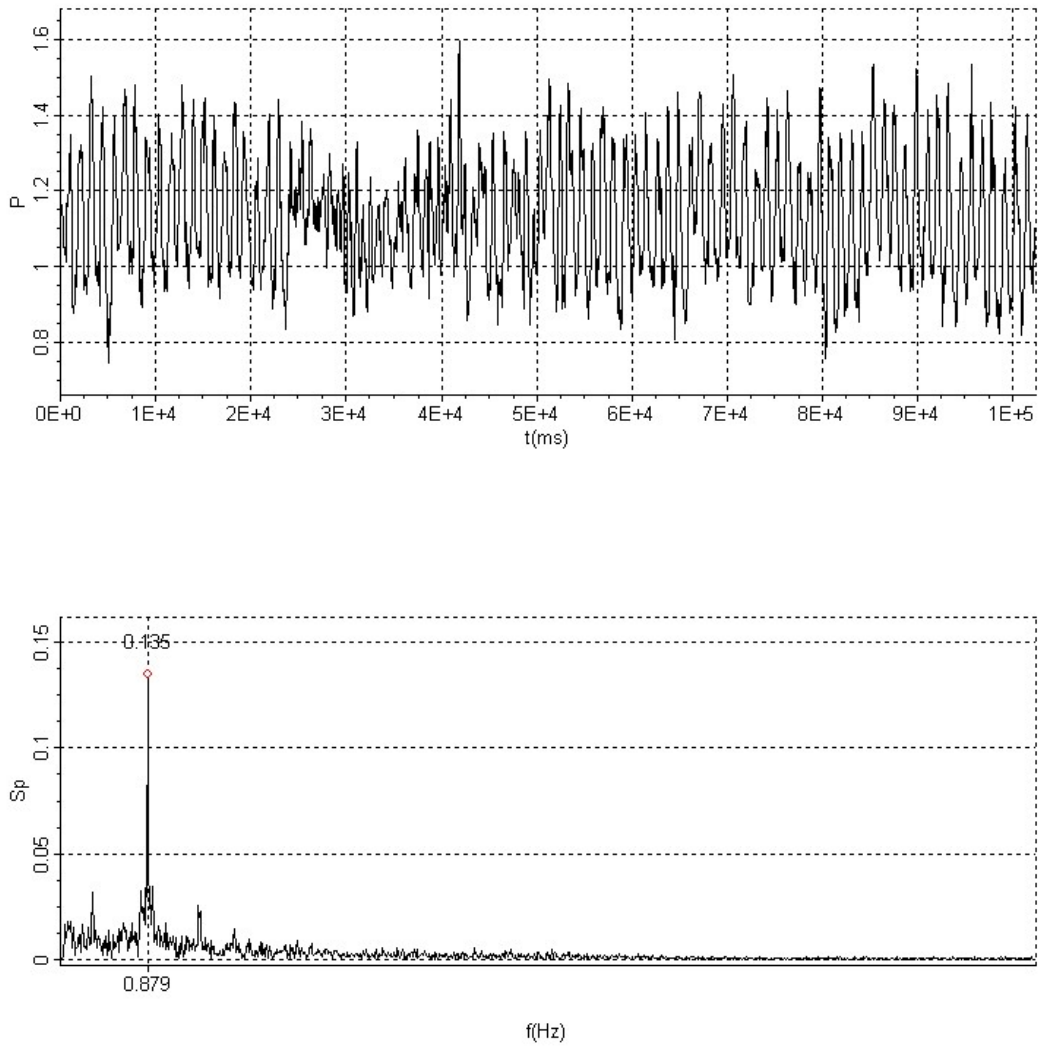

Figure 4.2.4. Time trace and spectrum of pressure fluctuation at tip of impingement edge. Sampling time is $\Delta t = 0.05$sec; Nyquist frequency is 10 Hz. Perforated plate diameter to momentum thickness ratio is $D/\theta = 0.85$ and impingement length to momentum thickness ratio is $L/\theta = 20$

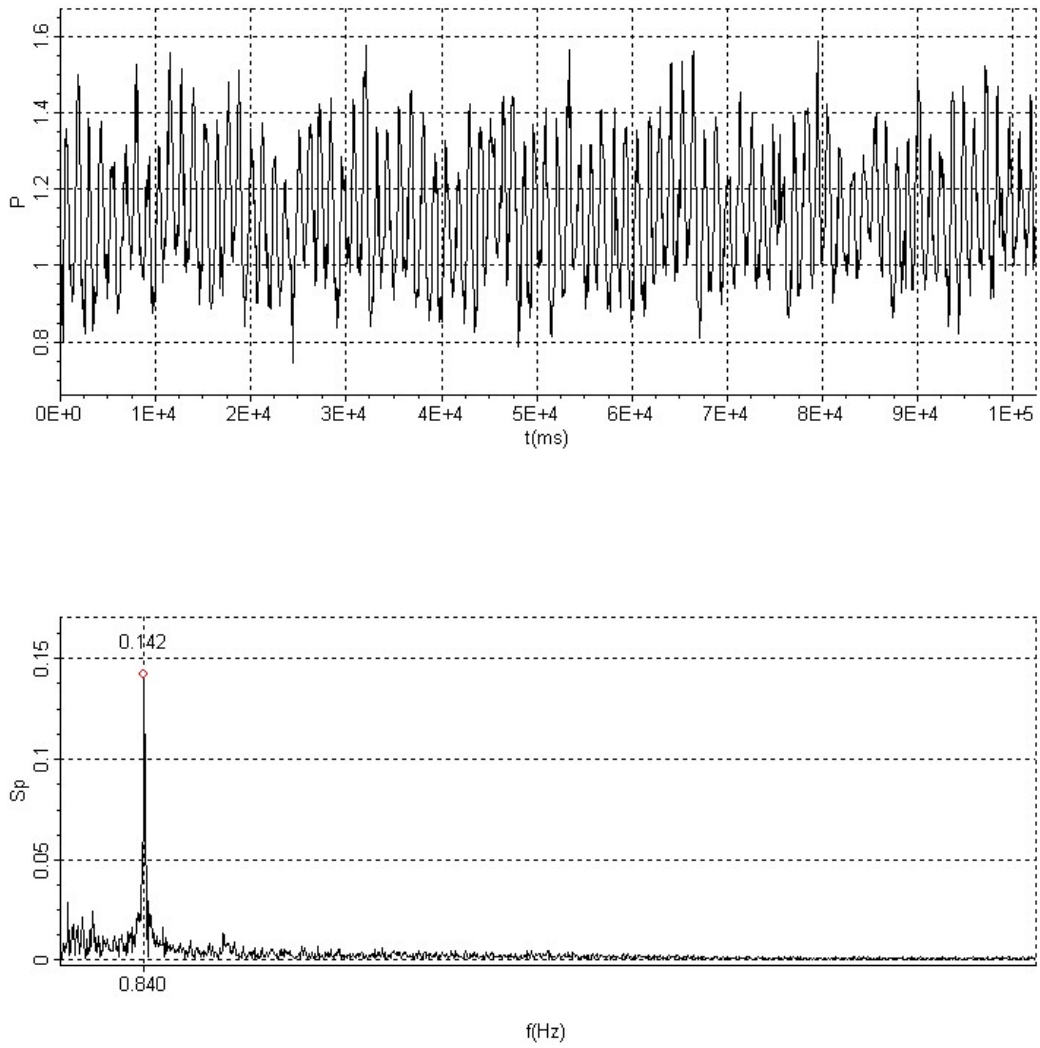

Figure 4.2.5. Time trace and spectrum of pressure fluctuation at tip of impingement edge. Sampling time is $\Delta t = 0.05$sec; Nyquist frequency is 10 Hz. Perforated plate diameter to momentum thickness ratio is $D/\theta = 0.85$ and impingement length to momentum thickness ratio is $L/\theta = 20.75$

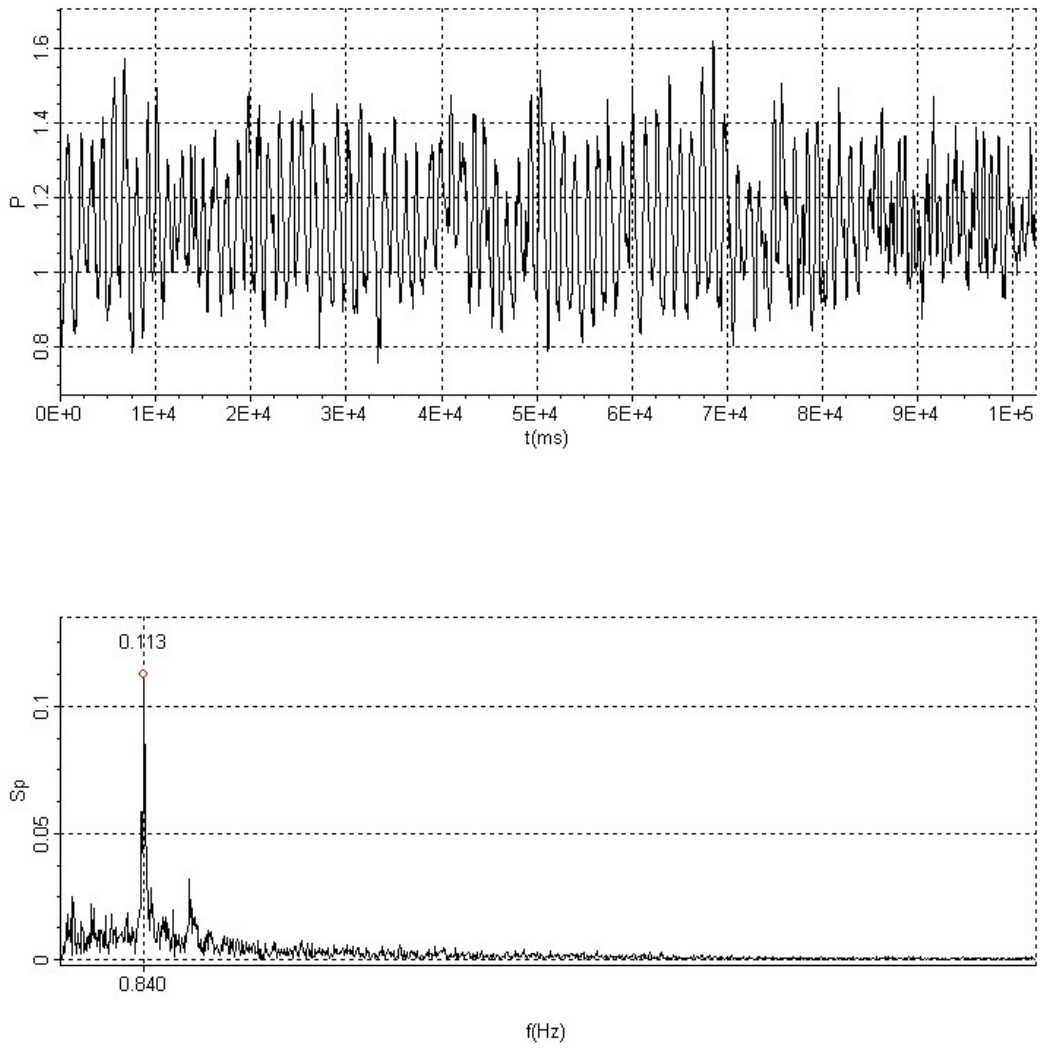

Figure 4.2.6. Time trace and spectrum of pressure fluctuation at tip of impingement edge. Sampling time is $\Delta t = 0.05$sec; Nyquist frequency is 10 Hz. Perforated plate diameter to momentum thickness ratio is $D/\theta = 0.85$ and impingement length to momentum thickness ratio is $L/\theta = 21.5$

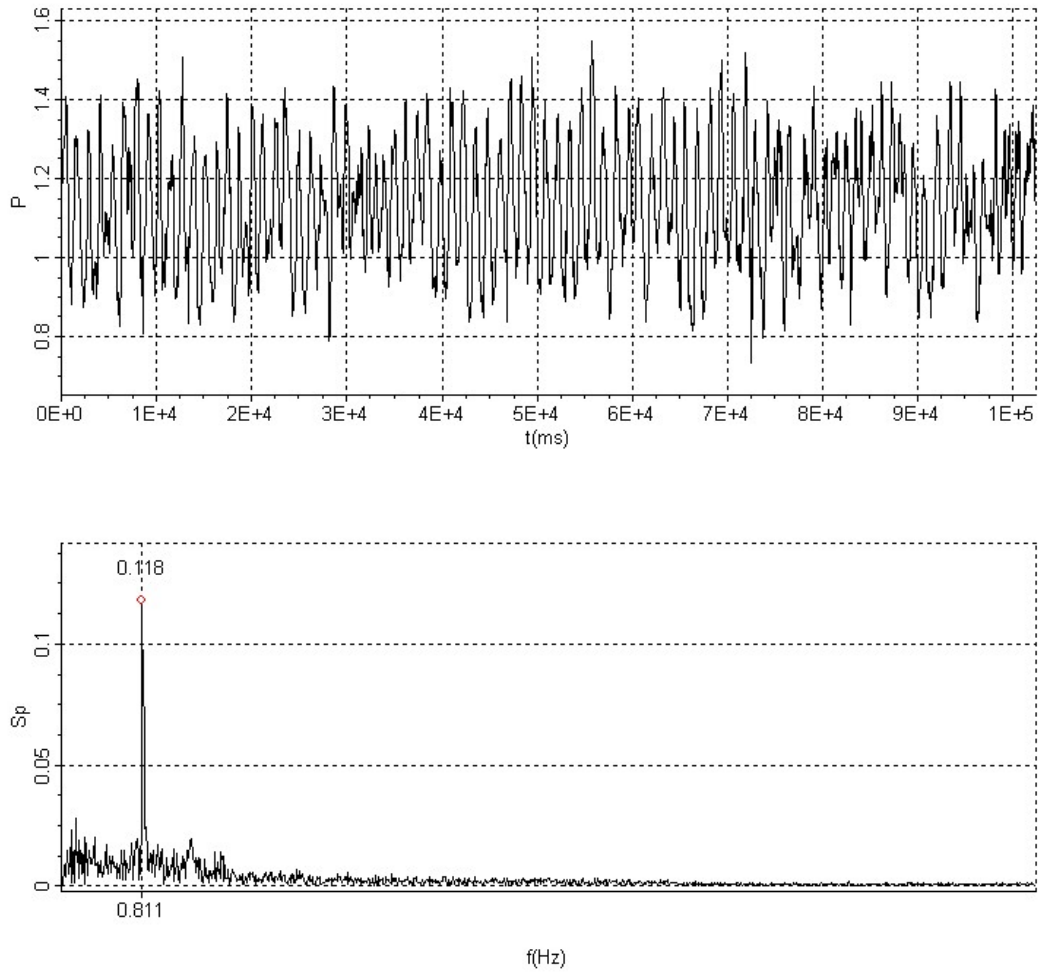

Figure 4.2.7. Time trace and spectrum of pressure fluctuation at tip of impingement edge. Sampling time is $\Delta t = 0.05$sec; Nyquist frequency is 10 Hz. Perforated plate diameter to momentum thickness ratio is $D/\theta = 0.85$ and impingement length to momentum thickness ratio is $L/\theta = 22.25$

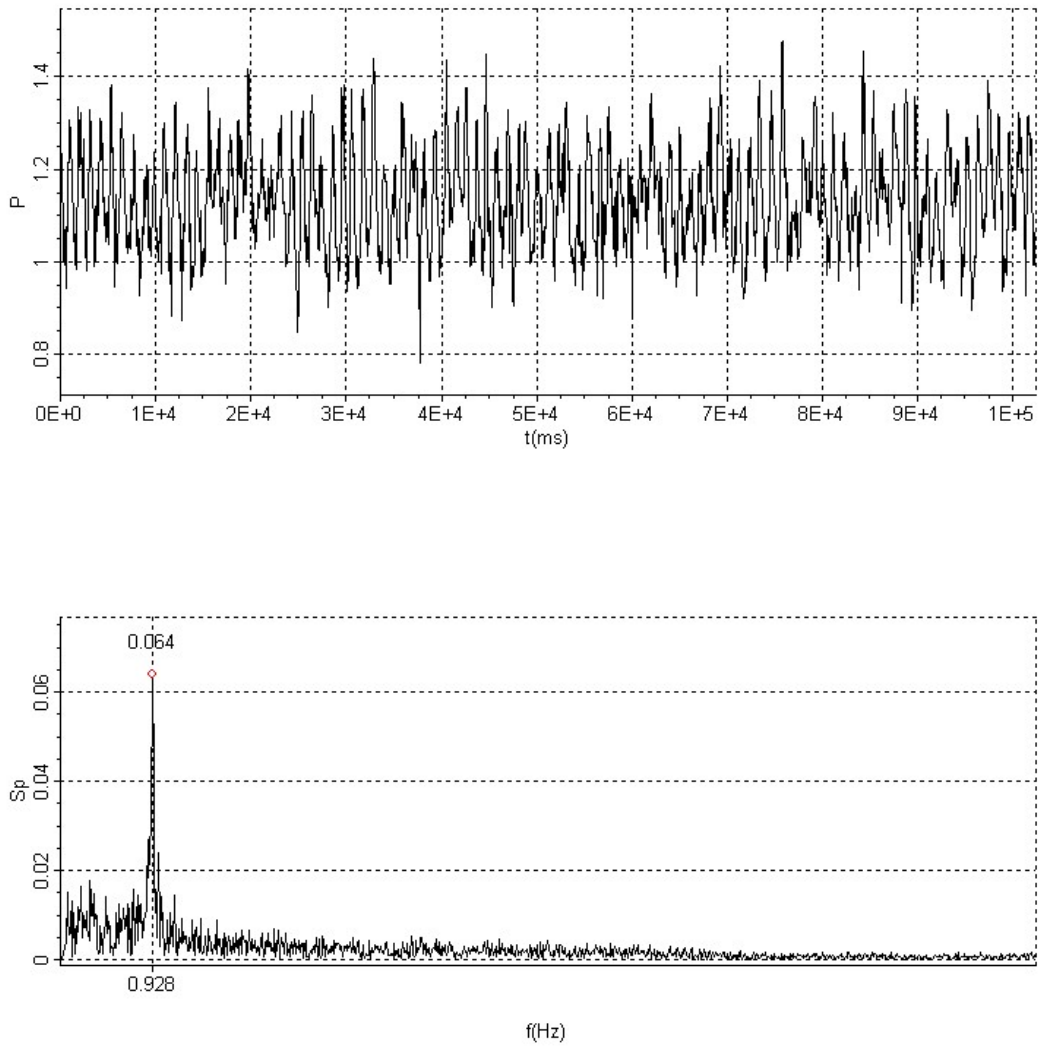

Figure 4.2.8. Time trace and spectrum of pressure fluctuation at tip of impingement edge. Sampling time is $\Delta t = 0.05$sec; Nyquist frequency is 10 Hz. Perforated plate diameter to momentum thickness ratio is $D/\theta = 1.7$ and impingement length to momentum thickness ratio is $L/\theta = 17.75$

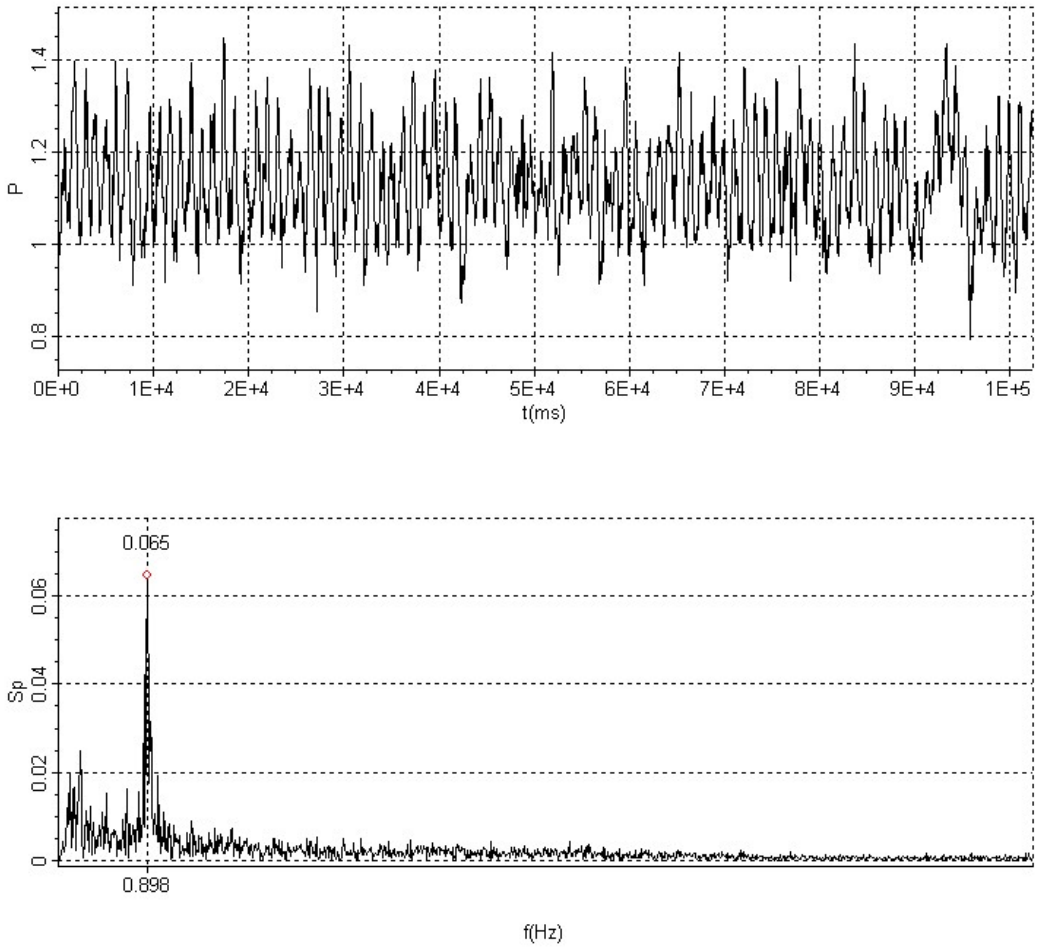

Figure 4.2.9. Time trace and spectrum of pressure fluctuation at tip of impingement edge. Sampling time is $\Delta t = 0.05$sec; Nyquist frequency is 10 Hz. Perforated plate diameter to momentum thickness ratio is $D/\theta = 1.7$ and impingement length to momentum thickness ratio is $L/\theta = 18.5$

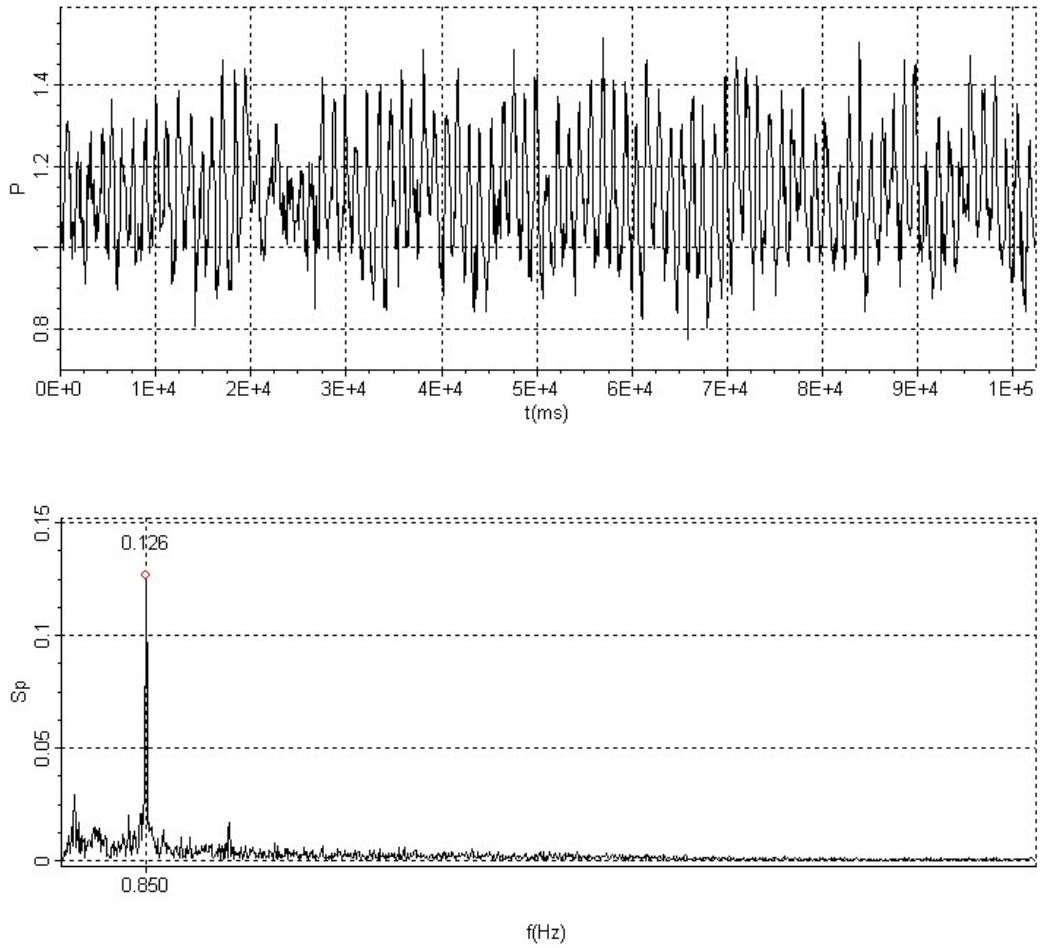

Figure 4.2.10. Time trace and spectrum of pressure fluctuation at tip of impingement edge. Sampling time is $\Delta t = 0.05$sec; Nyquist frequency is 10 Hz. Perforated plate diameter to momentum thickness ratio is $D/\theta = 1.7$ and impingement length to momentum thickness ratio is $L/\theta = 19.25$

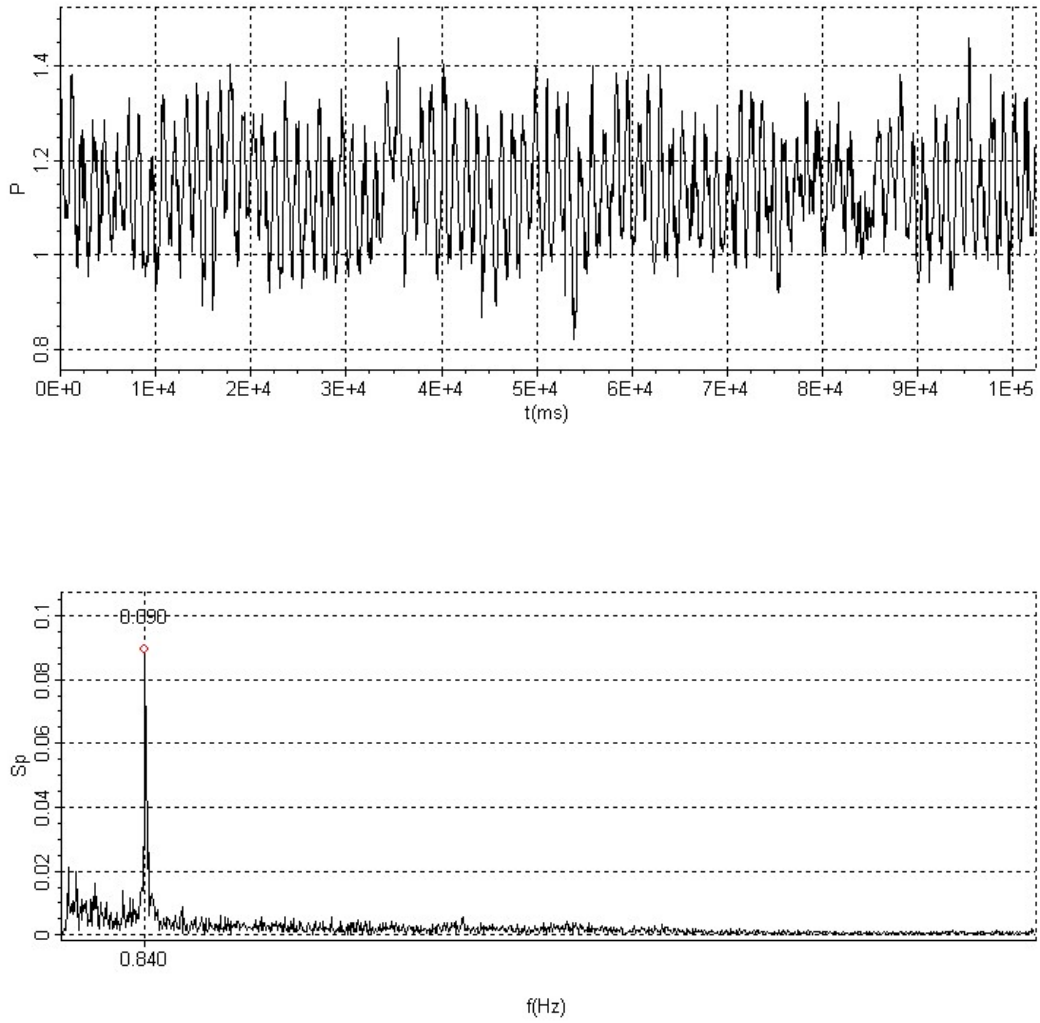

Figure 4.2.11. Time trace and spectrum of pressure fluctuation at tip of impingement edge. Sampling time is $\Delta t = 0.05$sec; Nyquist frequency is 10 Hz. Perforated plate diameter to momentum thickness ratio is $D/\theta = 1.7$ and impingement length to momentum thickness ratio is $L/\theta = 20$

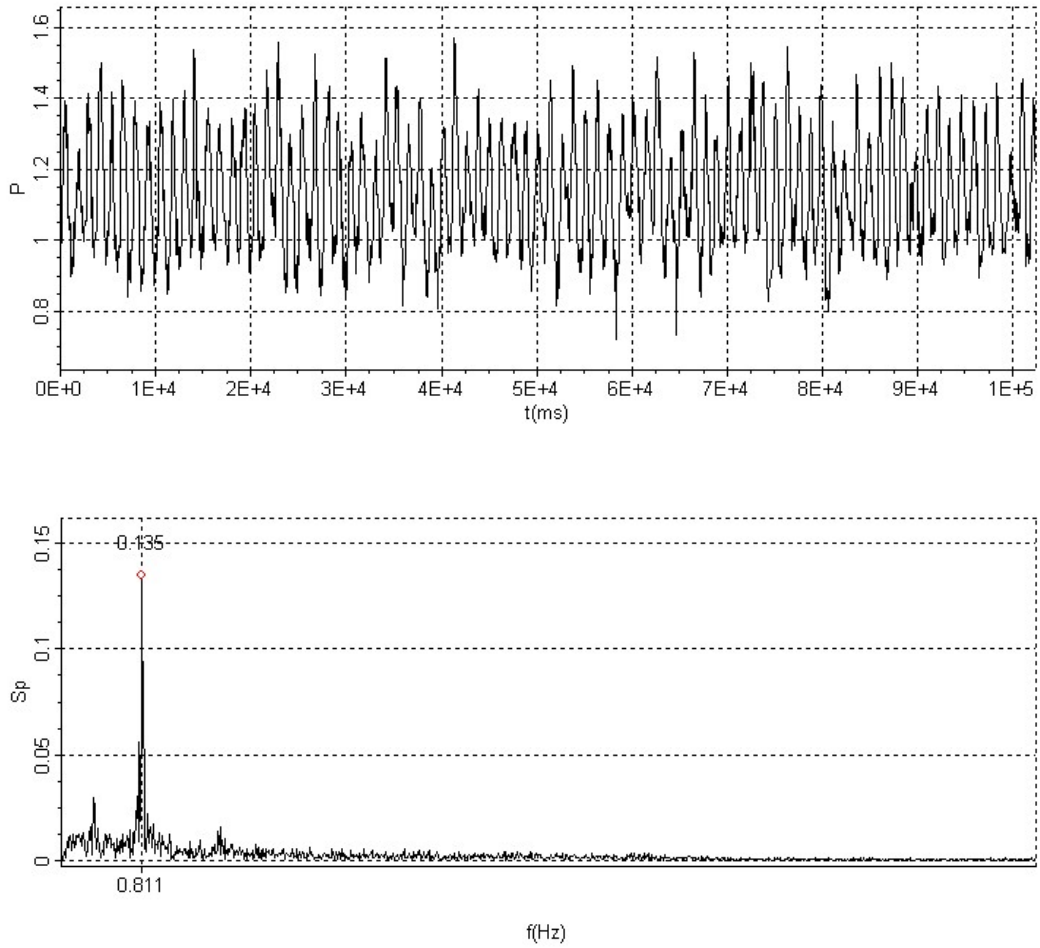

Figure 4.2.12. Time trace and spectrum of pressure fluctuation at tip of impingement edge. Sampling time is $\Delta t = 0.05$sec; Nyquist frequency is 10 Hz. Perforated plate diameter to momentum thickness ratio is $D/\theta = 1.7$ and impingement length to momentum thickness ratio is $L/\theta = 20.75$

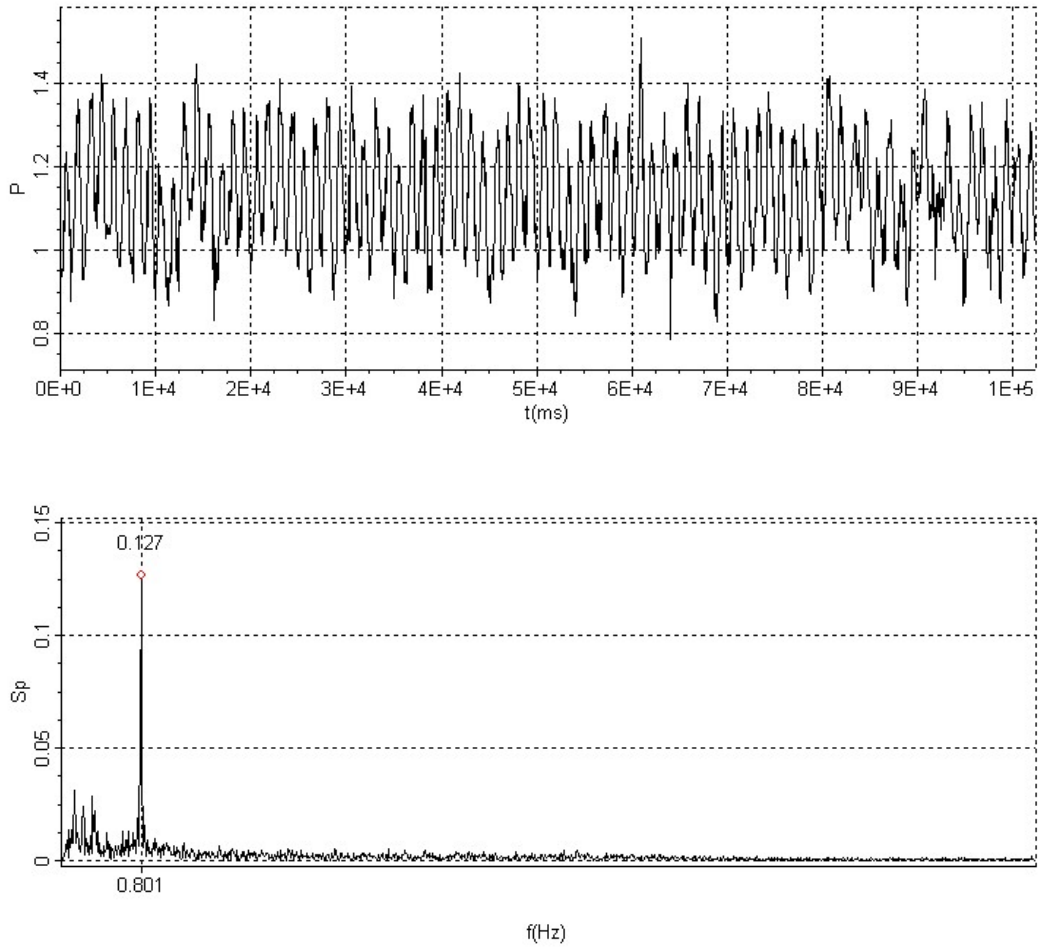

Figure 4.2.13. Time trace and spectrum of pressure fluctuation at tip of impingement edge. Sampling time is $\Delta t = 0.05$sec; Nyquist frequency is 10 Hz. Perforated plate diameter to momentum thickness ratio is $D/\theta = 1.7$ and impingement length to momentum thickness ratio is $L/\theta = 21.5$

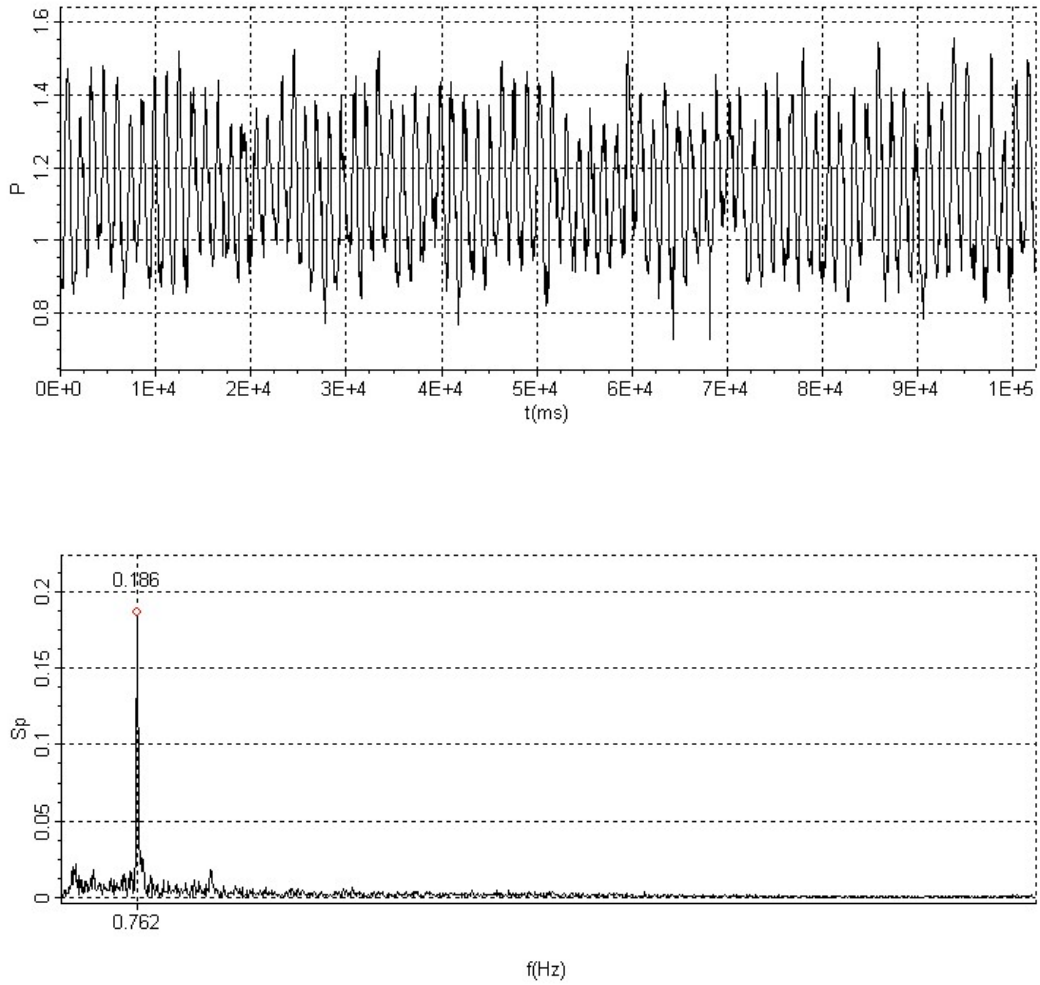

Figure 4.2.14. Time trace and spectrum of pressure fluctuation at tip of impingement edge. Sampling time is $\Delta t = 0.05$sec; Nyquist frequency is 10 Hz. Perforated plate diameter to momentum thickness ratio is $D/\theta = 1.7$ and impingement length to momentum thickness ratio is $L/\theta = 22.25$

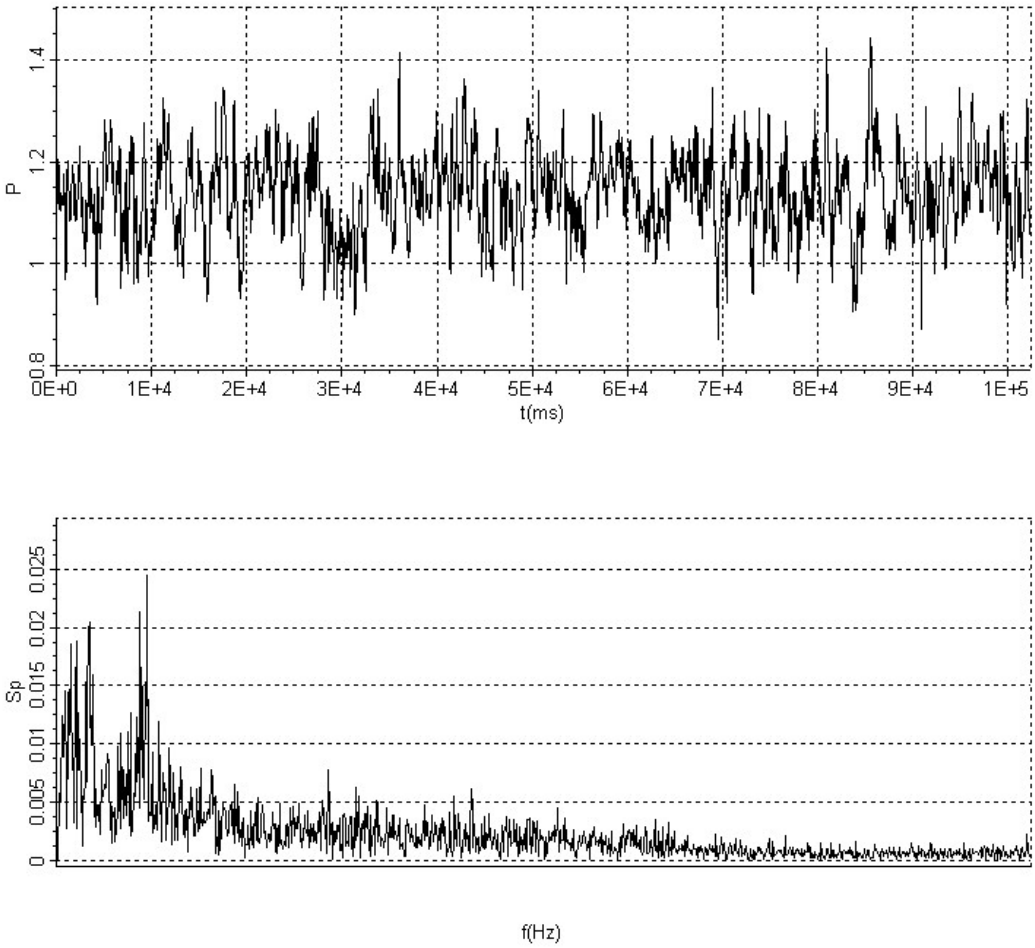

Figure 4.2.15. Time trace and spectrum of pressure fluctuation at tip of impingement edge. Sampling time is $\Delta t = 0.05$sec; Nyquist frequency is 10 Hz. Perforated plate diameter to momentum thickness ratio is $D/\theta = 2.54$ and impingement length to momentum thickness ratio is $L/\theta = 17.75$

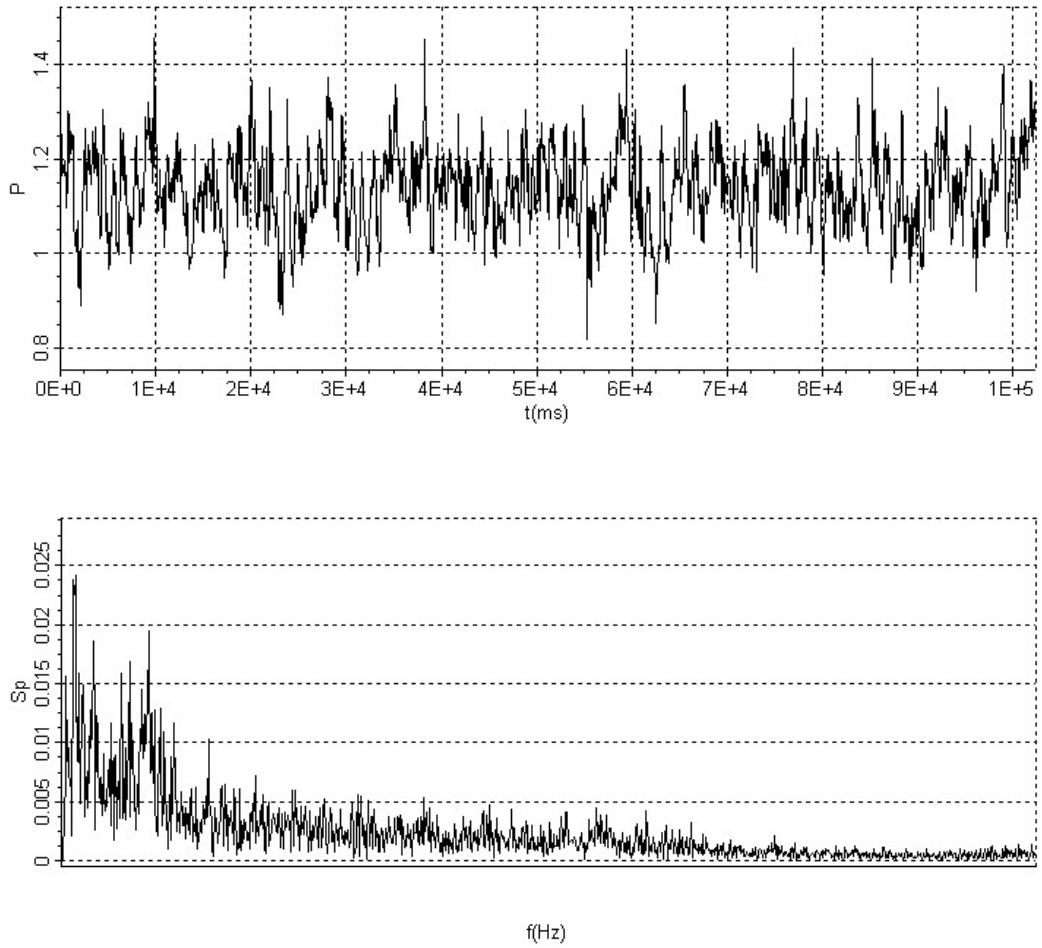

Figure 4.2.16. Time trace and spectrum of pressure fluctuation at tip of impingement edge. Sampling time is $\Delta t = 0.05$sec; Nyquist frequency is 10 Hz. Perforated plate diameter to momentum thickness ratio is $D/\theta = 2.54$ and impingement length to momentum thickness ratio is $L/\theta = 18.5$

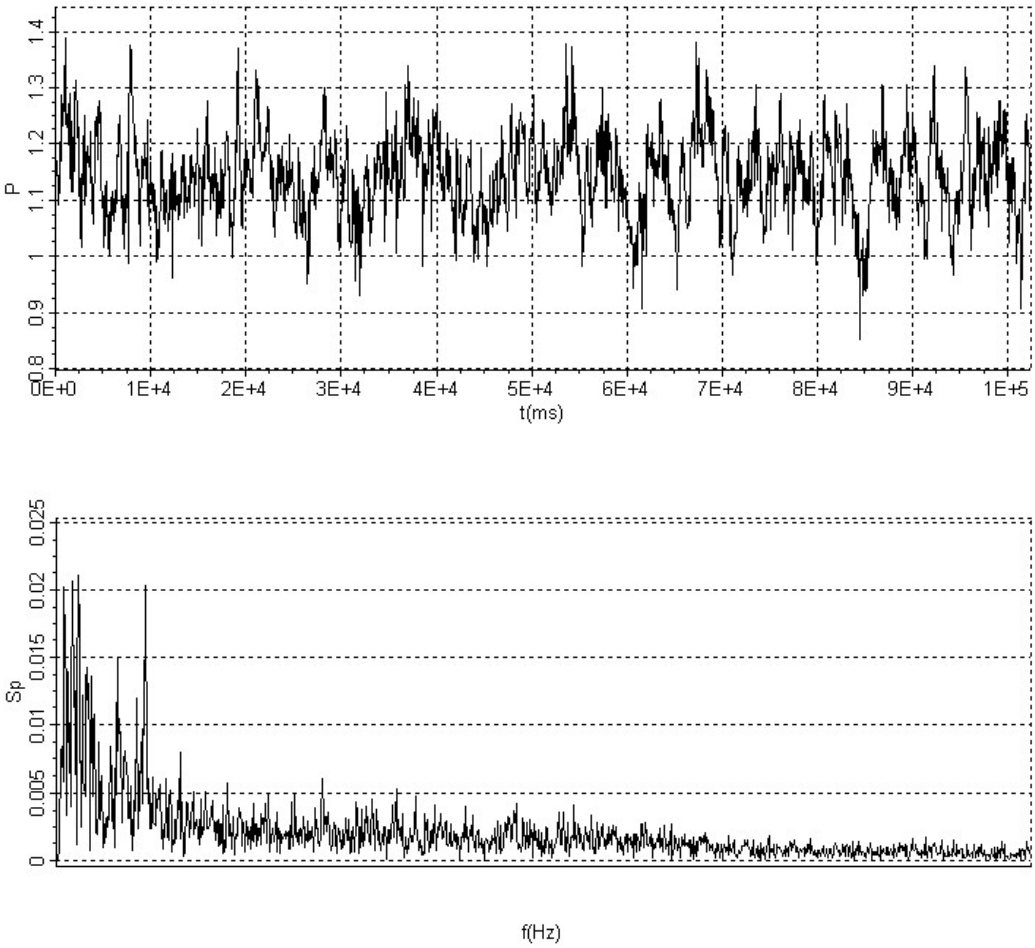

Figure 4.2.17. Time trace and spectrum of pressure fluctuation at tip of impingement edge. Sampling time is $\Delta t = 0.05$sec; Nyquist frequency is 10 Hz. Perforated plate diameter to momentum thickness ratio is $D/\theta = 2.54$ and impingement length to momentum thickness ratio is $L/\theta = 19.25$

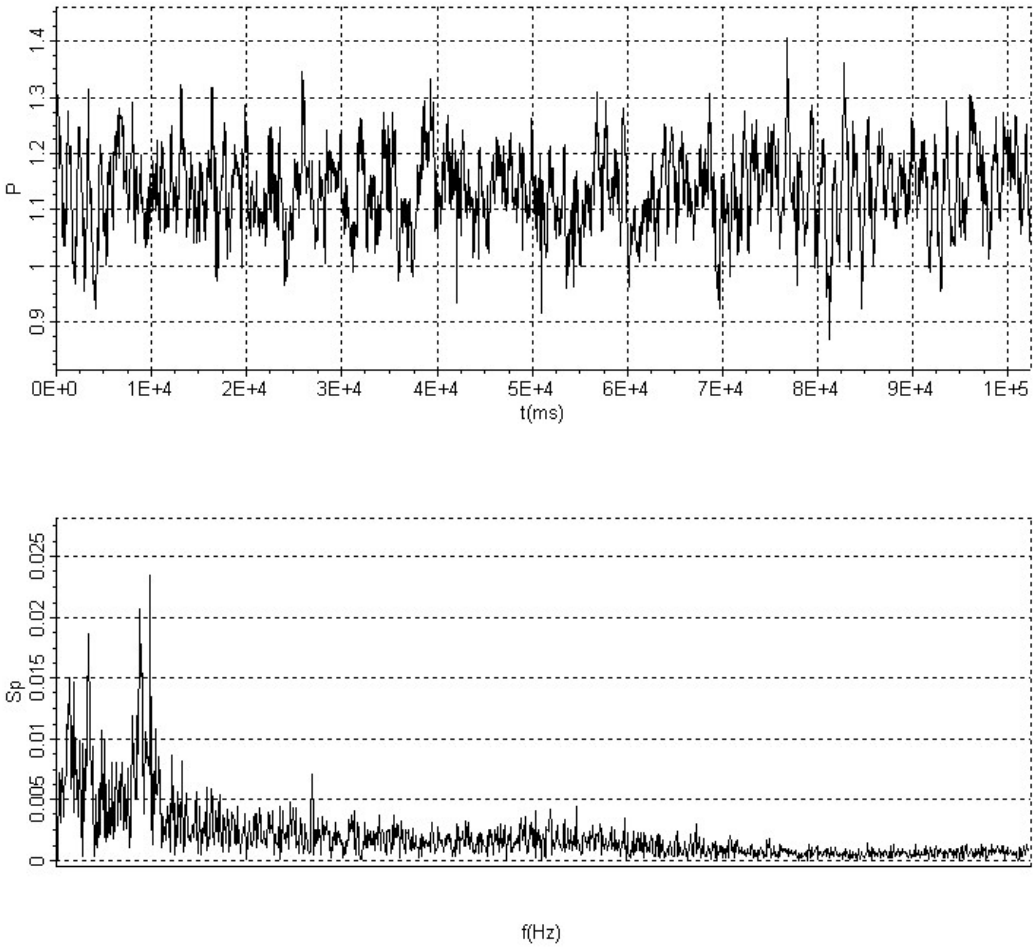

Figure 4.2.18. Time trace and spectrum of pressure fluctuation at tip of impingement edge. Sampling time is $\Delta t = 0.05$sec; Nyquist frequency is 10 Hz. Perforated plate diameter to momentum thickness ratio is $D/\theta = 2.54$ and impingement length to momentum thickness ratio is $L/\theta = 20.0$

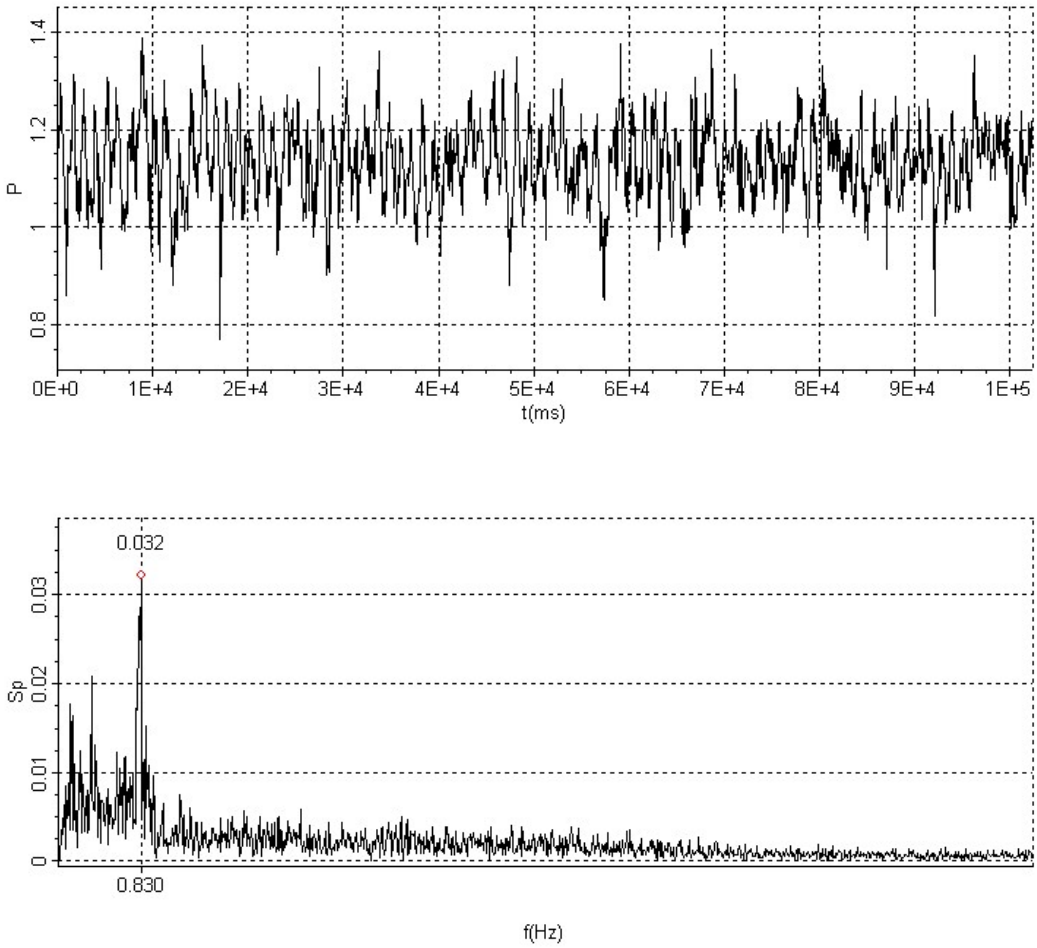

Figure 4.2.19. Time trace and spectrum of pressure fluctuation at tip of impingement edge. Sampling time is $\Delta t = 0.05$sec; Nyquist frequency is 10 Hz. Perforated plate diameter to momentum thickness ratio is $D/\theta = 2.54$ and impingement length to momentum thickness ratio is $L/\theta = 20.75$

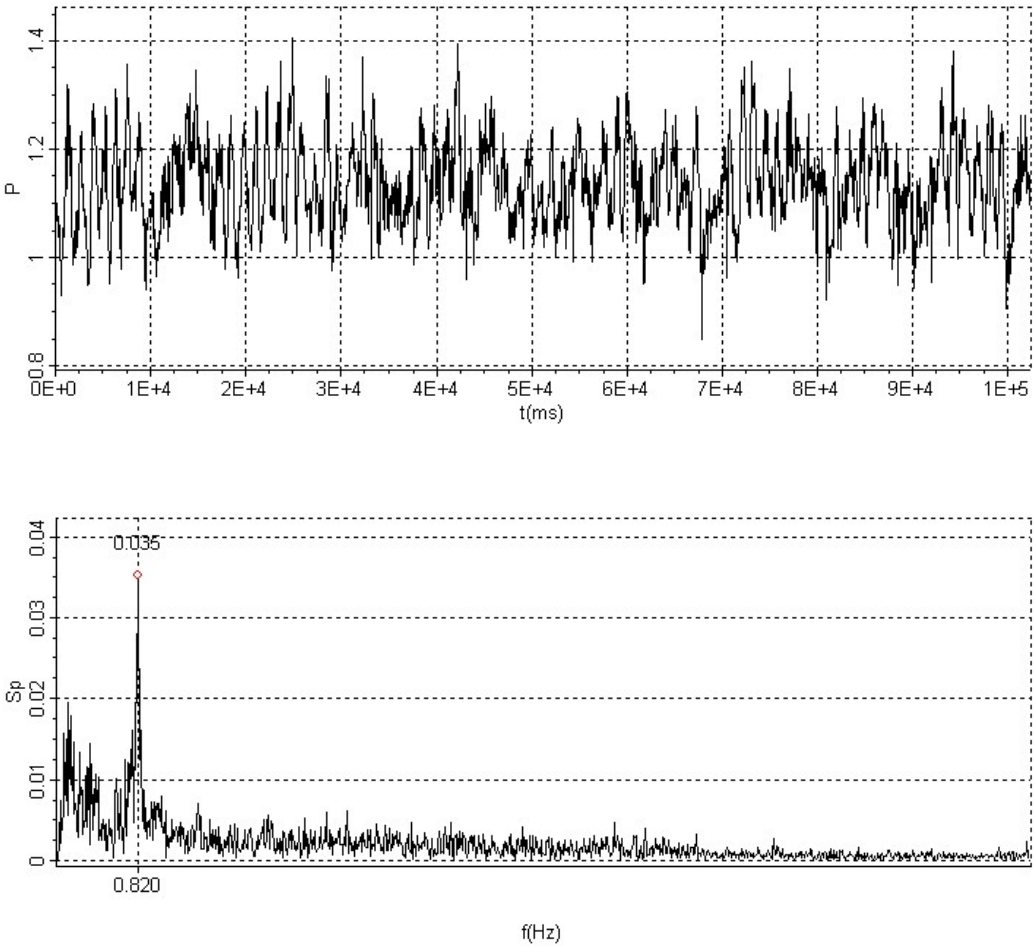

Figure 4.2.20. Time trace and spectrum of pressure fluctuation at tip of impingement edge. Sampling time is $\Delta t = 0.05$sec; Nyquist frequency is 10 Hz. Perforated plate diameter to momentum thickness ratio is $D/\theta = 2.54$ and impingement length to momentum thickness ratio is $L/\theta = 21.5$

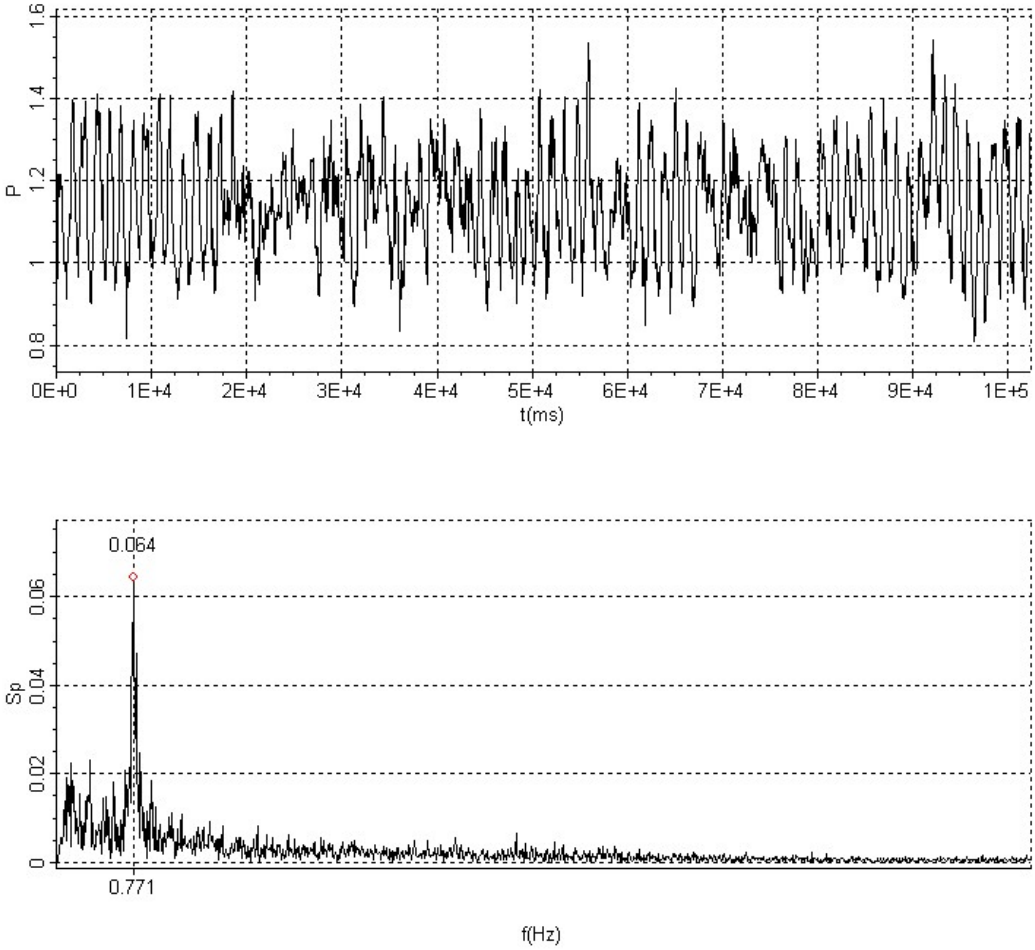

Figure 4.2.21. Time trace and spectrum of pressure fluctuation at tip of impingement edge. Sampling time is $\Delta t = 0.05$sec; Nyquist frequency is 10 Hz. Perforated plate diameter to momentum thickness ratio is $D/\theta = 2.54$ and impingement length to momentum thickness ratio is $L/\theta = 22.25$

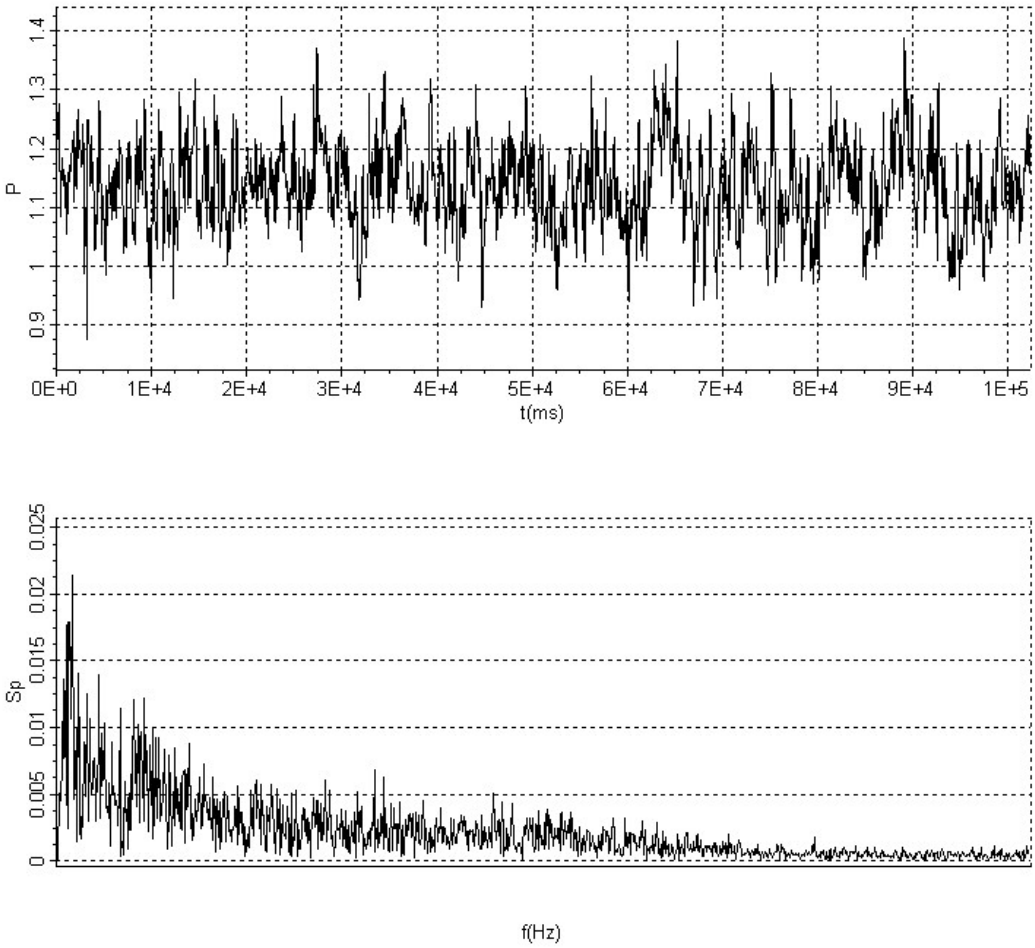

Figure 4.2.22. Time trace and spectrum of pressure fluctuation at tip of impingement edge. Sampling time is $\Delta t = 0.05$sec; Nyquist frequency is 10 Hz. Perforated plate diameter to momentum thickness ratio is $D/\theta = 3.4$ and impingement length to momentum thickness ratio is $L/\theta = 17.75$

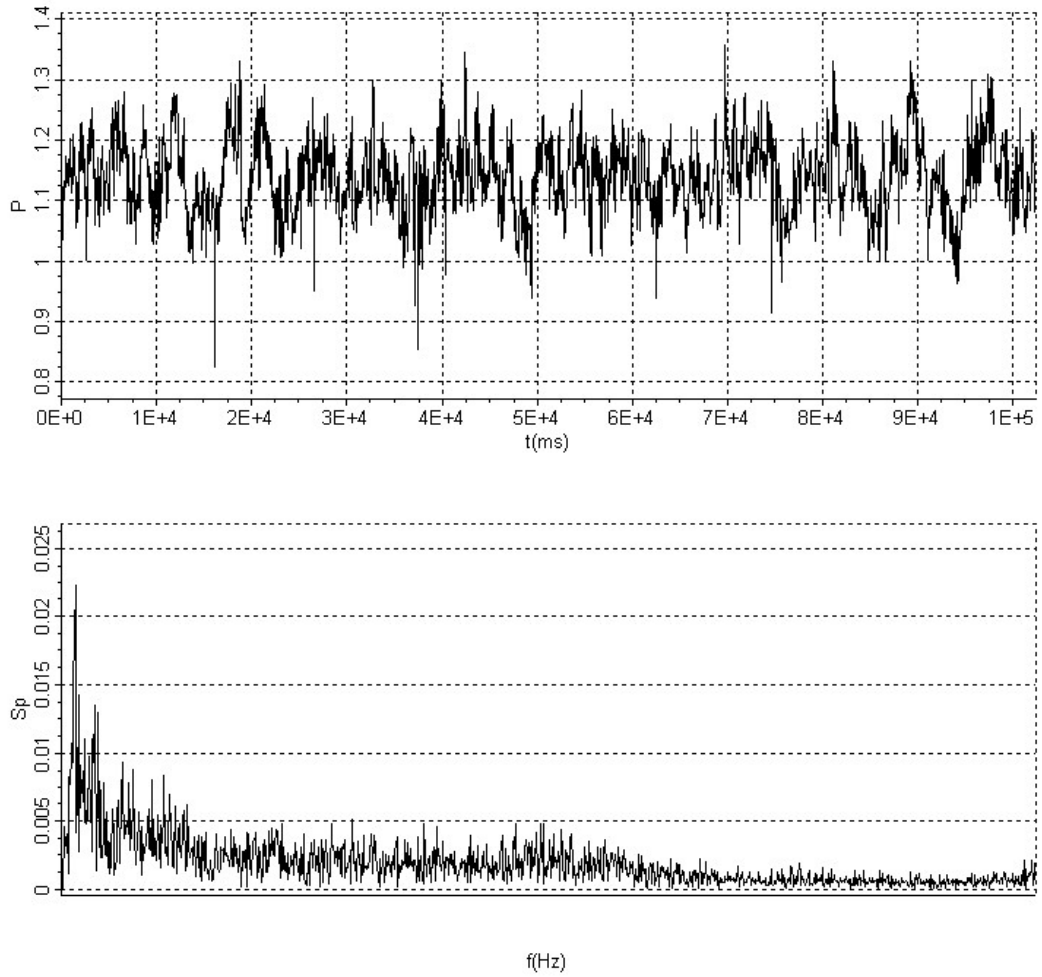

Figure 4.2.23. Time trace and spectrum of pressure fluctuation at tip of impingement edge. Sampling time is $\Delta t = 0.05$sec; Nyquist frequency is 10 Hz. Perforated plate diameter to momentum thickness ratio is $D/\theta = 3.4$ and impingement length to momentum thickness ratio is $L/\theta = 18.5$

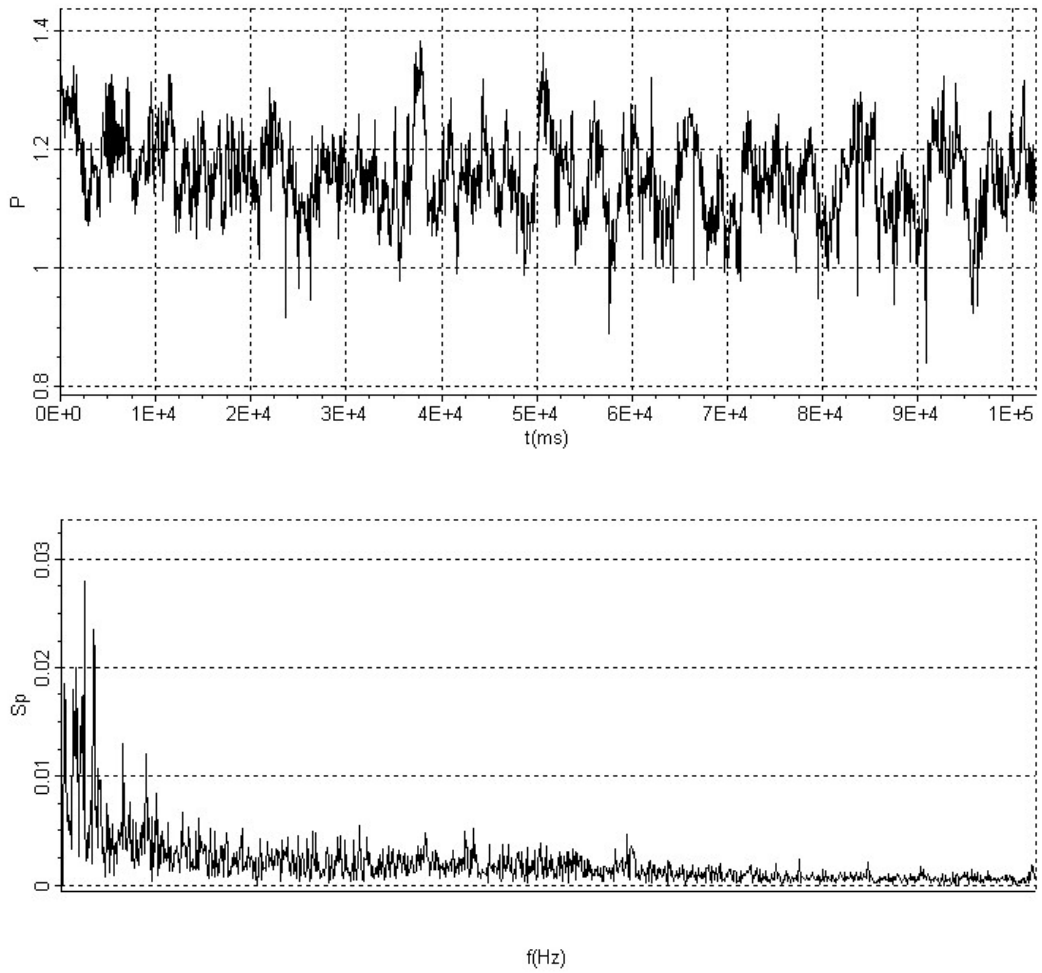

Figure 4.2.24. Time trace and spectrum of pressure fluctuation at tip of impingement edge. Sampling time is $\Delta t = 0.05$sec; Nyquist frequency is 10 Hz. Perforated plate diameter to momentum thickness ratio is $D/\theta = 3.4$ and impingement length to momentum thickness ratio is $L/\theta = 19.25$

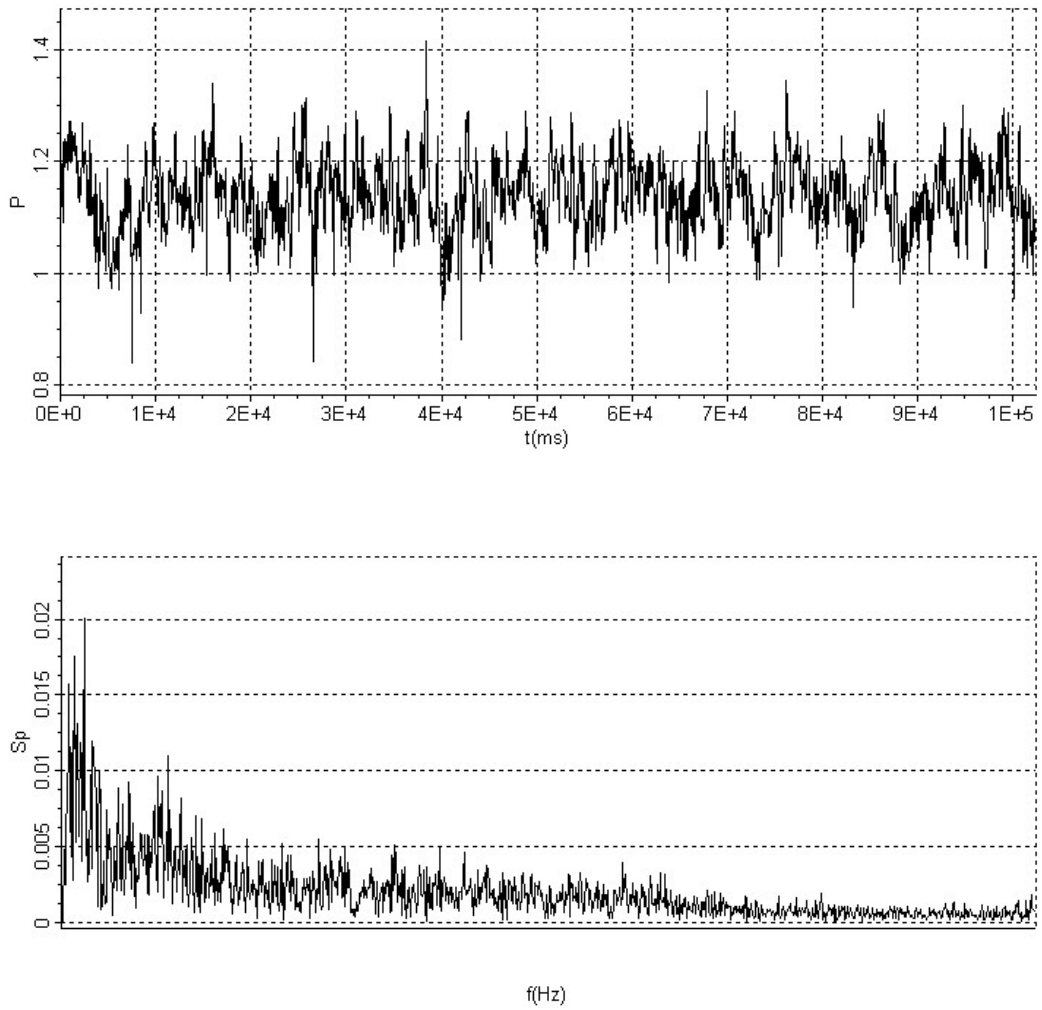

Figure 4.2.25. Time trace and spectrum of pressure fluctuation at tip of impingement edge. Sampling time is $\Delta t = 0.05$sec; Nyquist frequency is 10 Hz. Perforated plate diameter to momentum thickness ratio is $D/\theta = 3.4$ and impingement length to momentum thickness ratio is $L/\theta = 20.0$

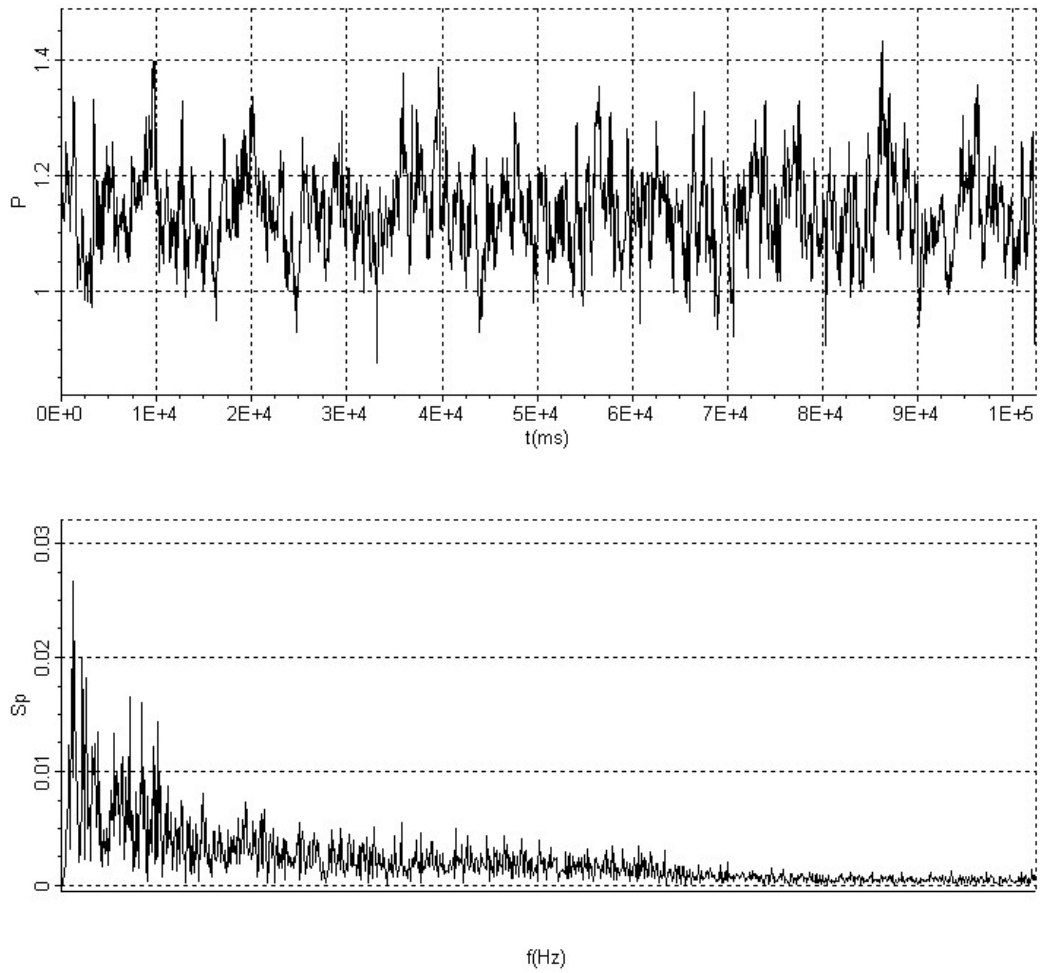

Figure 4.2.26. Time trace and spectrum of pressure fluctuation at tip of impingement edge. Sampling time is $\Delta t = 0.05$sec; Nyquist frequency is 10 Hz. Perforated plate diameter to momentum thickness ratio is $D/\theta = 3.4$ and impingement length to momentum thickness ratio is $L/\theta = 20.75$

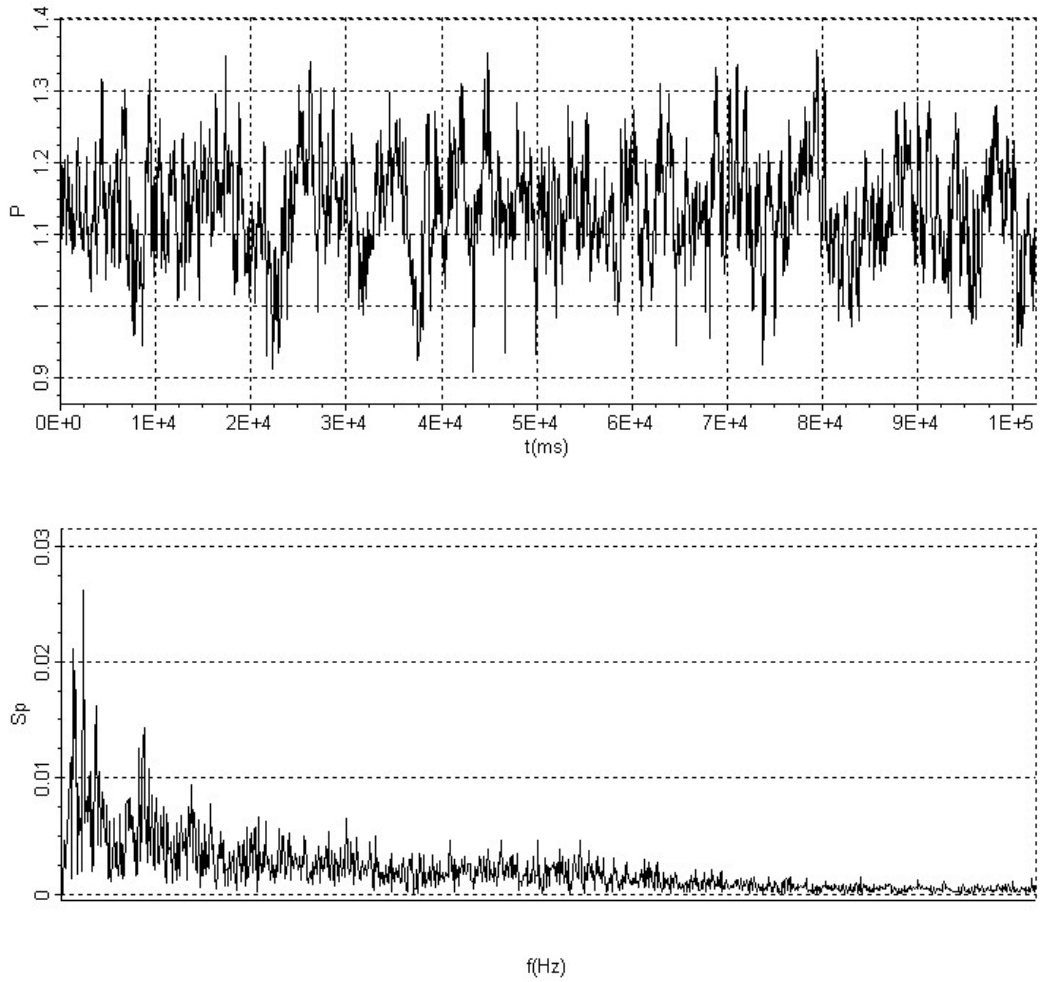

Figure 4.2.27. Time trace and spectrum of pressure fluctuation at tip of impingement edge. Sampling time is $\Delta t = 0.05$sec; Nyquist frequency is 10 Hz. Perforated plate diameter to momentum thickness ratio is $D/\theta = 3.4$ and impingement length to momentum thickness ratio is $L/\theta = 21.5$

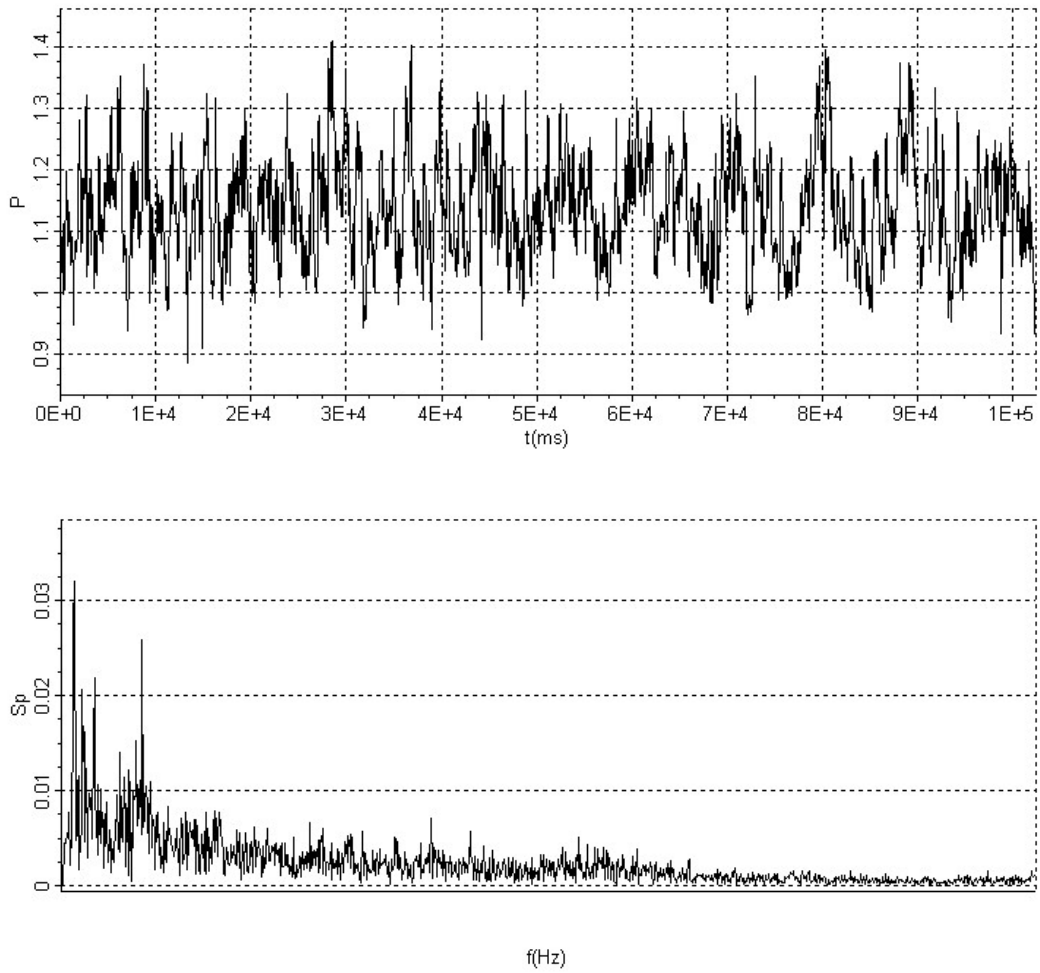

Figure 4.2.28. Time trace and spectrum of pressure fluctuation at tip of impingement edge. Sampling time is $\Delta t = 0.05$sec; Nyquist frequency is 10 Hz. Perforated plate diameter to momentum thickness ratio is $D/\theta = 3.4$ and impingement length to momentum thickness ratio is $L/\theta = 22.25$

4.3. Attenuation of Self-Excited Oscillations in Flow Past a Perforated Plate Via Three-Dimensional Surface Elements

In absence of the three-dimensional surface elements, a well-defined front of the unstable oscillation propagates along the surface of the plate. In presence of an appropriate surface element, the front is no longer detectable, and instantaneous and averaged defects of the streamwise velocity and surface-normal vorticity exist along the span of the plate. The magnitudes and spanwise wavelengths of these defects are directly related to the extent of attenuation of the oscillation. Since the magnitudes of these defects decay significantly with distance along the plate, the most effective attenuation typically occurs for plate lengths less than or equal to a critical length.

It is known that flow past a perforated plate can give rise to purely hydrodynamic, self-sustained oscillations, which have a wavelength of the order of the plate length. The present part of this investigation demonstrates that these oscillations can be effectively attenuated by three-dimensional surface elements in the form of vortex generators.

An appropriate measure of the degree of attenuation is a reduction in the magnitude of the coherent component of the fluctuating pressure. For all cases, even in presence of effective attenuation, a low magnitude spectral peak at the frequency of the inherent oscillation is still discernible; it may be either sharp or broadband, and is indicative of the robust nature of the self-sustained oscillation.

4.3.1. Alteration of Flow Structure due to Three-Dimensional Surface Elements

Although three-dimensional surface elements, such as vortex generators, have not been employed for the type of flow instability addressed herein, investigations of such elements or generators for attenuation of self-excited oscillations in related configurations can provide guidance. They have been effectively used for alterations of the structure of separated flows of finite streamwise extent, in absence of a perforated or slotted plate along the cavity opening. Keller and Escudier (1979) demonstrated the attenuation of self-sustained oscillations of flow past a cavity, with

emphasis on the effect of incidence angle of the generators. Karadogan and Rockwell (1983) characterized the effect of dimensionless height and wavelength of vortex generators for attenuation of the self-sustained oscillations of an axisymmetric jet flow through a cavity.

4.3.2. Oscillations in Absence of Three-Dimensional Surface Element

Figure 4.3.1 shows pressure spectra and images of the instantaneous flow structure along the span of the plate in absence of a three-dimensional surface element. It serves as a reference case for the mitigation of self-sustained oscillations, which is addressed in subsequent figures. Images were taken over a square field of view with dimensions 92.63 mm × 92.63 mm. The pressure spectra $S_p(f)$ shown at the top of Figure 3 indicate sharply defined peaks for the range of cavity length extending from $L/\theta = 17.0$ to 21.5. Correspondingly, the sequence of instantaneous images of streamwise velocity u is given in the cinema sequence $N = 0$, 2, 4 and 6. Darker regions correspond to larger magnitude vectors, and lighter regions to relatively small magnitude vectors. It is evident that a front, defined as the interface between regions of high (light) and low (dark) regions of u, propagates from left to right. In the section that follows, the consequences of the three-dimensional surface elements on both the pressure spectra and the surface patterns of Figure 4.3.1 will be addressed. Images in Figures 4.3.2 to 4.3.6 were taken in a field of view with dimensions 86.83 mm × 137.48 mm.

4.3.3. Attenuation of Self-Sustained Oscillations via Three-Dimensional Surface Elements

4.3.3.1. Pressure Spectra and Patterns of Instantaneous Velocity

The effect of the three-dimensional surface element *A* is shown in Figure 4.3.2. It involves, in essence, a series of triangular elements, all having the same angle of inclination (see Figure 3.8). The set of pressure spectra shown at the top of Figure 4 indicate that, in all cases, the amplitude of the spectral peak is smaller than the corresponding reference values of Figure 4.3.1. Substantial attenuation occurs up to $L/\theta = 20$ and, at this value, the time trace of the pressure signal intermittently shows regions of both ordered and less organized fluctuations. At the largest value of $L/\theta = 21.5$, the magnitude of the peak is sharply defined, but still is less than half the reference value given in Figure 4.3.1.

The physical basis for mitigation of the spectral peaks of Figure 4.3.2 is given in the cinema sequence of instantaneous streamwise velocity u at the bottom of Figure 4. Regions of significant velocity defects (light colored regions) form alternately with regions of higher velocity (dark colored regions) across the span of the plate. Furthermore, adjacent regions of larger velocity are connected as, for example, evident at the middle of the image $N = 0$ in Figure 4.3.2. Viewing the patterns at all values of N at the bottom of Figure 4.3.2, then comparing with the patterns of Figure 4.3.1 in absence of a three-dimensional surface element, it is evident that Figure 4.3.2 does not show a clearly defined front that propagates from left to right.

The spectra and velocity patterns of Figure 4.3.3 correspond to a three-dimensional element *B* that is geometrically similar to the element of Figure 4.3.2. As indicated in the overview of Figure 3.8, however, this element has a height h/θ that is more than a factor of three smaller than the element *A* given in Figures 3.8 and 4.3.2. The spectra at the top of Figure 4.3.3 indicate that this configuration is, in most cases, marginally effective. At the largest value of $L/\theta = 21.5$, the attenuation

of the peak is minimal. Furthermore, the trace of the pressure signal $p(t)$ at $L/\theta = 20$ indicates a reasonably organized oscillation over the entire time interval.

The corresponding patterns of instantaneous streamwise velocity u of Figure 4.3.3 show regions of lower velocity interspersed in an irregular fashion among regions of higher (dark) velocity, but the well-defined longitudinal regions of lower and higher velocity evident in the images of Figure 4.3.2 are not present. Furthermore, viewing together all of the images at values of $N = 0$ through 6 in Figure 4.3.2, it is possible, in an approximate sense, to witness the propagation, from left to right, of the highly irregular front. This front, however, is not as well defined as in the reference case of Figure 4.3.1 in absence of the three-dimensional element.

A fundamentally different three-dimensional element, geometry C, is represented in Figure 4.3.4. Generally speaking, the spectra shown at the top of Figure 6 indicate reasonable reduction of the predominant spectral peak. For the largest plate length $L/\theta = 21.5$, the attenuation is less effective. Nevertheless, at this value of L/θ, the amplitude of the spectral peak is of the order of one-third the value in absence of the three-dimensional element (see Figure 4.3.1).

This attenuation is accompanied by the appearance of a well-defined, longitudinal band of velocity defect (light region) in all of the images of instantaneous streamwise velocity u, i.e., images $N = 0$ through $N = 6$ of Figure 4.3.4. The persistence of this band of low velocity over the entire streamwise extent of the image is similar in form to the case shown in Figure 4.3.2, for which effective attenuation was also achieved. Furthermore, the lack of a well-defined front, of the type shown in Figure 4.3.1, is also apparent in the patterns of velocity of Figure 4.3.4. Again, this feature is in accord with that observed in conjunction with the attenuation concept of Figure 4.3.2.

The same overall form of the three-dimensional surface element of Figure 4.3.2, but with successively decreasing values of dimensionless height h/θ and wavelength Λ/θ, are represented by the configurations D and E respectively of Figures 4.3.5 and 4.3.6. As indicated by the corresponding spectra therein, element D of Figure 4.3.5 is essentially as effective as the element C in Figure 4.3.6 in reducing peak amplitudes of the spectra over the given range of L/θ. On the other

hand, element *E* of Figure 4.3.6 is not as effective as configuration *C* of Figure 4.3.4 for the lowest values of L/θ = 17.0 and 18.5. On the other hand, it is remarkably effective at longer values of L/θ = 20.0 and 21.5. This observation may, at least in part, be explained by the patterns of instantaneous streamwise velocity *u* at the bottom of Figure 4.3.6. Consider, for example, the image *N* = 6. At the left edge of this image, several distinct bands of high velocity (dark regions) are evident. On the other hand, towards the middle of the image *N* = 6, the top two bands appear to coalesce, or merge together, to form a single band. The consequence is that, in the right half of the image, only two distinct high velocity (dark region) bands are evident. This larger spanwise spacing may promote more effective attenuation at larger streamwise lengths, as observed for the larger spacing of the low velocity (light regions) of Figure 4.3.4.

Comparison of spectra of the pressure fluctuation at the tip of the edge with and without the three-dimensional surface elements (vortex generators) is shown in Figure 4.3.7 for a representative value of L/θ = 20. It is evident that all configurations *A* through *E* can lead to attenuation, to varying degrees, of the large amplitude spectral peak, at least for this value of L/θ. The element *B* is clearly the least effective of these configurations. As indicated in the foregoing, it is necessary, however, to consider the entire range of L/θ when assessing the performance of these three-dimensional surface elements.

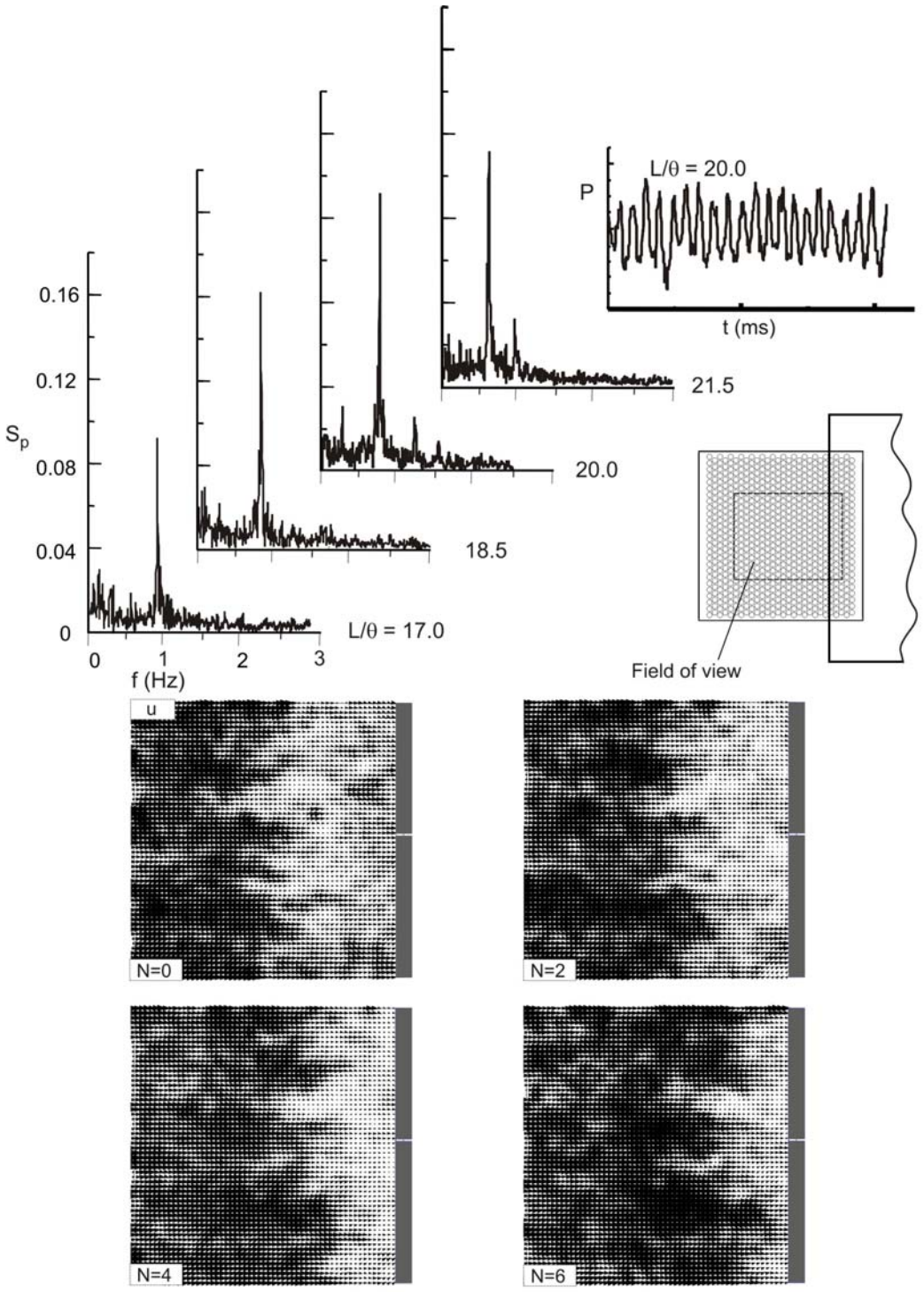

Figure 4.3.1. Spectra of pressure fluctuation S_p at tip of impingement edge without vortex generator for various L/θ values. Images show the patterns of instantaneous vectors of the longitudinal (streamwise) component of velocity u for $L/\theta = 20$. N represents the frame number of cinema sequence.

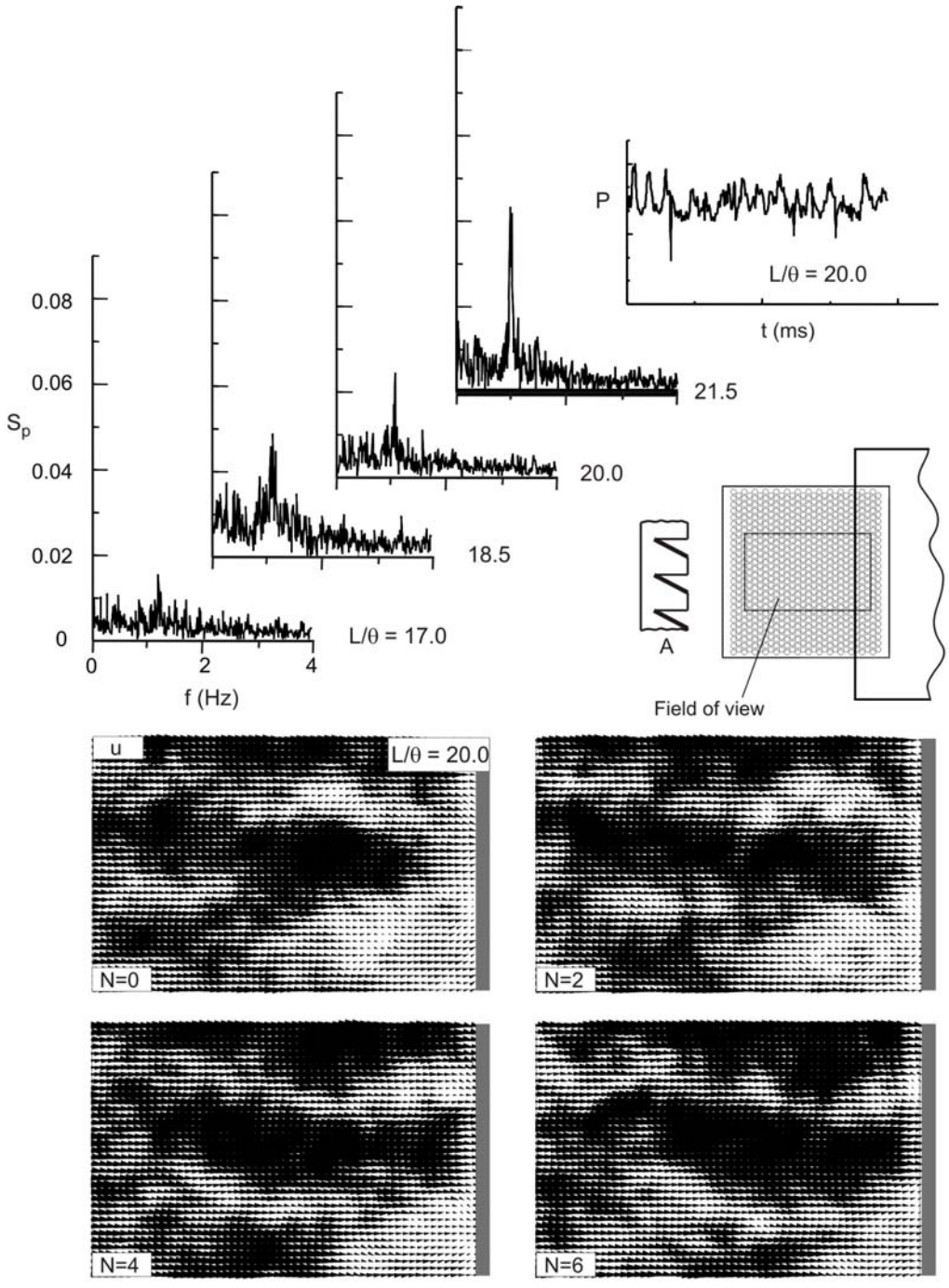

Figure 4.3.2. Spectra of pressure fluctuation S_p at tip of impingement edge for type *A* vortex generator for various L/θ values. Images show the patterns of instantaneous vectors of the longitudinal (streamwise) component of velocity *u* for effective plate length $L/\theta = 20$ and for width of field of view of $w/\theta = 19$, which is the same for all subsequent images. *N* represents the frame number of cinema sequence.

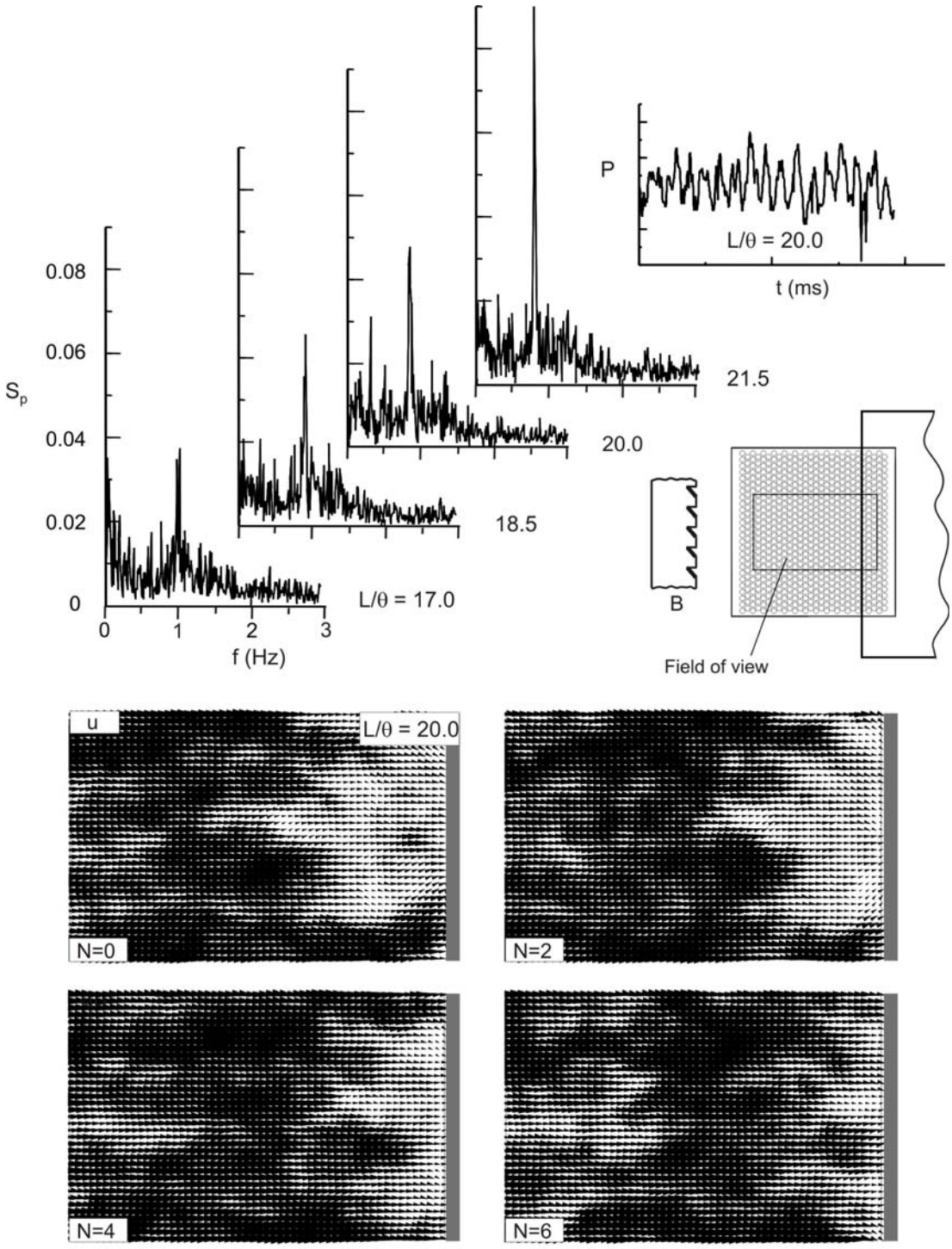

Figure 4.3.3. Spectra of pressure fluctuation S_p at tip of impingement edge for type *B* vortex generator for various L/θ values. Images show the patterns of instantaneous vectors of the longitudinal (streamwise) component of velocity u for $L/\theta = 20$. N represents the frame number of cinema sequence.

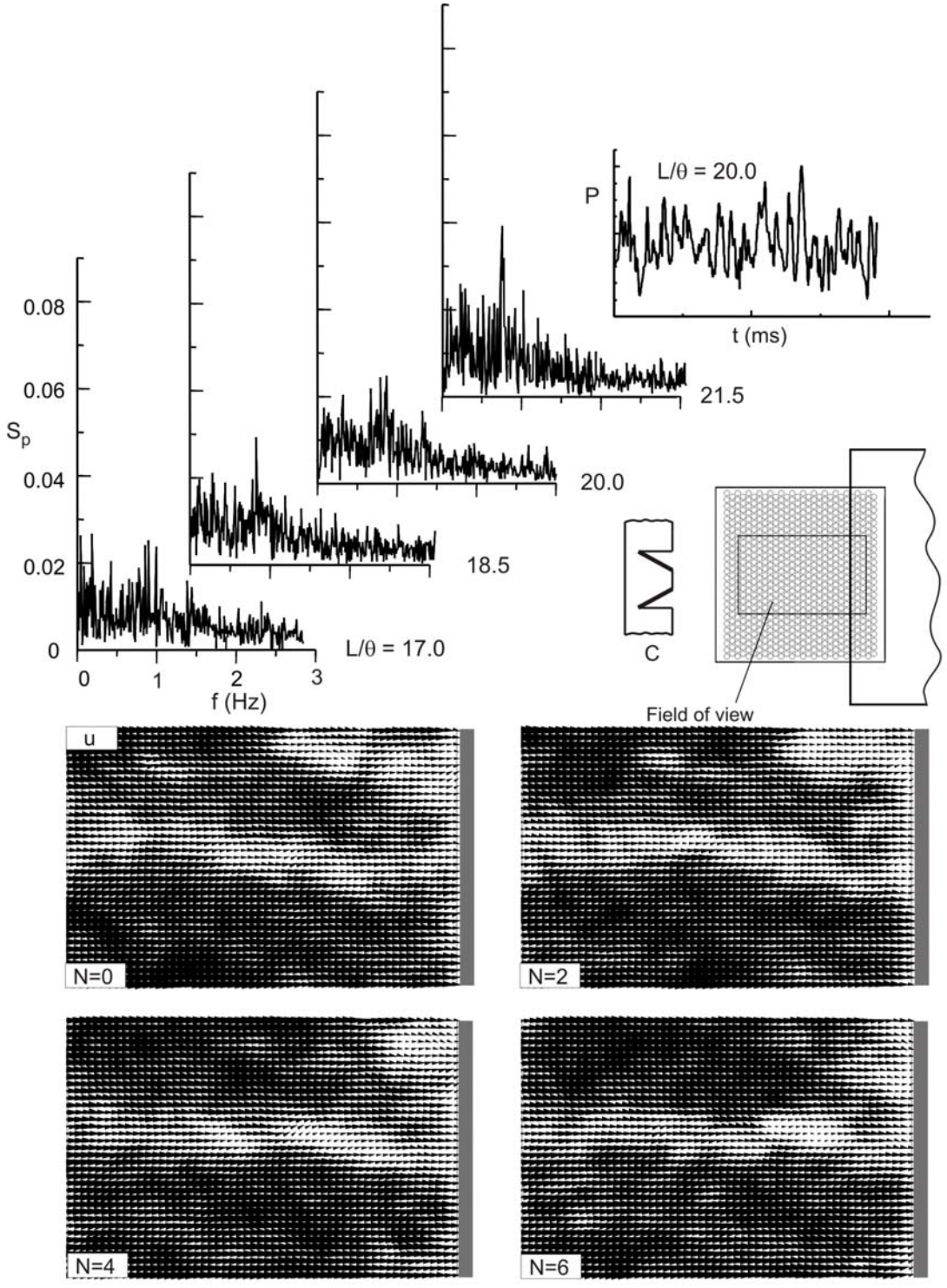

Figure 4.3.4. Spectra of pressure fluctuation S_p at tip of impingement edge for type *C* vortex generator for various L/θ values. Images show the patterns of instantaneous vectors of the longitudinal (streamwise) component of velocity u for $L/\theta = 20$. N represents the frame number of cinema sequence.

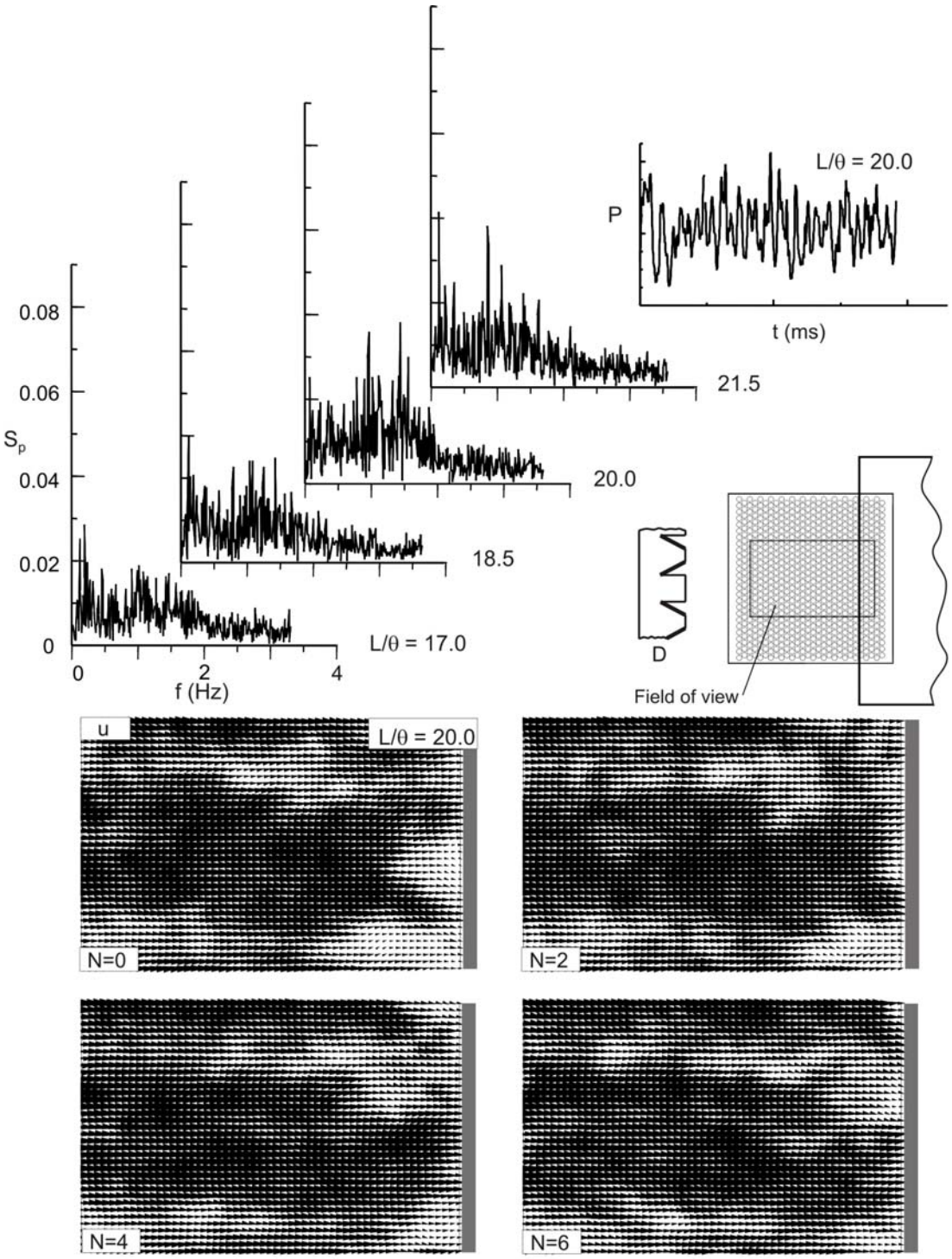

Figure 4.3.5. Spectra of pressure fluctuation S_p at tip of impingement edge for type *D* vortex generator for various L/θ values. Images show the patterns of instantaneous vectors of the longitudinal (streamwise) component of velocity *u* for $L/\theta = 20$. *N* represents the frame number of cinema sequence.

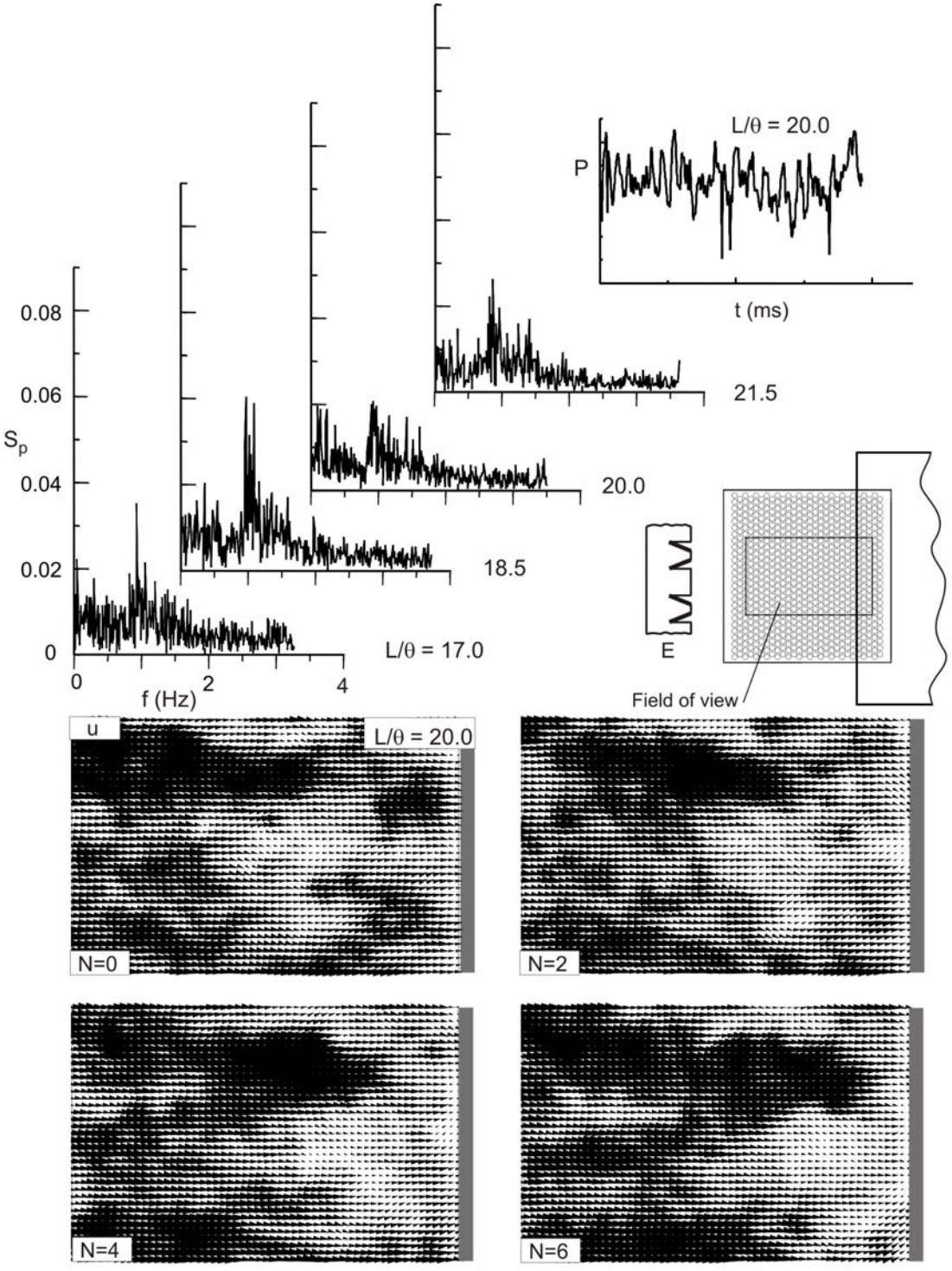

Figure 4.3.6. Spectra of pressure fluctuation S_p at tip of impingement edge for type *E* vortex generator for various L/θ values. Images show the patterns of instantaneous vectors of the longitudinal (streamwise) component of velocity u for $L/\theta = 20$. *N* represents the frame number of cinema sequence.

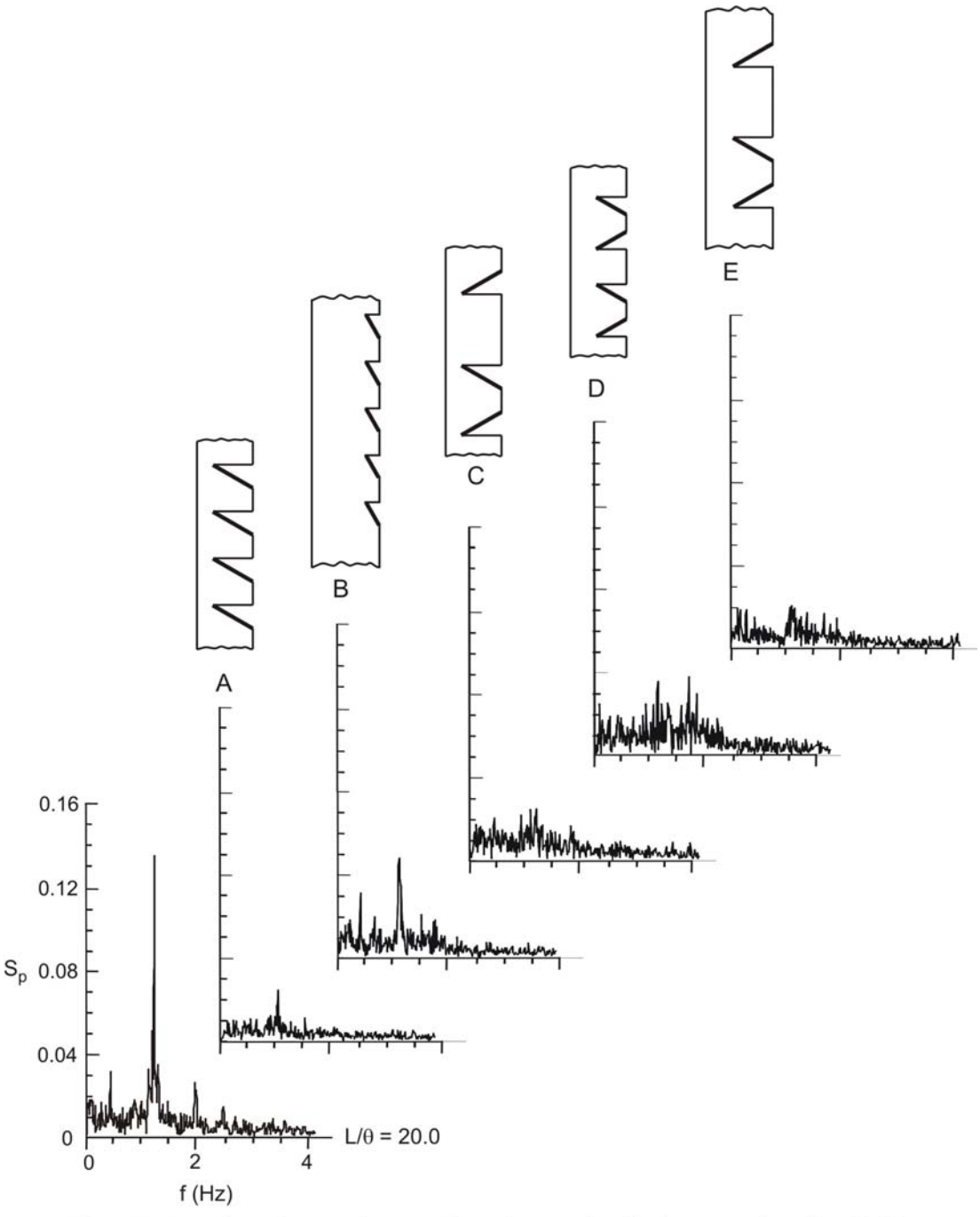

Figure 4.3.7. Comparison of spectra of pressure fluctuation S_p at tip of impingement edge with and without vortex generators for L/θ = 20. The first spectrum corresponds to the case of no vortex generator, while others represent spectra with vortex generators shown in the figure.

4.3.3.2. Velocity Spectra

Spectra S_u of the streamwise velocity fluctuation u were evaluated at various locations in the streamwise and spanwise directions along the perforated plate with and without vortex generators. The spectra S_u on the left hand side of Figure 4.3.8 indicate that the sharply defined peak in the corresponding spectra *Su* without a vortex generator, given at the right of Figure 4.3.8, as well as the peak in the pressure spectra S_p of Figure 4.3.1, is substantially attenuated along the entire streamwise extent of the image. For purposes of reference, the locations of the points of evaluation, 1 through 6, are shown to scale in the field of view, which has a length of 138 mm and a width of 86 mm. A similar type of representation, but across the span of the plate, is shown in Figure 4.3.9. Again, a generally similar level of attenuation occurs over this spatial extent. Taken together, the spectra of Figures 4.3.8 and 4.3.9 show that the organized peak of the oscillation is globally attenuated over the surface of the plate.

4.4. Patterns of Averaged Velocity and Vorticity

Time-averaged patterns of the near-surface velocity and vorticity fields are shown in Figures 4.3.10 through 4.3.12; they are complements to the corresponding instantaneous representations given in the foregoing figures. Figure 4.3.10 shows well-defined bands of lower (light region) and higher (darker region) velocity for the configurations *A, C, D* and *E*, for which effective attenuation was achieved. The distinct feature of the pattern of time-averaged streamwise velocity <*u*> of image *A* is the fact that the light and dark bands are substantially inclined relative to the direction of the freestream velocity. Such inclination does not occur for the patterns of *C*, *D* and *E*. Correspondingly, surface element *A* yielded the least effective attenuation of the configurations represented in Figure 4.3.10; details of this attenuation are shown in Figure 4.3.2.

Patterns of time-averaged velocity vectors at various streamwise locations are shown in Figure 4.3.11 for two representative configurations *C* and *E*. As indicated

in the foregoing Figures 4.3.4 and 4.3.6, both of these configurations yielded effective attenuation. These velocity vectors show two major features. First of all, the magnitude of the velocity defect in the leftmost profile is of the order of one-third of the maximum velocity away from the defect. In other words, this defect magnitude is apparently adequate to induce sufficient spanwise dephasing of the oscillation, which yields attenuation. The second point is that the magnitude of this defect decays with streamwise distance along the plate, which is evident from inspection of the patterns corresponding to both configurations *C* and *E*. This decay is most likely the origin of the less effective attenuation at the largest values of L/θ for each of the three-dimensional elements investigated herein. That is, when L/θ is sufficiently large, the magnitude of the defect has decayed sufficiently at larger streamwise distances, such that effective attenuation may not be possible.

Corresponding patterns of time-averaged vorticity $<\omega>$ are given in Figure 4.3.12 for elements *C* and *E*. The peak values of vorticity in images *C* and *E* are respectively $\omega\theta/U$ 0.31 and 0.22. In other words, generation of this magnitude of dimensionless surface-normal vorticity appears to be adequate to effectively attenuate the coherent oscillation.

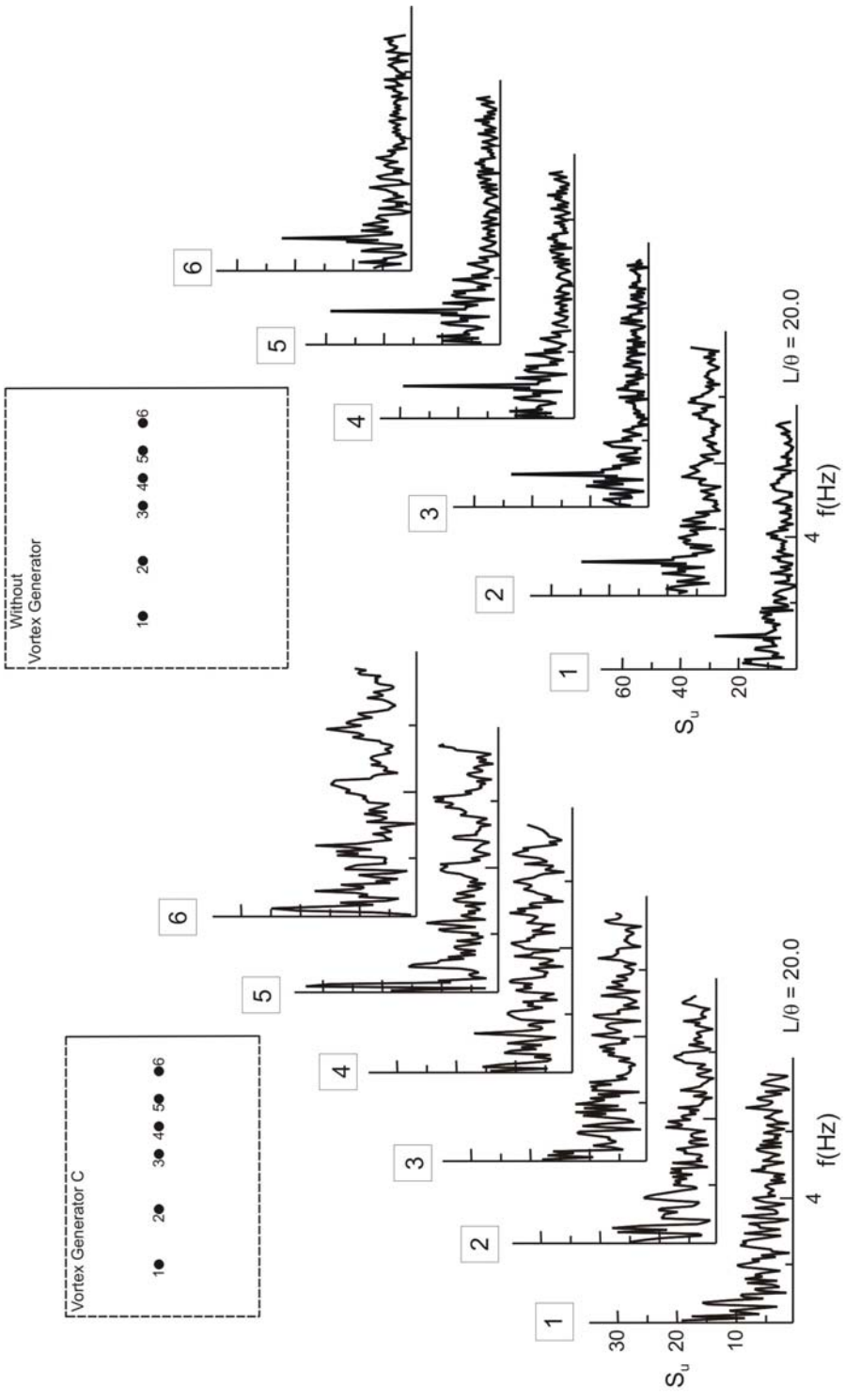

Figure 4.3.8. Spectra of velocity fluctuation S_u for various longitudinal (streamwise) locations for type C vortex generator and without vortex generator. The field of view indicated by the rectangular region at the top of each spectra has dimensions of 138 mm length and 86 mm width and 138 mm length and 142 mm width respectively. Impingement length corresponds to L/θ=20.

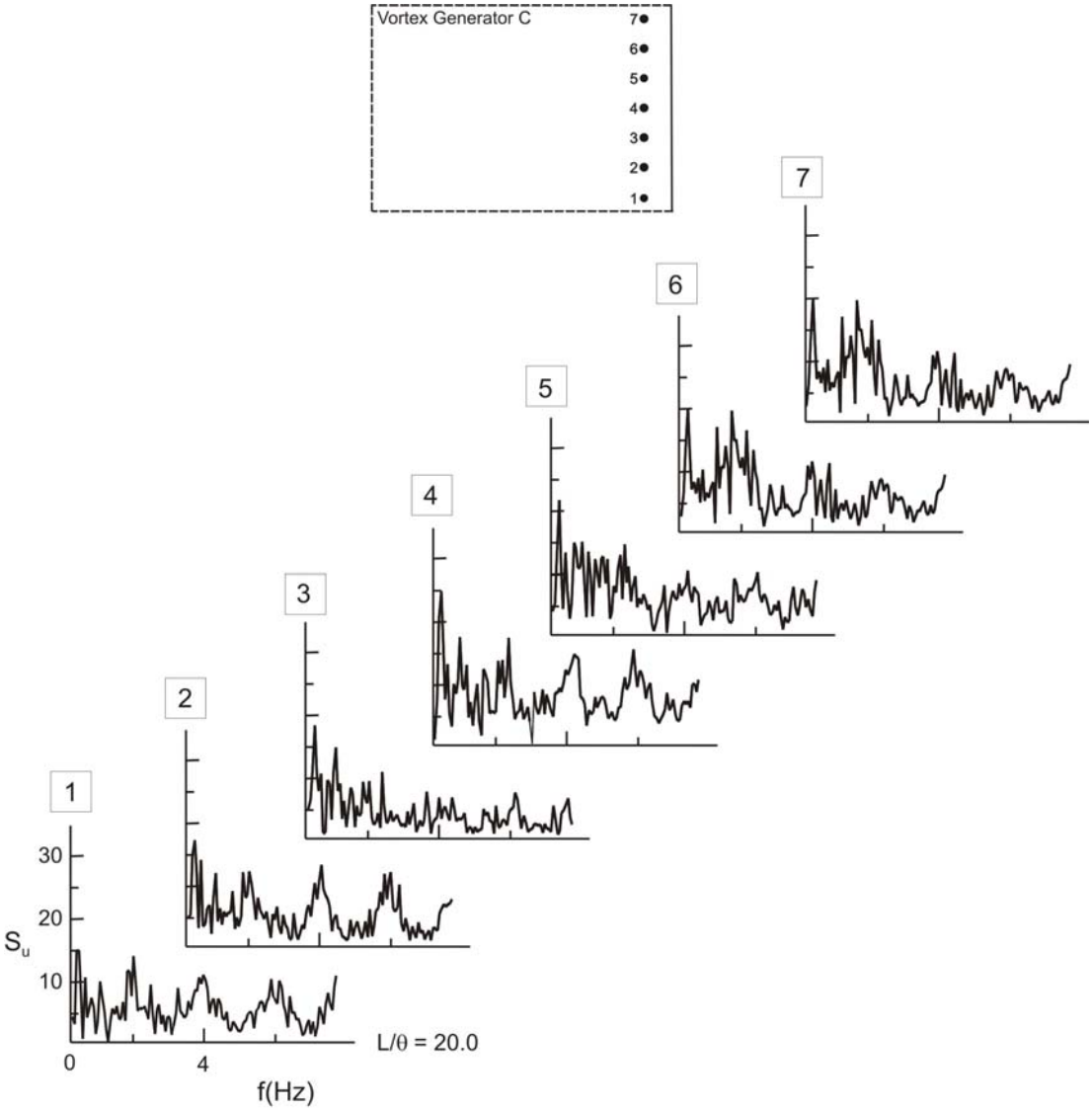

Figure 4.3.9. Spectra of velocity fluctuation S_u for various spanwise positions across the impingement plate for type *C* vortex generator and without vortex generator. Impingement length corresponds to $L/\theta = 20$.

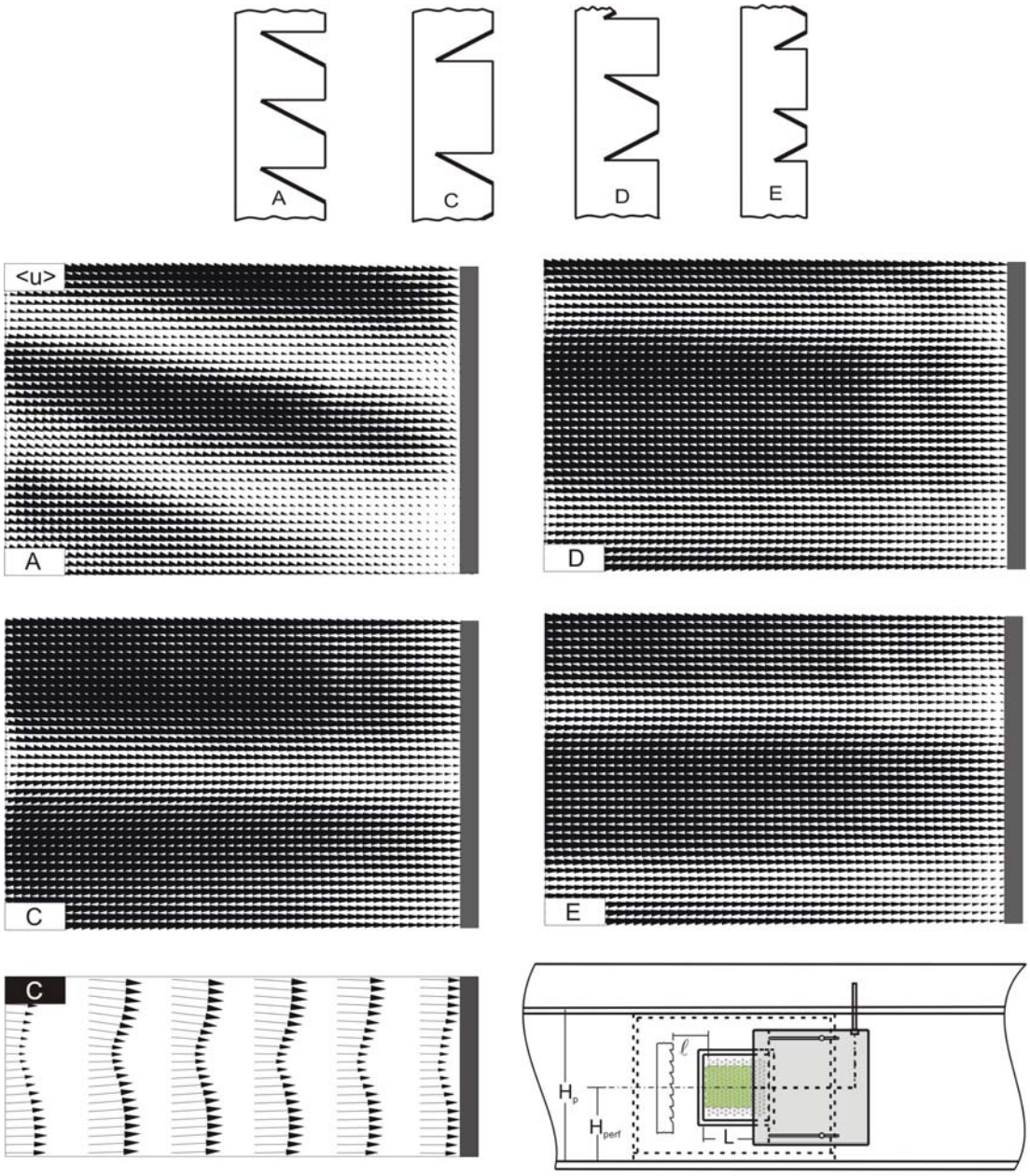

Figure 4.3.10. Patterns of average vectors of the longitudinal (streamwise) component of velocity u for various vortex generators for L/θ = 20 and L = 152.4 mm.

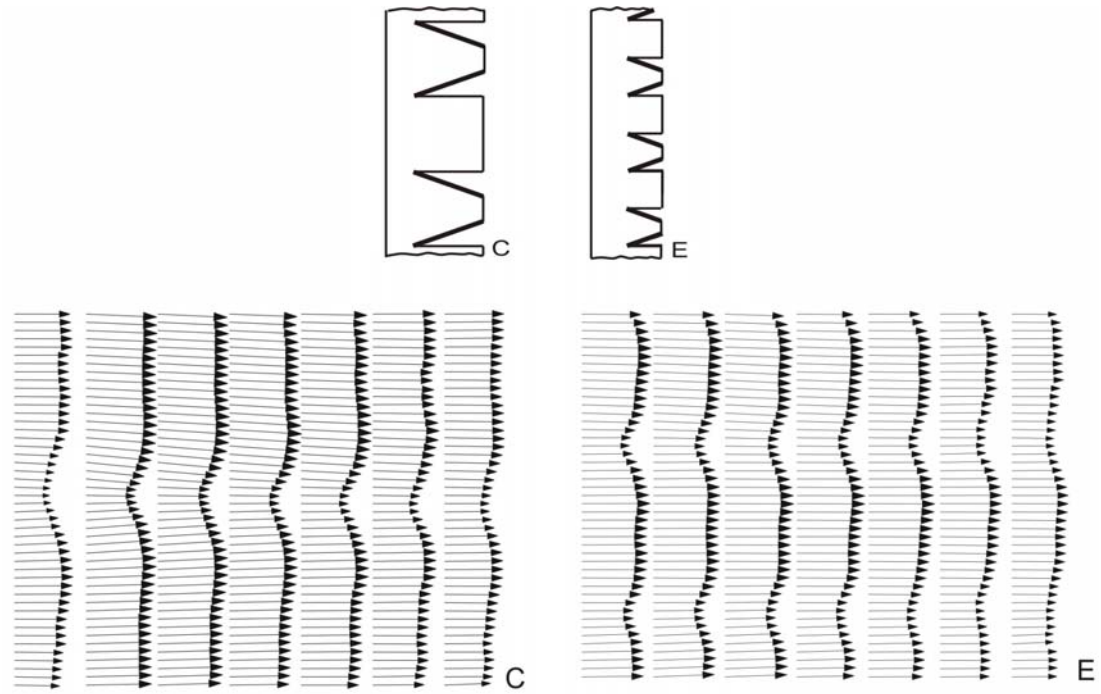

Figure 4.3.11. Patterns of the averaged velocity vectors at various streamwise locations for different vortex generators. L/θ = 20, L = 152.4 mm and width w of field of view is w/θ = 19.

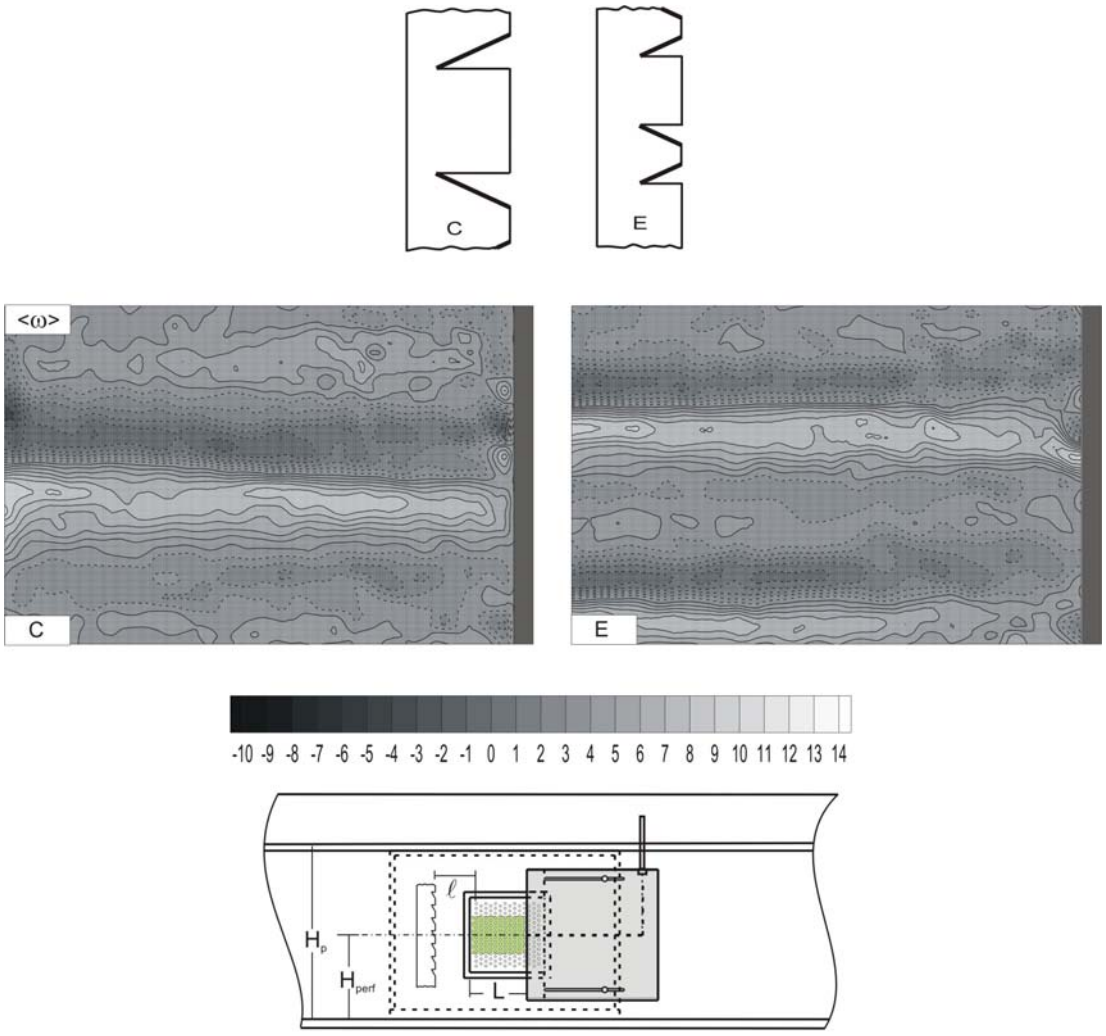

Figure 4.3.12. Contours of averaged vorticity for two representative vortex generators for L/θ = 20. Units of vorticity contours are 1/sec.

5. CONCLUSIONS AND RECOMMENDATIONS

5.1. Summary of Primary Findings

5.1.1. Self-Sustained Oscillations Past a Perforated Surface

Fully turbulent inflow past a perforated plate can give rise to highly coherent, self-sustained oscillations. This type of long wavelength instability is fundamentally different from the instability typically associated with local instabilities past the individual holes or orifices in a perforated plate. It is robust and rapidly emerges above the background level of the flow, even in the absence of acoustic-resonant coupling.

In essence, the primary findings of first part of present study are as follows:

Well-defined spectral peaks of both the pressure fluctuation at the effective trailing-end of the perforated plate, as well as in the unsteady shear layer along the plate, extend well above the background turbulence level.

For an effective hole diameter D normalized by the momentum thickness y of the turbulent boundary layer, D/θ, of the order of unity, relatively large amplitude oscillations occur, and the amplitude of the corresponding spectral peak is sharp. As the hole diameter is increased above this value, the amplitude of the oscillation decreases and the spectral peak becomes ill-defined until, at a value of $D/\theta \sim 4$, detectable oscillations are no longer evident. Further investigations should address the effect of the thickness t of the perforated plate, and its effectiveness as a normalizing parameter, i.e., normalization of the hole diameter D by t; D/t. The relative sensitivity of the oscillation to variations in inflow momentum thickness θ and t could thereby be directly assessed. Such additional studies could also provide clues to the effect of very small values of D, while open area ratio is maintained constant, on the coherence of the self-sustained oscillation.

Even when the amplitude of oscillation is significantly attenuated, but still detectable, it is demonstrated that as the effective length L of the perforated plate is varied, the dimensionless frequency fL/U remains essentially constant, for all values of hole diameter D: This observation reaffirms the view that the oscillation is indeed a long wavelength phenomenon that is not directly influenced by the scale of the individual holes of diameter D of the plate.

Patterns of time-averaged Reynolds stress show that two distinct regions occur. One region is relatively close to the perforated plate and is associated with the interaction between the shear flow and the perforations, and the other region, which is located well above the first, is associated with a classical turbulent boundary layer. For the perforated plate having holes of diameter $D/\theta \sim 1$ which give rise to the most organized and largest amplitude oscillations, the peak amplitude of Reynolds stress occurs very close to the surface of the perforated plate. Furthermore, this pattern of Reynolds stress shows an organized cell-like structure with a characteristic wavelength of the order of the hole diameter. In contrast, for the largest hole diameter $D/\theta \sim 4$, for which the organized component has an undetectable amplitude, the pattern of Reynolds stress takes on a less ordered form and its peak value is substantially smaller than for the case for which organized oscillations occur.

Distributions of amplitudes of the spectral peaks of the longitudinal and transverse (organized) velocity fluctuations in the vicinity of the trailing-end of the plate show a highly organized form, with relatively large amplitudes at the effective trailing-end of the plate. These localized regions of high amplitude are associated with a source-like region, which involves an upstream influence that sustains the long wavelength oscillation.

The spanwise structure of the flow pattern close to the surface of the perforated plate shows a well organized, yet irregular, advancing front along the surface of the plate for the case where highly coherent, self-sustained oscillations occur. This observation indicates that even though the oscillations are highly coherent, the spanwise structure of the shear layer in the immediate vicinity of the plate is not highly correlated along the span, in contrast to what one typically

observes for a free shear flow. On the other hand, for the case where self-sustained oscillations do not occur, no such advancing front is evident.

5.2. Attenuation of Self-Sustained Oscillations via Three-Dimensional Surface Elements

Robust, self-sustained, purely hydrodynamic oscillations of shear flow past a perforated plate have recently been observed. These oscillations, which occur in presence of a cavity on one side of the plate, do not involve any acoustic resonance or elastic effects. Such oscillations involve a well-defined front, which propagates along the high speed surface of the plate. The aim of the part of investigation has been to induce localized velocity and vorticity effects along the span of the propagating front, such that the oscillation is attenuated.

The results of second part of present study are as follows:

The time records and spectra of the fluctuating pressure at the effective trailing-edge of the plate provide global indicators of the strength of the shear layer oscillation. In presence of a three-dimensional surface element, it is possible to attain a substantial reduction in the degree of organization of the pressure fluctuation and the amplitude of its spectral peak. This indicator of attenuation is reinforced by spectra of the fluctuating velocity in regions upstream of the effective trailing-edge of the plate. The attenuation can involve either a reduction in amplitude of a sharply-defined spectral peak, or transformation of the sharp spectral peak to a relatively broadband, low level peak.

The most effective mitigation of the oscillation, i.e., reduction in amplitude of the spectral peak, is achieved with dimensional heights h of the three-dimensional surface elements, i.e., vortex generators, of h/θ = 1 to 2, in which θ is the momentum thickness of the inflow boundary layer. Furthermore, the most effective spanwise wavelength Λ of the generators is in the range Λ/θ = 4 to 12.

The mechanism of attenuation of the self-excited oscillation involves, first of all, streamwise striations of instantaneous velocity u and time-averaged velocity $\langle u \rangle$ at spanwise locations corresponding to the deployment of the vortex generators. The maximum value of the local defect of the time-averaged velocity $\langle u \rangle$ is of the order of one-third the undisturbed region of velocity away from the defect. These defects of $\langle u \rangle$ are associated with corresponding peaks of vorticity ω normal to the surface of the plate. These peaks are in the range $\omega\theta/U = 0.22$ to 0.43; they can have either a positive or negative sign. Furthermore, it is shown that when the striations of $\langle u \rangle$ or $\langle \omega \rangle$ are angled substantially with respect to the free-stream, the attenuation is less effective compared to cases where the induced striations are parallel to the free-stream.

A critical length L of the perforated plate exists, beyond which effective attenuation is not possible; it has a value of approximately $L/\theta = 20$. This critical length is due to the decay of the defect of $\langle u \rangle$ with streamwise distance along the perforated plate, such that, at sufficiently large value of L/θ, the defect becomes small. For the analogous case of self-sustained oscillations of shear flow along a cavity in absence of a perforated plate, it is well known that the region of upstream influence that sustains highly coherent oscillations occurs at the trailing (impingement-edge) of the cavity. If this concept is extended to the present case, then spanwise defects of $\langle u \rangle$ (and u) would correspond to decreased spanwise correlation of the shear flow-trailing-edge interaction, thereby resulting in a less effective upstream influence and amplitude of oscillation; conversely, this defect becomes small at the trailing-edge when L/θ is adjusted to larger values; the spanwise variations of $\langle u \rangle$ (and u) are not as large, and attenuation is no longer possible.

When the length of the perforated plate downstream of the vortex generators exceeds a certain value, two-dimensional oscillations reappear in the flow over the perforated plate. These observations suggest that the height h of vortex generators should be more than 5% of the length of the perforated plate, i.e., $h/L > 0.05$, in order to disrupt the two-dimensional character of the flow over the entire length of the

perforated plate. This criterion, however, must be further considered before it is taken as a design guideline.

LIST OF REFERENCES

ADAMS, W. J., 1974. The design of reactive silencers for internal combustion engines. Institute of Sound and Vibration Research, Interim Report, University of Southampton.

ADRIAN, R. J., 1986b. Image Shifting Technique to resolve directional Ambiguity in Double-Pulsed Velocimetry, Appl. Opt., 25(21), 3855-58.

ADRIAN, R. J., 1991. Particle imaging techniques for experimental fluid mechanics. Annu. Rev. Fluid Mech., 23, 261-304.

AHUJA, KK., MENDOZA, J., 1995. Effects of cavity dimensions, boundary layer, and temperature on cavity noise with emphasis on bench-mark data to validate computational aero acoustic codes. NASA contractor report: final report contract NAS1-19061, task 13.

BAUER, A. B., CHAPKIS, R. L., 1977. Noise Generated by Boundary Layer Interaction with Perforated Acoustic Liners. Journal of Aircraft, 14, 157-160.

BETTS, P.L., BINNIE, A. M., 1966. Some experiments on ship models held in a small open water channel with slotted walls. Trans. Roy. Inst. Nav. Archit. 108, 421.

BETTS, P.L., 1972. Self-induced oscillations in an open water-channel with slotted walls. J. Fluid Mech. Vol 55, Part 3, pp. 401-417.

BINNIE, A.M. AND CLOUGHLEY, T. M., 1970 “A comparison of ship model test in a slotted-wall channel and in a towing tank”, Trans. Roy. Inst. Nav. Archit. 102,102.

BRUGGEMAN, J. C., VELEKOOP, J. C., VAN DER KNAPP, F. G. P., and KEUNING, P. J., 1991. Flow-excited resonance in a cavity covered by a grid: theory and experiments. NCA-Vol.11/FED-Vol.130, Flow Modeling, Measurement and Control ASME, 135-144.

BRUGGEMAN, J.C., HIRSCHBERG, A., VAN DONGEN, M.E.H., WIJNANDS, A. P. J., AND GORTER, J., 1991. Self-sustained aero-acoustic pulsations in gas transport systems: Experimental study of the influence of closed side branches. Journal of Sound and Vibration **,**150**,** 3, 371-393.

CRIGHTON, D. G., 1975. Basic principles of aerodynamics noise generation. Progress in Aerospace Sciences, 16 ,1, 31-96.

CELIK, E, and ROCKWELL, D., 2002. Shear layer oscillation along a perforated surface: A self-excited large-scale instability. Physics of Fluids, 14,12, 4444-4448.

CELIK, E. and ROCKWELL, D., 2004. Coupled oscillations of flow along a perforated plate. Physics of Fluids, 16, 5.

DEAN, P., 1972. On the measurement of the local acoustic impedance of the walls of flow ducts and its use in predicting sound attenuation. Ph.D. Thesis, University of Southampton.

DICKEY, N. S., SELAMET, A., and CIRAY, M. S., 2001. An experimental study of the impedance of perforated plates with grazing flow. J. Acous. Soc. Am., 110, 2360-2370.

DUNHAM, W. H. 1962. Flow-induced cavity resonance in viscous compressible and incompressible fluids. Report ARC-73, Fourth Symposium on Naval Hydrodynamics, 3, ONR, 1057-1081.

EKMEKCI, A., and ROCKWELL, D., 2003. Self-sustained oscillations of the shear flow past a slotted plate coupled with cavity resonance. Journal of Fluids and Structure. 17, 8, 1237-1245.

ETHEMBABAOGLU, S., 1973. On the fluctuating characteristics in the vicinity of gate slots. Division of Hydraulic Engineering, University of Trondheim, Norwegian Institute of Technology.

GHARIB, M., ROSHKO, A., 1987. The effect of flow oscillations and cavity drag. J. Fluid Mechanics 177, 501-530.

GOLDSTEIN, M. E., 1976. Aeroacoustics, McGraw-Hill, New York.

GRACE, M. S., DEWAR, G. W., WROBLEWSKI, D. E., 2004. Experimental investigation of the flow characteristic within a shallow wall cavity for both laminar and turbulent upstream layers. Experiment in Fluids, 36, 791-804.

HARRINGTON, M. C., DUNHAM, W. H., 1960. Studies of the mechanisms for flow-induced cavity resonance. Journal of the Acoustical Society of America, 32, 921.

HOWE, M. S., 1996. Energy conservation and the damping of flexural waves by vorticity production. Journal of Sound and Vibration, 190, 1-19.

HOWE, M. S., 1997. Sound generated by turbulence and discrete vortices interacting with a perforated elastic plate in low-mach-number flow. Quarterly Journal of Mechanics & Applied Mathematics 50, 279-301.

HOWE, M. S., 1998. Acoustics of Fluid-Structure Interactions, Cambridge University Press, New York.

HU, H., SAGA, T., KOBAYASHI, T., TANIGUCHI, N., 2000. Passive control on jet mixing flows by using vortex generators. Proceed of the Sixth Triennial International Symposium on Fluid Control, Measurement and Visualization, Sherbrooke, Canada, 13-127.

JOHANSEN, J. B., and SMITH, C. R., 1983. The effect of cylindrical surface modifications on turbulent boundary layers. Report FM-3, Department of Mechanical Engineering and Mechanics, Lehigh University, Bethlehem, PA, April.

KARADOGAN, H., and ROCKWELL, D., 1983. Toward attenuation of self-sustained oscillations of a turbulent jet through a cavity. ASME J. Fluids Eng., 105**,** 3, 335-340.

KEANE, R. D., and ADRIAN, R. J., Theory of Cross-Correlation Analysis of PIV Images, Department of Theoretical and Applied Mechanics University of Illinois at Urbana- Champaign.

KELLER, J. J., AND ESCUDIER, M. P., 1979. Periodic-flow aspects of throttles, cavities, and diffusers. Brown-Boveri Research Center Report RLR-79-144 S, November.

KING, J.L., BOYLE, P., Ogle J. B., 1958. Instability in slotted wall tunnels. , Journal of Fluid Mechanics, 4, 283.

KNISELY, C., ROCKWELL, D., 1982. Self-sustained low frequency components in an impingement shear layer. Journal of Fluid Mechanics 116, 157-186.

KUETHE, A.M., 1972. Effect of stream-wise vortices on wake properties associated with sound generation. Journal of Aircraft 9, 10, 715-719.

KUO, C. H., HUANG, S. H., 2001. Influence of flow path modification on oscillation of cavity shear layer. Experiment in Fluids, 31 162-178.

KUO, C. H., HUANG, S. H., 2003. Effect of surface mounting of upper plate on oscillating flow structure within cavity. Experimental Thermal and Fluid Sciences, 27, 755-768.

KUO, C. H., JENG W. I., 2003. Lock-on characteristic of a cavity shear layer, Journal of Fluid and Structures, 18, 715-728.

KUO, C. H., CHANG, C. W, 1998. Shear-layer characteristic across a cavity with horizontal top plate. Fluid Dynamic Research, 22, 89-104.

KUO, C. H., HUANG, S. H., CHANG, C. W., 2000. Self-sustained oscillation induced by horizontal cover plate above a cavity, Journal of Fluids and Structures, 14, 25-48.

LANDRETH, C. C and ADRIAN, R.J., 1989. Measurement and refinement of velocity data using high image density in particle image velocimetry, Application of Laser Anemometry: Proceedings of the 4th International Symposium, edited by R.J. Adrian, T. Asunuma, D. Durao, F. Durst abd J. Whitlaw, Springer Verlag, Berlin, 484-499

LIN, J. C., 2002. Review of research on low-profile vortex generators to control boundary layer separation, Progress in Aerospace Sciences, 38, 389-420.

LIN, J. –C. AND ROCKWELL, D. 1999. Cinema PIV and its application to impinging vortex systems. Journal of Fluids Engineering, 121, 4, 720-724.

LIN, J.C. and ROCKWELL D., 2001. Organized oscillations of initially turbulent flow past a cavity. AIAA Journal, 39, 6, 1139-1150.

LIN, J.C.,1994. NFILVB Software, Fluid Mechanics Lab, Lehigh University.

LIN, J.C.,1996. NWENSAV2 software, Fluid Mechanics Lab, Lehigh University.

LOOIJMANS, K. N. H., AND BRUGGEMAN, J. C., 1997. Simple vortex models for vibration and noise caused by a flow over louvers in a cavity opening. Proceedings Fluid-Structure Interactions, Aeroelasticity, Flow-Induced Vibration and Noise Symposium, 1 ASME AD-Vol.53-1, 351-359.

LYER, C. O., CECCIO, S. L., LABERTEAUX, K. R., 1998. An experimental study of cavitating and non-cavitating shear flows, Proceedings of FEDSM'98, 1998

ASME Fluids Engineering Divisions Summer Meeting June 21-25, 1998, Washington, DC.

MAUNG, P.M., HOWE, M.S., MICKINLEY, G.H., 1999. Experimental investigation of the damping of structural vibrations by vorticity production. Journal of Sound and Vibration, 220, 297-312.

MCCORMICK, D. C., 1992. Shock-boundary layer interaction control with low-profile vortex generators and passive cavity. AIAA Paper 92-0064, 30th AIAA Aerospace Sciences Meeting and Exhibit, Reno, NV, January 6-9.

MEDVED, B.L., 1993. Some acoustic features of perforated test section walls with splitter plates. AIAA Journal 31, 1885–1890.

MEYER, E., MECHEL, F., AND KURTZE, G., 1958. Experiments on the influence of flow on sound attenuation in absorbing ducts. J. Acoust. Soc. Am., 30, 165-174.

NELSON, P. A., 1982. Noise generated by flow over perforated surfaces. Journal of Sound and Vibration, 83, 11-26.

NEWLAND, D. E., 1993. An introduction to random vibrations, Spectral and Wavelet Analysis. 3rd Edition, Longman Singapore Publishers, Singapore, ISBN 0582 215 846.

ÖZGÖREN, M., 2000. Impingement of vortex breakdown upon an edge: Flow structure and origin of loading Ph.D. Thesis, Cukurova University Institute of Natural and Applied Sciences, ADANA .

PEREIRA, J. C. F. AND SOUSA, J. M.M., 1993. Finite Volume Calculations of Self-Sustained Oscillations in a Grooved Channel. Journal of Computational Physics, 106, 19-29.

PEREIRA, J. C. F. AND SOUSA, J. M.M., 1995. Experimental and numerical investigation of flow oscillations in a rectangular cavity. Transactions of the ASME, Journal of Fluids Engineering, 117, 68-74.

ROCKWELL, D., KNISELY, C., 1979. The organized nature of floe impingement upon a corner. Journal of Fluid Mechanics, 93, 3, 413-432.

ROCKWELL, D., AND NAUDASCHER, E., 1978. Review–self-sustaining oscillations of flow past cavities. ASME J. Basic Eng., 100, 152-165.

ROCKWELL, D. 1983. Invited lecture: oscillations of impinging shear layers. AIAA Journal, 21, 5, 645-664.

ROCKWELL, D. AND NAUDASCHER, E. 1979. Self-sustained oscillations of impinging free shear layers. Annual Review of Fluid Mechanics, 11, 67-94.

ROCKWELL, D. AND NAUDASCHER, E. 1980. Practical experiences with flow-induced vibrations. Proceedings of the 1979 IAHR/IUTAM Symposium, Springer-Verlag, Berlin.

RONNEBERGER, D., 1980. The dynamics of shearing flow over a cavity a visual study related to the acoustic impedance of small orifices. Journal of Sound and Vibration, 71**,** 565-581.

ROWLEY, C. W., COLONIUS, T., BASU, A.J., 2002, On self-sustained oscillations in two-dimensional compressible flow over rectangular cavities. J. Fluid Mechanic, 455, 315-346.

SAROHIA, V., 1977. Experimental investigation of oscillations in flows over shallow cavities. AIAA Journal, 15, 7, 984 991.

TAYLOR, H.D., 1947. The elimination of diffuser separation by vortex generators United Aircraft Corporation Report No R-4012-3.

TSUI, C. Y., AND FLANDRO, G. A., 1977. Self-induced sound generation by flow over perforated duct liners. Journal of Sound and Vibration, 50, 315-331.

YARAGAL, S. C., RAM, H. S.G., MURTHY, K. K., 2002. Two dimensional flow field behind perforated plates on a flat surface. Journal of Wind Engineering and Industrial Aerodynamics, 90, 75-90

ZHANG, X., CHEN, X. X., RONA, A., 1999. Attenuation of cavity flow oscillation through leading edge corner, Journal of Sound and Vibration, 221,1, 23-47.

ZOCCOLA, P. J., 2002. Excitation by flow over an obstructed opening. ASME IMECE2002/NCA-33374.

CIRRICULUM VITAE

Coşkun Özalp was born on November 1, 1973 in Doğanşehir-Malatya, Turkey. In 1990, he graduated from High School. He graduated with Bachelor of Science degree in mechanical engineering from the Department of Mechanical Engineering in 1997. He began to work as a Research Assistant in 1998 and he received his M. Sc. Degree in February 2000 at the Department of Mechanical Engineering of Çukurova University. In February 2000 he began his Ph. D. program at the same department. In 2001 he went to Department of Mechanical enginnering and Mechanics, Lehigh University, Bethlehem, PA, USA to carry out his Ph. D thesis. While at Lehigh he worked as a visitor researcher in the Fluid Mechanics Laboratories for 15 months.

APPENDIX A

Vorticity Evaluation

For 2-D flows, the out-of-plane component of vorticity is given by:

$$\Omega = \frac{1}{2}\left(\frac{\partial v}{\partial x} - \frac{\partial u}{\partial y}\right)$$

The most common way to compute this expression numerically is to approximate the partial derivatives with finite difference. Using central differences at an interior point to leads to:

$$\Omega_{ij} = \frac{1}{2}\left(\frac{v(i+1,j) - v(i-1,j)}{2\delta_x} - \frac{u(i,j+1) - u(i,j-1)}{2\delta_y}\right)$$

Any computation involving derivatives is very sensitive to noises that are the primary reason to try to smooth out the velocity field before computation of the vorticity, strain rate or similar gradient quantities.

Another way around the noise problem for the particular case of the computation of vorticity is to use a self-smoothing method derived from the Stokes theorem. This the so-called circulation method that the user can choose to compute the vorticity in NFILVB.

The stokes theorem can be formulated as:

$$\iint \left(\vec{\nabla} \times \vec{u}\right) d\vec{s} = \oint \vec{u} d\vec{l}$$

Assuming that the vorticity is constant all over the unit surface formed by the four grid cells surrounding a given point, the vorticity a that point is given by:

$$\Omega = \frac{1}{4\delta_x \delta_y} \oint \vec{u} d\vec{l}$$

where the integral is the circulation of the velocity around the path formed by the sides of the unit surface.

APPENDIX B

Bilinear Interpolation

To fill the gaps left in the data grid by the interrogation system NFILVB is using a bilinear least square fit technique.

Knowing the data values u_1,….., u_n at the N nearest neighbor location of a point where the data u is missing, the idea is to find a value for u that does not deviate too much from these values. To realize this goal, in a least square technique, one has to minimize the merit function:

$$\chi^2 = \sum_{k=1}^{N} \frac{|u_k - u|^2}{\sigma_k}$$

As suggested by Adrian et al., NFILVB is applying this method to a linear model of the 2 components of velocity:

$u=a_0+a_1x+a_2y$

$v=b_0+b_1x+b_2y$

using the 5 nearest neighbors of a missing data. The standard way to deal with the measurement errors σ_k, on each data u_k, when they are not known, is to set them to 1. The minimum of the merit function:

$$\chi^2 = \sum_{k=1}^{5} \left| u_k - (a_0 + a_1 x + a_2 y) \right|^2$$

occurs when:

$$\frac{\partial \chi^2}{\partial a_0}(x_k, y_k) = \frac{\partial \chi^2}{\partial a_1}(x_k, y_k) = \frac{\partial \chi^2}{\partial a_2}(x_k, y_k) = 0 \quad \text{for k=1,……..,5}$$

This is a linear system of 15 equations and 3 unknowns that is solved using the Singular Value Decomposition (SVD) technique described in the Numerical Recipes books.

Gaussian Smoothing

To reduce the measurement noises in the velocity data from PIV, a local weighted averaging technique is used in NFILVB. The weights used are Gaussian:

$$u(x_i, y_j) = \sum_{m=-4}^{4} \sum_{k=-4}^{4} w_{km} u(x_{i-k}, y_{j-m})$$

where:

$$w_{km} = \frac{\omega_{km}}{\sum_{k=-4}^{4} \sum_{m=-4}^{4} \omega_{km}}$$

and $\omega_{km} = e^{\frac{2(k^2+m^2)}{\sigma^2}}$

The parameter σ is the smoothing parameter that the user is asked for when running NFILVB. It controls how fast the Gaussian ω is decaying and therefore, determines the contributions of the surrounding points to the average value.

APPENDIX C

Averaged Flow Structure

Calculation of the averaged quantities was performed according to the equations listed in the flowing table. Each averaged parameter was calculated at each spatial coordinate (x,y) by considering the average of all instantaneous values (x,y). The terminology for each of the averaged parameters and the dimensionless equation employed to determine the averaged parameter as follows:

<V> ≡ averaged (or mean) total velocity

$$< V > \equiv \frac{1}{N}\sum_{n=1}^{N} V_n(x,y)$$

<u> = averaged value of streamwise component of velocity

$$< u > \equiv \frac{1}{N}\sum_{n=1}^{N} u_n(x,y)$$

<v> = averaged value of transverse component of velocity

$$< v > \equiv \frac{1}{N}\sum_{n=1}^{N} v_n(x,y)$$

<ω> = mean value of vorticity

$$< \omega > \equiv \frac{1}{N}\sum_{n=1}^{N} \omega_n(x,y)$$

u_{rms} = root-mean-square of u component fluctuation

$$u_{rms} \equiv < u >_{rms} \equiv \left[\frac{1}{N}\sum_{n=1}^{N} \left[u_n(x,y) - < u(x,y) > \right]^2 \right]^{1/2}$$

v_{rms} = root-mean-square of v component fluctuation

$$v_{rms} \equiv < v >_{rms} \equiv \left[\frac{1}{N} \sum_{n=1}^{N} \left[v_n(x,y) - < v(x,y) > \right]^2 \right]^{1/2}$$

$< u'v' >$ = averaged value of Reynolds stress correlation

$$< u'v' > = \frac{1}{N} \sum_{n=1}^{N} \left[u_n(x,y) - < u(x,y) > \right] \left[v_n(x,y) - < v(x,y) > \right]$$

APPENDIX D

Spectral Analysis

In order to estimate spectra from measured data, the obvious method is to estimate the appropriate correlation function first and than Fourier transform this function to obtain the required spectrum. Until the late 1960s, this approach was the basis of practical calculation procedures which followed the formal mathematical route by which spectra are defined as Fourier transform of correlation functions. Newland (1993)

From the book of Newland (1993), spectral density functions of random process can be defined as the fourier transforms of corresponding auto- and cross-corrleation fuctions. Therefore if $R_{xx}(\tau)$ and $R_{xy}(\tau)$ are auto and cross-corrlation functions, the auto-and cross-spectral density can be defined as

$$S_{xy}(\bar{\omega}) = \frac{1}{2\pi}\int_{-\infty}^{\infty} R_{xy}(\tau) e^{-i\bar{\omega}\tau} d\tau \qquad 1$$

$$S_{yx}(\bar{\omega}) = \frac{1}{2\pi}\int_{-\infty}^{\infty} R_{xy}(\tau) e^{-i\bar{\omega}\tau} d\tau \qquad 2$$

and their accompanying transform relations which are

$$R_{xx}(\tau) = \frac{1}{2\pi}\int_{-\infty}^{\infty} S_{xy}(\omega) e^{i\omega\tau} d\omega \qquad 3$$

$$R_{yx}(\tau) = \frac{1}{2\pi}\int_{-\infty}^{\infty} S_{yx}(\omega) e^{i\omega\tau} d\omega$$

Due to cross-corrlelation functions are related by $R_{xy}(\tau) = R_{yx}(-\tau)$, equ. 1 becomes in the form of

$$S_{xy}(\omega) = \frac{1}{2\pi}\int_{-\infty}^{\infty} R_{yx}(-\tau) e^{-i\omega\tau} d\tau \text{ and substituting } \tau' = -\tau$$

$$S_{xy}(\omega) = \frac{1}{2\pi}\int_{-\infty}^{\infty} R_{yx}(\tau') e^{-i\omega\tau'} d\tau' \qquad 4$$

is obtained.

Since FFT originally works with complex data to write equ. 4 in the complex form, let x(t) is a fuction of time, with period T,

$$x(t) = a_o + \sum_{k=1}^{\infty}\left(a_k \cos\frac{2\pi kt}{T} + b_k \sin\frac{2\pi kt}{T} \right) \qquad 5$$

where a_0 and a_k and b_k are constont Fourier coefficients given by

$$a_0 = \frac{1}{T}\int_{-T/2}^{T/2} x(t)dt$$

$$a_{\substack{k \\ k\geq 1}} = \frac{2}{T}\int_{-T/2}^{T/2} x(t)\cos\frac{2\pi kt}{T}dt \qquad 6$$

$$b_{\substack{k \\ k\geq 1}} = \frac{2}{T}\int_{-T/2}^{T/2} x(t)\sin\frac{2\pi kt}{T}dt$$

Substituting 6 into 5 for a_0=0

$$x(t) = \sum_{k=1}^{\infty}\left\{ \frac{2}{T}\int_{-T/2}^{T/2} x(t)\cos\frac{2\pi kt}{T}dt \right\}\cos\frac{2\pi kt}{T} + \sum_{k=1}^{\infty}\left\{ \frac{2}{T}\int_{-T/2}^{T/2} x(t)\sin\frac{2\pi kt}{T}dt \right\}\sin\frac{2\pi kt}{T}$$

Next substituting for $\omega_k = \frac{2\pi k}{T}$ and $\Delta\omega = \frac{2\pi}{T}$

$$x(t) = \sum_{k=1}^{\infty}\left\{ \frac{\Delta\omega}{\pi}\int_{-T/2}^{T/2} x(t)\cos\omega_k t dt \right\}\cos\omega_k t + \sum_{k=1}^{\infty}\left\{ \frac{\Delta\omega}{\pi}\int_{-T/2}^{T/2} x(t)\sin\omega_k t dt \right\}\sin\omega_k t$$

when the period $T \to \infty, \Delta\omega \to d\omega$ and the $\sum$ becomes an integral with the limits $\omega = 0$ *to* $\omega = \infty$. In this case

$$x(t) = \int_{\omega=0}^{\infty} \frac{d\omega}{\pi} \left\{ \int_{-\infty}^{\infty} x(t) \cos \omega_k t dt \right\} \cos \omega_k t + \int_{\omega=0}^{\infty} \frac{d\omega}{\pi} \left\{ \int_{-\infty}^{\infty} x(t) \sin \omega_k t dt \right\} \sin \omega_k t$$

or putting

$$A(\omega) = \frac{1}{2\pi} \int_{-\infty}^{\infty} x(t) \cos \omega t dt$$

7

$$B(\omega) = \frac{1}{2\pi} \int_{-\infty}^{\infty} x(t) \sin \omega t dt$$

gives $x(t) = 2\int_{0}^{\infty} A(\omega) \cos \omega t d\omega + 2\int_{0}^{\infty} B(\omega) \sin \omega t d\omega$ 8

The terms $A(\omega)$ and $B(\omega)$ defined by equ. 7 are the components of the Fourier transform of x(t) and equ. 8 is a representation of x(t) by a Fourier integral of inverse Fourier transform.

To write equations 7 and 8 in complex form making use of the result that

$$e^{i\theta} = \cos \theta + i \sin \theta$$ 9

Defining

$X(\omega) = A(\omega) - iB(\omega)$ equations may be combined to give

$$X(\omega) = \frac{1}{2\pi} \int_{-\infty}^{\infty} x(t) (\cos \omega t - i \sin \omega t) dt$$

$$= \frac{1}{2\pi} \int_{-\infty}^{\infty} x(t) e^{-i\omega t} dt$$ 10

from equation 9. The latter equation is the formal definition of $X(\omega)$ which is called the fourier transform of x(t).

If we return to equation 4 according to equations 9 and 10,

$$S_{xy}(\omega) = A(\omega) - iB(\omega)$$

and

$$S_{yx}(\omega) = C(\omega) - iD(\omega)$$

where $A(\omega)$, $B(\omega)$, $C(\omega)$ and $D(\omega)$ are real functions of ω.

The amplitude of the any signal is calculated

$$\text{Amplt}^2 = A^2 + B^2 \qquad 11$$

$$\text{Phase} = \arctan(B/A)$$

APPENDIX E

PERFORMANCE	**ENGLISH**	**SI**
Measurement Range (for ± 2.5V output)	5 psi	35 kPa
Useful Overrange	5 psi	35 kPa
Sensitivity (± 15 %)	500 mV/psi	72.5 mV/kPa
Maximum Pressure (step)	100 psi	690 kPa
(static)	500 psi	3448 kPa
Resolution	0.07 mpsi	0.00048 kPa
Resonant Frequency	≥ 40 kHz	≥ 40 kHz
Rise Time	≤ 12 μ sec	≤ 12 μ sec
Low Frequency Response (-5 %)	0.5 Hz	0.5 Hz
Non-Linearity	≤ 1 % FS	≤ 1 % FS
ENVIRONMENTAL		
Acceleration Sensitivity	≤ 0.002 psi/g	≤ 0.0014 kPa/(m/s^2)
Temperature Range (Operating)	-65 to +250 °F	-54 to +121 °C
Temperature Coefficient of Sensitivity	≤ 0.03 %/°F	≤ 0.054 %/°C
Maximum Flash Temperature	3000 °F	1649 °C
Maximum Vibration	500 g pk	4903 m/s^2 pk
Maximum Shock	1000 g pk	9807 m/s^2 pk
ELECTRICAL		
Output Polarity (Positive Pressure)	Positive	Positive
Discharge Time Constant (at room temp)	≥ 1 sec	≥ 1 sec
Excitation Voltage	11 to 30 VDC	11 to 30 VDC
Constant Current Excitation	2 to 20 mA	2 to 20 mA
Output Impedance	≤ 100 ohm	≤ 100 ohm
Output Bias Voltage	3 to 8 VDC	3 to 8 VDC
PHYSICAL		
Sensing Element	Quartz	Quartz
Housing Material	17-4 Stainless Steel	17-4 Stainless Steel
Diaphragm	316L Stainless Steel	316L Stainless Steel
Sealing	Welded Hermetic	Welded Hermetic
Electrical Connector	10-32 Coaxial Jack	10-32 Coaxial Jack
Weight	1.13 oz	32 gm